Interferometric Diagnosis of Warm Dense Matter

Interferometrische Untersuchungen an warmer dichter Materie
Zur Erlangung des Grades eines Doktors der Naturwissenschaften (Dr. rer. nat.)
genehmigte Dissertation von Dipl.-Ing. Bogdan-Florin Cihodariu-Ionita aus Bacau, Romania
2013 — Darmstadt — D 17

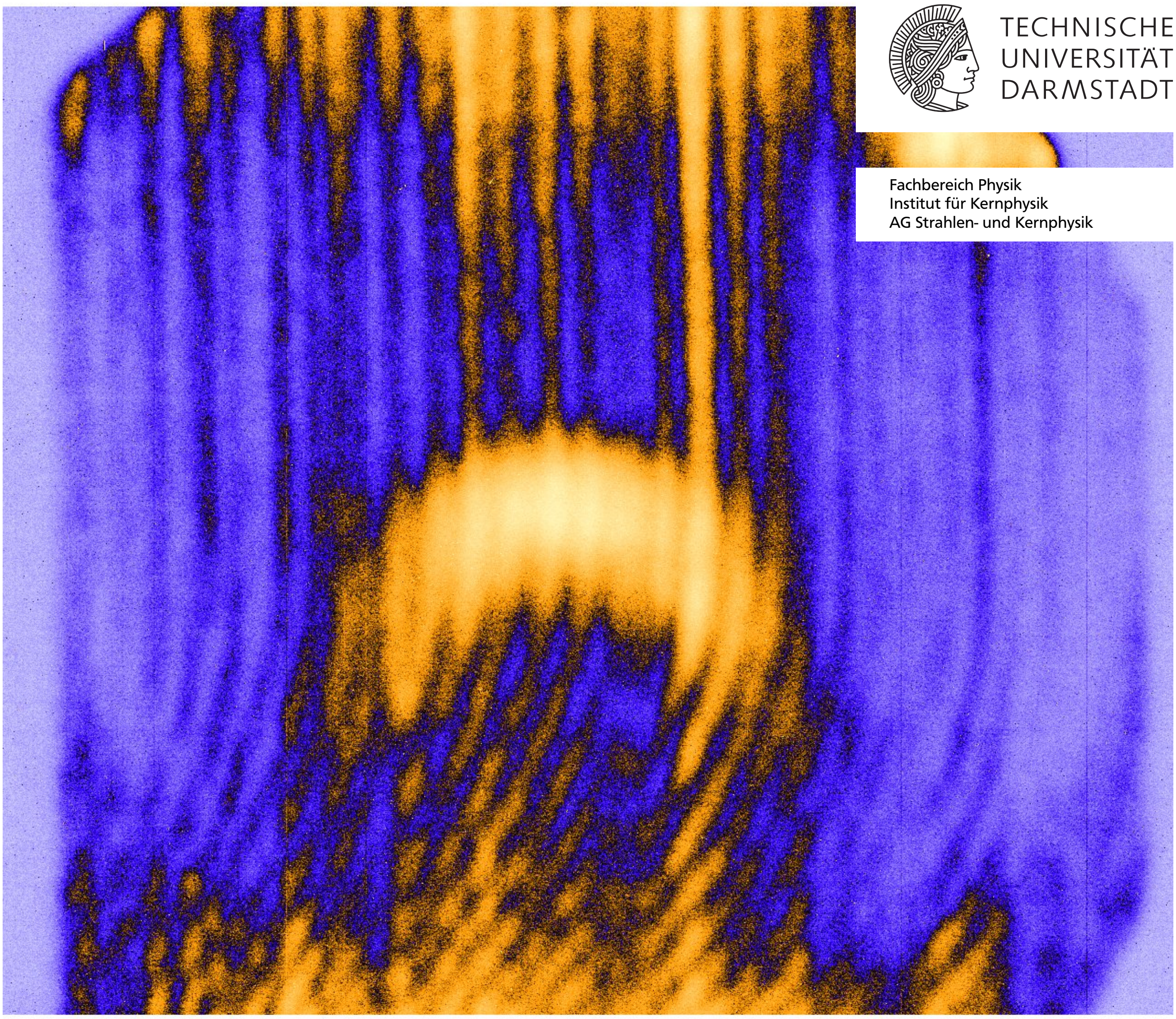

TECHNISCHE
UNIVERSITÄT
DARMSTADT

Fachbereich Physik
Institut für Kernphysik
AG Strahlen- und Kernphysik

Interferometric Diagnosis of Warm Dense Matter
Interferometrische Untersuchungen an warmer dichter Materie

Genehmigte Dissertation von Dipl.-Ing. Bogdan-Florin Cihodariu-Ionita aus Bacau, Romania

1. Gutachten: Prof. Dr. Dr. h.c./RUS D.H.H. Hoffmann
2. Gutachten: Prof. Dr. Markus Roth

Tag der Einreichung: 27.11.2012
Tag der Prüfung: 21.12.2012

Darmstadt — D 17

Dedicated to the memory of my grandmother Marieta Ionita

Zusammenfassung

Materie unter extremen Druck und Temperatur Bedingungen bietet einen aufregenden Forschungsbereich sowohl für die Grundlagen- als auch die angewandte Forschung. Die fundamentalen physikalischen Eigenschaften solcher Zustände hoher Energiedichte (High Energy Density – HED states) – wie die Zustandsgleichung (equation of state – EOS) – sind von großer Bedeutung sowohl für theoretische als auch für experimentelle Untersuchungen. Solche extreme Zustände können unter Laborbedingungen nur in dynamischen Experimenten mit besonders leistungsfähigen Treibern erreicht werden. Das GSI Helmholtzzentrum für Schwerionenforschung (GSI) mit seinem einzigartigen Schwerionensynchrotron SIS-18 and dem Hohe Energie Petawatt Laser PHELIX bietet ideale Möglichkeiten zur Erforschung dieser Materiezustände.

Das Ziel dieser Arbeit ist, die thermophysikalischen Eigenschaften von Metallen im Bereich der Warmen Dichten Materie (WDM), die sich durch Temperaturen von 1-50 eV und Dichten nahe deren der Festkörper charakterisiert, mittels interferometrischer Messungen zu untersuchen.

Am Hochtemperaturmessplatz HHT des GSI wurden Druck- und Temperaturmessungen im Bereich des kritischen Punktes von Metallen durchgeführt. Zu diesem Zweck, wurden intensive, gepulste Uranionenstrahlen mit einer Dauer von weniger als einer Mikrosekunde auf einen Submillimeter-Bereich eines festen metallischen Targets fokussiert. Dadurch wurden sowohl eine hohe Energiedichte als auch eine gleichmäßige volumetrische Heizung erzielt. Das expandierende Material traf auf ein Saphirfenster und wurde dadurch komprimiert. An der somit gebildeten Grenzfläche wurden mit einem schnellen Mehrkanalpyrometer Temperaturmessungen durchgeführt. Gleichzeitig wurde das Geschwindigkeitsprofil der freien Fensterfläche mit einem abbildenden Interferometer ermittelt wodurch der zeitliche Druckverlauf bestimmt werden konnte.

Am Experimentierplatz Z6 des GSI wurden Experimente zur isentropischen Kompression von Eisen mittels des hochintensiven Laserstrahls des PHELIX Systems durchgeführt. Geschwindigkeitsmessungen im km/s Bereich wurden an der freien Fläche des Targets mit zwei abbildenden VISAR (Velocity Interferometer System for Any Reflector) durchgeführt. Daraus wurden Druckprofile mit Werten bis zu 0,25 Mbar abgeleitet. Das Verhalten von Eisen beim $\alpha - \epsilon$ Übergang wurde bei verschiedenen Kompressionsraten untersucht.

Überdies wurde die am HHT vorhandene Software zur Datenaufnahme für Experimente mit Schwerionenstrahlen erweitert.

Abstract

Matter at extreme pressures and temperatures provides an exciting field of research in both fundamental and applied physics. The basic physical properties of these "High Energy Density" (HED) states – for instance the equation of state (EOS) – are of great importance from an experimental as well as theoretical point of view. Under laboratory conditions such extreme states can be reached only in dynamic experiments using extremely powerful drivers. The GSI Helmholtzzentrum für Schwerionenforschung (GSI), with its unique heavy ion accelerator SIS-18 and high energy petawatt laser PHELIX facilities offers ideal conditions for the investigation of these states of matter.

The aim of this work is to apply interferometric methods for studying thermophysical properties of metals within the warm dense matter (WDM) region of the phase diagram, characterized by temperatures of 1-50 eV and densities close to the solid state one.

At the "High Temperature" (HHT) experimental area of GSI, pressure and temperature measurements of metals heated by intense uranium ion beams to regions near the critical point were performed. Sub-microsecond intense uranium ion beams were focused on a sub-millimetre spot on solid metallic targets, achieving both high energy density deposition and uniform volumetric heating. The expanding material got compressed against a sapphire window and temperature measurements were taken at this interface with a fast multi-channel pyrometer, while spatial velocity profiles were recorded on the free surface by the imaging displacement interferometer allowing for the determination of temporal pressure profiles.

At the Z6 experimental area of GSI isentropic compression experiments of iron were conducted using PHELIX as driver. Free surface velocity measurements on the order of km/s were performed using two imaging VISARs (Velocity Interferometer System for Any Reflector) from which pressure profiles up to 0.25 Mbar were derived. The behaviour of iron during the $\alpha - \epsilon$ transition at different compression rates was studied.

Besides the interferometric set-ups, work was performed on the data acquisition system for the heavy–ion beam driven experiments at the HHT area.

Contents

List of Figures

Abbreviations and symbols used

AMeV MeV per nucleon
AOM Acousto-optic modulator
CCD Charge-Coupled Device
EOS Equation of State
ESR Experimentierspeicherring
FAIR Facility for Antiproton and Ion Research
FCT Fast Current Transformer
FWHM Full Width at Half Maximum
GSI GSI Helmholtzzentrum für Schwerionenforschung GmbH
GUI Graphical User Interface
HED High Energy Density
HEDgeHOB High Energy Density Matter generated by Heavy Ion Beams (Collaboration)
HEDP High Energy Density Physics
IPCP Institute for Problems of Chemical Physics, Chernogolovka, Russia
LLNL Lawrence Livermore National Laboratory (LLNL)
LULI Laboratoire pour l'Utilisation des Laser Intenses, Palaiseau Cedex, France
OPD Optical Path Difference
SIS-18 Schwerionensynchrotron 18 Tm (Heavy Ion Synchrotron)
UNILAC Universal Linear Accelerator
VISAR Velocity Interferometer System for Any Reflector
WDM Warm Dense Matter

1 Introduction

The GSI Helmholtzzentrum für Schwerionenforschung GmbH (GSI) provides accelerator facilities with which a large range of ions (from hydrogen to uranium) can be accelerated to various final energies, from a few AMeV with the UNILAC linear accelerator, to 1-2 AGeV with the SIS-18 heavy ion synchrotron. Experiments are conducted in a wide range of fields, from nuclear physics, atomic physics, material science to biophysics and cancer therapy. The institute also provides the unique possibility of conducting experiments in which powerful laser beams and ion beams can simultaneously interact with various targets. The laser beams are provided by the nhelix - "Nanosecond High Energy Laser for Ion beam eXperiments" and PHELIX - "Petawatt High Energy Laser for heavy Ion eXperiments" systems.

At the "High Temperature" (HHT) area High Energy Density Physics (HEDP) experiments are performed using heavy ion beams accelerated by the heavy ion synchrotron SIS-18. The accessible states of matter are of great interest for the research of physical properties of Warm Dense Matter (WDM), with quasi-isochoric heating of macroscopic volumes at near-solid density up to the 1 eV range. Among the results already obtained at HHT stand the hydrodynamic motion of the heavy ion beam heated target material observed using laser deflection [1] and shadowgraphy techniques with various high-speed multi-framing and streak cameras, compression caused by multiple weak shock waves in transparent targets studied using schlieren [2] and interferometric methods [3, 4]. Also, direct time-resolved pressure measurements were performed using piezo-electric pressure gauges embedded in the targets [5]. More recently, interferometric methods were deployed as plasma pressure diagnostic in [6]. The main research activities in the last few years at HHT have been the testing of target geometries for experiments performed within the HEDgeHOB (High Energy Density Matter Generated by Heavy IOn Beams) collaboration [7], as well as the investigation of properties of matter under extreme conditions and in high energy density (HED) states [8], including its equation of state and transport properties, like the electrical conductivity [9, 10, 11, 12].

The powerful laser systems available at Z6 allow for the generation of energetic plasmas, which then can be studied in their interaction with ion beams. For example the energy loss of ions going through plasma generated with nhelix was studied in [13]. Since the commissioning of PHELIX in 2008, the range of experiments at Z6 has expanded [14]. With energies of a couple hundred joule per pulse, pulse durations up to 15 ns, and pulse profiling, PHELIX also provides unique capabilities for the isentropic compression experiments described in this work.

The study of WDM states is important because, as can be seen in Figure 1.1, they lie in a region of the phase diagram which has to be crossed in order to access more energetic states. This region is poorly explored both experimentally and theoretically. In this thesis, research was focused on the development and implementation of advanced interferometric pressure diagnostic tools for matter in these states.

Part of this research represents a continuation of the work performed previously at HHT [6, 8] with point displacement interferometers, bringing imaging capabilities to the diagnostic systems, capabilities which are crucial in unequivocally determining the direction of motion of the target surface. The scope of these experiments was to study the behaviour of lead near the critical point around 5500 K and 2.3 kbar and in two-phase liquid-vapour states. By these means

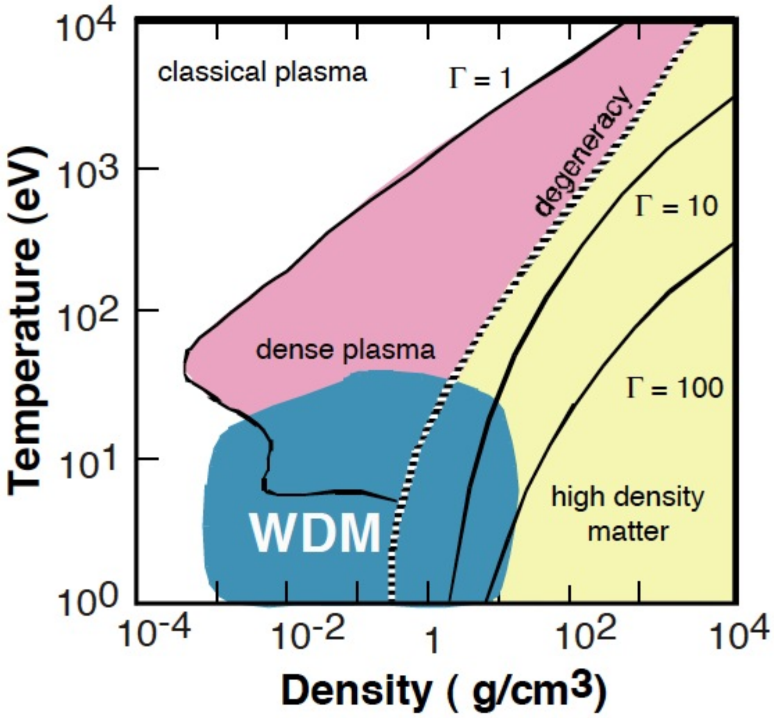

Figure 1.1: Temperature-density phase diagram of aluminium [16]. The WDM region is shown in blue, between ideal ($\Gamma \ll 1$) and strongly coupled, non-ideal ($\Gamma \gg 1$) plasmas, with near-solid densities and temperatures between 1 eV and a few tens of eV.

other metals, especially refractory ones, will be investigated in future work.

The interferometric system is designed to be deployed simultaneously with a fast multi-channel pyrometer on the same target area, in order to provide pressure and temperature histories of lead going through different vapour, liquid-vapour and liquid states. Interferometric measurements are performed on the free surface of a reflection coated sapphire window which is hit by ion-beam heated expanding lead, along a 1 mm line, with a modified Michelson interferometer imaging the area of interest onto a streak camera. Thermal radiation is collected over a 200 μm diameter spot situated on the same line, but on the impacted surface, using two off-axis parabolic mirrors which couple the light into a glass fibre that conveys it to a spectral analyser [15]. In order for simultaneous measurements to be possible, the light injection and collection system for the interferometer had to be integrated in the pyrometer head by means of a small transparent sapphire window inserted between the parabolic mirrors and the target window, coated to reflect only the diagnostic laser.

In the other part of this work, in experiments conducted at the Z6 area with PHELIX and nhelix, iron is studied in isentropic compression experiments, taking advantage of PHELIX's 15 ns long pulses and temporal pulse shaping capabilities. Using a flattened top-hat spatial intensity profile for PHELIX, planar compression can be achieved, in which a one-dimensional (1D) load is applied to iron foils 10-50 μm thick over a region roughly 1 mm in diameter. The goal is to reach pressures as high as possible without generating shocks that would increase the temperature too fast. This can be achieved by carefully choosing the foil thickness and the loading temporal profile. Surface velocity up to the km/s range is recorded with two imaging line VISARs (Velocity Interferometer System for Any Reflector), corresponding to pressure up to several hundred kbar.

As diagnostic laser, nhelix in a slightly modified configuration was used in the main experiment with PHELIX as compression driver, due to the coherence length of at least a few centimetres required by the line VISARs.

A review of the theoretical description of warm dense matter and principles of optical interferometry is given in Chapter 2, with an emphasis on velocimetry in Section 2.2.3.
In Chapter 3 are described the experiments performed at HHT with the imaging displacement interferometer, using sub-microsecond uranium beams at 350 AMeV and $\approx 3 \cdot 10^9$ ions per pulse. Interaction of ion beams and matter is discussed, and an overview of the accelerator facilities is given. Pressure and temperature results for lead are finally presented and analysed.
Chapter 4 focuses on the iron isentropic compression experiments that took place at Z6 with PHELIX and the imaging velocity interferometers, with a description of the laser facilities and the experimental configuration, followed by a discussion on the results that were obtained.
Conclusions and possible future applications of the diagnostic methods developed in this work are given in the closing Chapter 5, as well as improvements that could be made to them in the future.

2 Review of the field

This chapter contains an overview of the research that has been performed in the fields relevant to this work.

The first section gives a summary of the field of Warm Dense Matter generation and investigation, with the specific problems arising in each situation. Different dynamic methods of producing such states of matter are presented, an emphasis being put on results obtained at GSI using intense heavy ion beams.

In the second section an introduction to the field of optical interferometry is given first, and then the discussion is focused on the methods of velocity interferometry which can be applied in the investigation of matter under extreme conditions such as the WDM states.

2.1 Warm Dense Matter (WDM)

Warm Dense Matter (WDM) can be generally described as matter that is at densities comparable to the solid state (0.1-10 g/cm^3) and at temperatures in the range 1-100 eV. Key characteristics of these states of matter are the strong correlation between ions and electrons due to their Coulomb interaction and the degeneracy parameter around unity.

Theoretical modelling of matter in such states poses difficult problems. Because of the electron degeneracy generated by temperatures on the order of or greater than the Fermi energy it cannot be modelled with solid state physics methods. At the same time, the strong ion-ion coupling means that the Coulomb interactions cannot be considered just a perturbation to the thermal motion, therefore not allowing a classical plasma physics approach.

The correlation affects almost all aspects of WDM properties, it alters for example the resistivity and compressibility. Therefore specialized methods to analyse these properties are necessary and some of them will be presented in Section 2.1.2.

2.1.1 Generating warm dense matter

In almost all cases, WDM states of matter can be reached only by dynamic methods. Static methods such as the Diamond Anvil Cell in which high pressures are achieved by squeezing a solid sample between two diamonds are usually limited to low temperatures. Therefore only a review of the dynamic methods will be given in this section, as shown in Figure 2.1.

Short Pulse Lasers - SPLs

Using short pulse lasers, WDM is produced by heating a target either directly with a laser, or with a laser generated radiation source. For efficient generation of such states, the conditions of an idealized slab plasma [18] must be achieved, in which hydrodynamic expansion is minimized and isochoric conditions can be produced. Uniform heating is realized by selecting a sample thickness matched to the deposition range of the laser source, as well as the characteristic scale-length for thermal conduction. Thus usually very thin target foils on the order of tens of

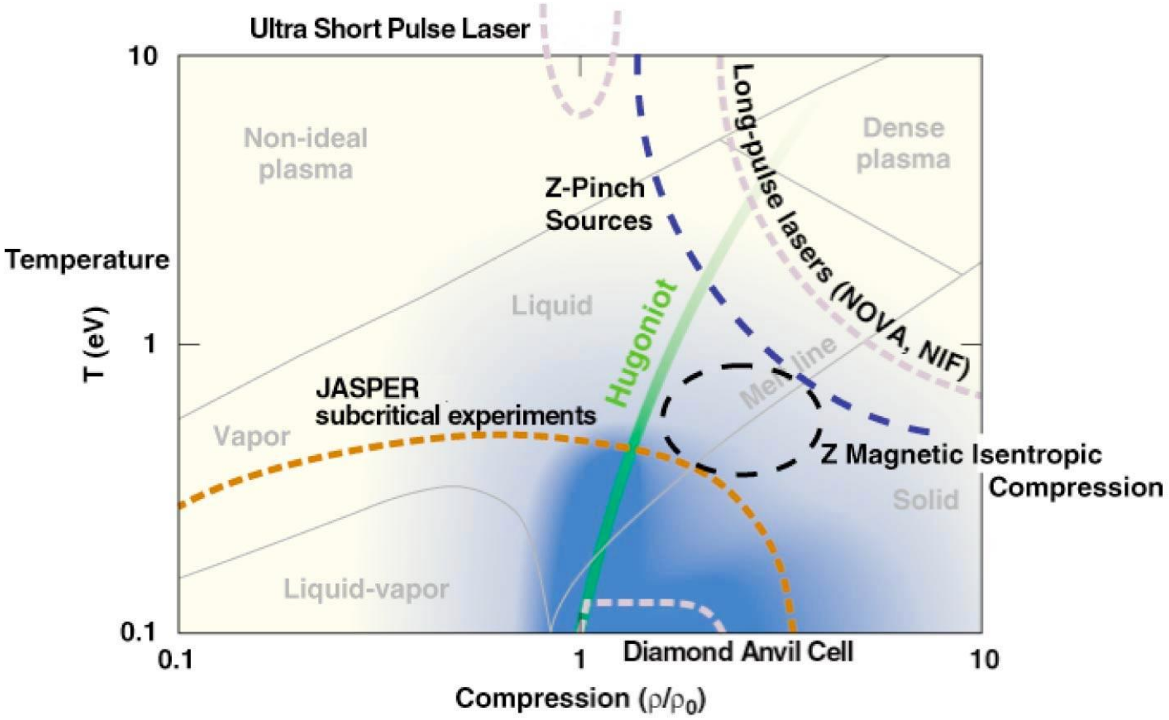

Figure 2.1: Experimental facilities and methods for generating WDM regimes [17]. JASPER refers to the Joint Actinides Shock Physics Experimental Research facility which is a two-stage gas gun designed to perform shock physics experiments, Z refers to the pulsed-power Z-pinch accelerator at Sandia National Laboratory.

nanometres are used with pulse durations around 100 fs generated by lasers such as the TESLA Test Facility (TTF) X-ray FEL at HASYLAB. In this type of experiments though, generally only very short lived transient states are achieved, which do not allow the best determination of the EOS.

High Energy-Density Lasers

High energy lasers are a flexible tool for studying different states of matter. Laser pulse shaping in combination with different driver configurations allows access to a wide range of the WDM phase space. Methods to compress and heat materials following isochoric, isobaric, isothermal, isentropic or implosion processes have been developed. A wide range of physical problems can be addressed using high energy lasers, ranging from phase transitions at the lowest temperatures to ionization phenomena at higher temperatures, due to their capability of generating pressures in the Gbar range and power and energy deposition levels on the order of PW/g and MJ/g, respectively.

Strong shock

In this configuraton, states along single-shock curves (also known as Hugoniot curves) are reached, at pressures up to the Gbar range [19], by launching a strong shock into a low-Z ablation layer through direct laser or X-ray irradiation.

Multiple shocks

Nearly isentropic compression can be obtained using a series of time delayed shocks generated as described above. For this method to be implemented, the laser system must have pulse shaping capabilities. These separate shocks may be used to compress a sample nearly isentropically to tens of Mbar at low temperature (<1 eV). For example, in aluminium compression experiments done with the NOVA laser, peak pressures of 1.8 Mbar were reached with a sequence of 3 shocks [20].

Flyer plate impacting

Pressures above 1 Mbar can be obtained by using a foil accelerated by direct laser or X-ray irradiation as an impactor to generate a shock. The flyer plate geometry is similar to the impactor configuration on a gas gun, but the target sizes and achieved time-scales are much smaller. An important difficulty in implementing this method is the growth of instabilities due to pre-existing defects in the flyer.

Isentropic compression

Isentropic compression can be performed either with a reservoir technique or with direct pulse shaping of the laser driver.

In the reservoir technique, a strong shock is launched in a material (for example a low density foam) which then unloads across a gap and accumulates against the sample material. Pressure in the target material increases with a ramp up to tens of Mbar. This approach to compression can be found in experiments at the OMEGA facilities. 20 μm Al foils were compressed up to several hundred kbar using a 7 ns square laser pulse incident on a thick foam layer [21].

In the direct pulse shaping technique, the laser pulse is temporally shaped for optimum ramp compression up to several Mbar, such as in experiments performed at LULI, or several hundred kbar in this work.

Isochoric heating

Volumetric heating can be achieved using high fluxes of X-rays and protons generated by short and long pulse laser-matter interactions. For example, using the Titan laser facility at the Lawrence Livermore National Laboratory (LLNL) [22], with laser pulses of 100 J, 500 fs long at 1 μm wavelength focused on a spot under 10 μm on 15-25 μm thick Al or Au foils, MeV protons were created which afterwards heated isochoricaly thin foils of aluminium to WDM states.

Implosions

In inertial confinement fusion related experiments such as the ones performed at NIF [23], spherical capsules of deuterium are loaded using multiple shocks and isentropic compression to extreme states of density around 10^3 g/cm^3 and temperature of 100 eV.

Isobaric Expansion Technique - IEX

In experiments employing this method a high electrical current is discharged through a metal wire placed in a containment vessel. Using this technique, compared to the shock wave one, thermodynamically complete EOS data are obtained by measuring pressure, temperature and volume. For example, states of matter up to 15 kbar in pressure and 40,000 K in temperature were reached for various metals, limited by the material strength of the containing vessel [24].

Heavy Ion Heating and Expansion - HIHEX

Intense focused heavy ion beams can be used to heat large volume targets uniformly and quasi-isochorically, generating thus states of high pressure and high entropy. Through isentropic expansion, depending on the deposited energy, the material can reach afterwards various regions of the phase diagram: hot liquid, the critical point region, two-phase liquid-gas states, strongly coupled plasmas and WDM states. The range of materials that can be used is very broad: gases, metals, oxides.

During the last 10-20 years extensive theoretical and experimental work [7, 25, 26, 27, 28] has been performed on this method, demonstrating its applicability to generating macroscopic volumes of HED matter.

Experimental work using this method has been carried out since 2003 in the plasma physics department of GSI. In particular the "Heavy Ion Heating and Expansion" experimental concept (HIHEX) has been developed and employed [29].

Given present beam parameters at GSI, the level of specific energy deposition in solid lead is of a few kJ/g with which generation of HED states at solid state densities with temperatures up to $\approx$2 eV and pressures in the multi-kbar range is possible.

2.1.2 Investigating properties of warm dense matter

Various methods exist for investigating the physical properties of warm dense matter.

Pressure measurements can be done directly with pressure gauges or indirectly by recording the spatial dynamics with displacement or velocity interferometers.

Temperature is analysed using spectrometric methods, in which pyrometry plays an important role.

The microscopic structure, charge states and opacity of WDM samples can be investigated with X-ray radiation. Due to the transient nature of WDM states, usually diagnostic resolution times on the sub-nanosecond scale are required, near the limit of most current X-ray sources. With this technique, the phase space around solid density and temperatures up to 1 eV can be analysed.

An introduction to some of these methods will be given below.

X-ray radiography

Target samples can be radiographed with high intensity X-rays during shock propagation or foil surface motion, for example exploding titanium wires [30].

Absorption spectroscopy

This method is used to study the spectroscopic structure of a highly ionized plasma in order to obtain the pressure and density of the plasma or to characterize the temperature and density of solid samples in extended X-ray absorption fine structure spectroscopy (EXAFS).

In EXAFS measurements, lattice order information is obtained by observing the modulation in absorption frequency and amplitude occuring near absorption edges, as for example in experiments performed with Ti foils [31].

Bragg diffraction

X-rays diffracted on the lattice structure of a material under compression can be recorded with angular resolution on X-ray streak cameras to observe the lattice response to dynamic loading. This technique of in-situ dynamic Bragg diffraction was demonstrated using the Nova and OMEGA lasers for shock compressed single crystals of Si and Cu, with X-rays at a wavelength of 1.85 Å created by a laser beam hitting a thin Fe foil. The X-rays were diffracted at the Bragg angle corresponding to both the uncompressed lattice and the compressed lattice spacing as the shock propagated through the sample, thus allowing a direct measurement of the lattice spacing evolution during target loading [32].

X-ray Thomson scattering

X-ray Thomson scattering may be used to measure directly plasma parameters like temperature, free electron density, degree of ionization and the microscopic structure of warm dense matter samples.

This technique has been demonstrated in experiments using the OMEGA laser in which a heated Be target was investigated by X-rays created from a Ti foil. The resulting Thomson scattered spectrum was both Compton downshifted and Doppler broadened [33].

Other experiments were performed at GSI with nhelix compressing a carbon target and PHELIX irradiating a Ti foil as X-ray generator [34].

X-ray opacity

Changes in opacity can be recorded and linked to phase transitions, as has been shown with compressed Al heated to 1 eV [35].

Optical velocimetry

Optical velocimetry techniques are used to characterize the compression in loaded materials in different experimental configurations. EOS measurements have been done on various materials at the NOVA [36] and OMEGA [37] laser facilities, implementing this kind of methods.

Pressure gauges

In contrast to the technique of optical velocimetry, pressure can also be directly measured with piezo-electric gauges embedded in the target. Experiments have been performed at GSI using such gauges to study ion beam interaction with solid lead targets [38].

Pyrometry

Contactless temperature measurements can be performed using pyrometers adapted to the temperature range and time scale of the given experiments. This technique is used in the present work in the visible and near-infrared spectral regions up to 1-2 eV, deploying a nanosecond fast multi-channel configuration developed in [15, 39, 40].

2.2 Optical interferometry

Optical interferometry, as a field of study, spans over more than 300 years. From the discovery of Newton's rings in the 17th century, through the development of the classical electromagnetic theory of light, to the present quantum description of light, it has provided both new information on the nature of light itself, as well as important tools used in analysing other physical phenomena.

With the advent of lasers in the second half of the 20th century, optical interferometry underwent a rapid development as an important method of diagnostic.

In the following sections a review of the development of this field and its applications will be given.

2.2.1 Wave theory of light

In 1690, in his *Traité de la lumiere*, Huygens develops and gives its current form to Hooke's wave theory of light: "J'ay donc monstré de quelle façon l'on peut concevoir que la lumière s'etend successivement par des ondes spheriques" [41]. For more than a century though, it was not accepted by scientists, especially by Newton who developed a corpuscular theory of light. Only in 1801 and 1803, in his Bakerian lectures [42, 43], Young proposes the principle of interference, which is perfected in 1818 by Fresnel. He and Arago discover that two orthogonally polarized light beams cannot interfere, which leads Young and Fresnel to the idea that light waves must be transversal waves, not longitudinal ones as they have previously thought. Fresnel introduces the concept of a "luminiferous aether" which pervades everything and through which light waves propagate. Michelson carries out an experiment trying to demonstrate the "aether drift" in 1881, but the results showed that the "luminiferous aether" does not exist and set the basis for the special theory of relativity[44].

Light was finally discovered to be an electromagnetic wave which propagates according to Maxwell's laws. Even though it has an electric field component $\overrightarrow{E}$ and a magnetic field component $\overrightarrow{B}$, only the electric field $\overrightarrow{E}$ is detectable by sensors (including the human eye).

For the simplest case of a linearly polarized plane wave propagating in a vacuum in the z direction, the magnitude of the electric field $\overrightarrow{E}$ can be written as:

$$E = a\cos\left[2\pi\nu\left(t - z/c\right)\right], \tag{2.1}$$

where a is the amplitude, ν the frequency, and c the propagation speed of the wave.

In complex representation we have:

$$E = \mathrm{Re}\left\{a\exp\left[\mathrm{i}2\pi\nu\left(t - z/v\right)\right]\right\}, \tag{2.2}$$

where Re stands for the real part of the bracketed expression and i is the imaginary unit. It follows that E can be written as

$$E = \mathrm{Re}\left\{a\exp\left(-\mathrm{i}\phi\right)\exp\left(\mathrm{i}2\pi\nu t\right)\right\}, \tag{2.3}$$

where

$$\phi = 2\pi\nu z/v, \tag{2.4}$$

is the phase difference corresponding to the optical path between the origin and the point z. Therefore, the electrical field can be described by a complex function:

$$E = A \exp(\mathrm{i}2\pi \nu t), \tag{2.5}$$

where $A = a \exp(-\mathrm{i}\phi)$ is the complex amplitude of vibration. To obtain usable data, at the end of calculations only the real part is to be considered.

In actual experiments, the electrical field cannot be directly observed due to the high frequency of visible light waves ($\nu \approx 10^{14} Hz$). What can be measured by detectors is the intensity of light, that is the amount of energy which, in unit time, crosses a unit area normal to the direction of energy flow. The intensity is proportional to the time average of the square of the electric field:

$$I \propto \left\{E^2\right\} = \lim_{T \to +\infty} \frac{1}{2T} \int_{-T}^{T} E^2 \, dt = a^2/2. \tag{2.6}$$

Finally, the optical intensity can be defined as

$$I = a^2 = A^2. \tag{2.7}$$

Of practical interest is the formula for the total electric field generated by two monochromatic waves propagating in the same direction and polarized in the same plane, given by

$$E = E_1 + E_2, \tag{2.8}$$

where E_1 and E_2 are the electrical fields of the two waves.

For waves having the same frequency, the resulting intensity will be

$$I = |A_1 + A_2|, \tag{2.9}$$

where $A_1 = a \exp(-\mathrm{i}\phi_1)$ and $A_2 = a \exp(-\mathrm{i}\phi_2)$ are the complex amplitudes of the two waves. Two such waves are said to interfere, resulting in a final intensity

$$I = A_1^2 + A_2^2 + A_1 A_2^* + A_1^* A_2 = I_1 + I_2 + 2\left(I_1 I_2\right)^{1/2} \cos \Delta\phi, \tag{2.10}$$

where $I_1 = |A_1|^2$, $I_2 = |A_2|^2$ and $\Delta\phi = \phi_1 - \phi_2$.

The visibility of the interference fringes is defined by

$$V = \frac{\left(I_{max} - I_{min}\right)}{\left(I_{max} + I_{min}\right)}, \tag{2.11}$$

For monochromatic light, it follows from Eqs. 2.10 and 2.11 that

$$V = \frac{2\left(I_1 I_2\right)^{1/2}}{\left(I_1 + I_2\right)}. \tag{2.12}$$

Given the finite time duration of these waves in real situations, a coherence length can be introduced and defined as the optical path length difference which corresponds to a $1/e$ decrease in fringe visibility, in a Michelson interferometer, compared to the situation in which both arms have the same length.

In order to obtain two beams of interfering light, two methods can be used and will be described: **Wavefront division** and **Amplitude division** of an initial optical field.

Wavefront division

The method of wavefront division consists in splitting the original wavefront in two spatially different portions, which afterwards are superimposed to obtain interference. Optical systems that use this method are Fresnel's mirrors, Young's double slit and Lloyd's mirror.

Amplitude division

Two beams can also be obtained by dividing the amplitude over the same section of the wavefront, for example by using a surface that reflects part of the incident light and transmits part of it. Depending on the nature of the source of monochromatic light and optical system used to recombine the beams, several types of fringe patterns can be obtained, of which some will be described below.

Fringes of equal inclination will be produced by reflection of a point source on the sides of a plane-parallel plate.

Fringes of equal thickness (Fizeau fringes) are created using a collimated beam of light in a plate with small variations of thickness - collimated beam of monochromatic light, at near-normal incidence.

Fringes of equal thickness in a thin film can be obtained using an extended source of monochromatic light.

2.2.2 Typical interferometer configurations

Interferometers are optical systems with which phase differences between two interfering beam of light can be measured. These phase difference measurements translate, depending on the type of interferometer, to density, displacement, velocity and many other physical properties.
The general configuration of an interferometer consists in having two arms through which the interfering beams of light pass different conditions.
A short review of some of the existing types of interferometers will be given. From these, two were used in a modified form in experiments at GSI.

Michelson interferometer

The classical example of a system which uses the division of amplitude interference is the Michelson interferometer [44] illustrated in Figure 2.2a. A beam splitter divides the input beam of light into two beams which travel different distances to two mirrors M1 and M2. After being reflected they are recombined by the same beam splitter and focused by the lens L on a detector. Ideally, to obtain uniform illumination over the detector, the input light must be perfectly collimated. In practical cases though, there is still some angular distribution in the input beam and concentric zones of non-uniform illumination are created on the detector.
To demonstrate this effect, it is useful to consider the equivalent optical system of the Michelson interferometer shown in Figure 2.2b.

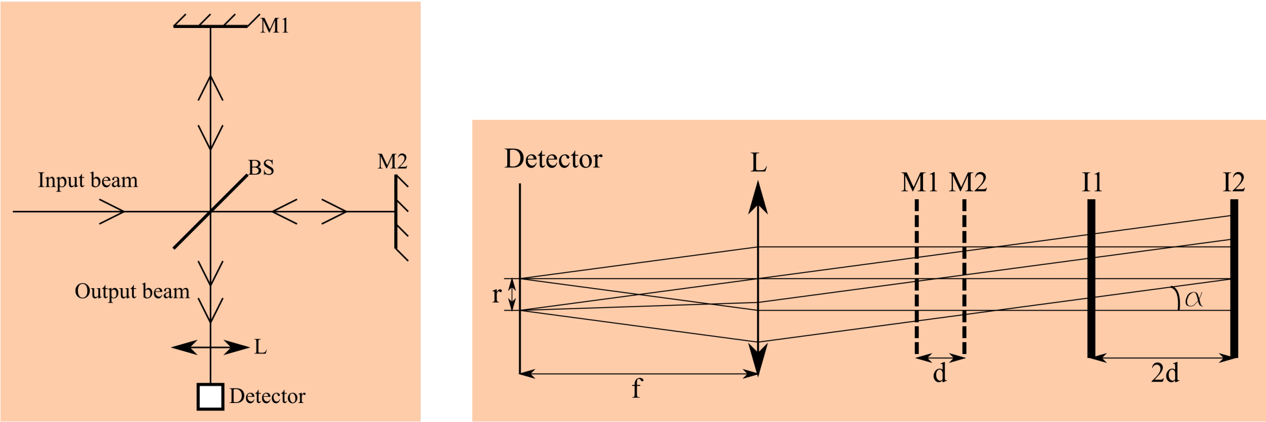

(a) The Michelson interferometer. **(b)** Equivalent optical system.

Figure 2.2: Michelson interferometer configuration.

From the point of view of the detector, the beam splitter and mirrors create two virtual images I1 and I2 of the input. The intensity pattern on the detector corresponds to either a series of circular fringes for parallel mirrors (Haidinger fringes or fringes of equal inclination), or, if the mirrors are tilted, to parallel fringes (Fizeau fringes or fringes of equal thickness).

In the case of Haidinger fringes, for small mirror separations, the spot size on the detector is comparable to the focal length of the focusing lens in front of the detector, leading to uniform illumination. However, for large mirror separations, large intensity variations appear on the surface of the detector. In principle, using sufficiently small detectors, the intensity distribution issues could be mitigated but at the expense of heavily reduced signal levels.

Mach-Zehnder interferometer

The Mach-Zehnder interferometer illustrated in Figure 2.3 uses two beamsplitter BS1, BS2, and two mirrors M1, M2 to divide and recombine light from a source S. Usually, BS1, BS2, and M1, M2 are adjusted so that they are approximately parallel, the paths traversed by the beams of light forming thus a rectangle or a parallelogram.

Due to the widely separated beam paths which are each traversed only once, and fringe localization which can be done in any plane, it is more versatile than the Michelson interferometer and has been used extensively in studies of gas flow, combustion, plasma density, and diffusion. In these type of experiments, a change in refractive index in one of the arms can be related to changes in pressure, temperature or relative concentrations of different components of a mixture.

Wide angle Michelson interferometer

By inserting a transparent window in one arm of the interferometer such that the virtual image I2 in 2.2b is superposed on the virtual image I1, the problem of the non-perfectly collimated

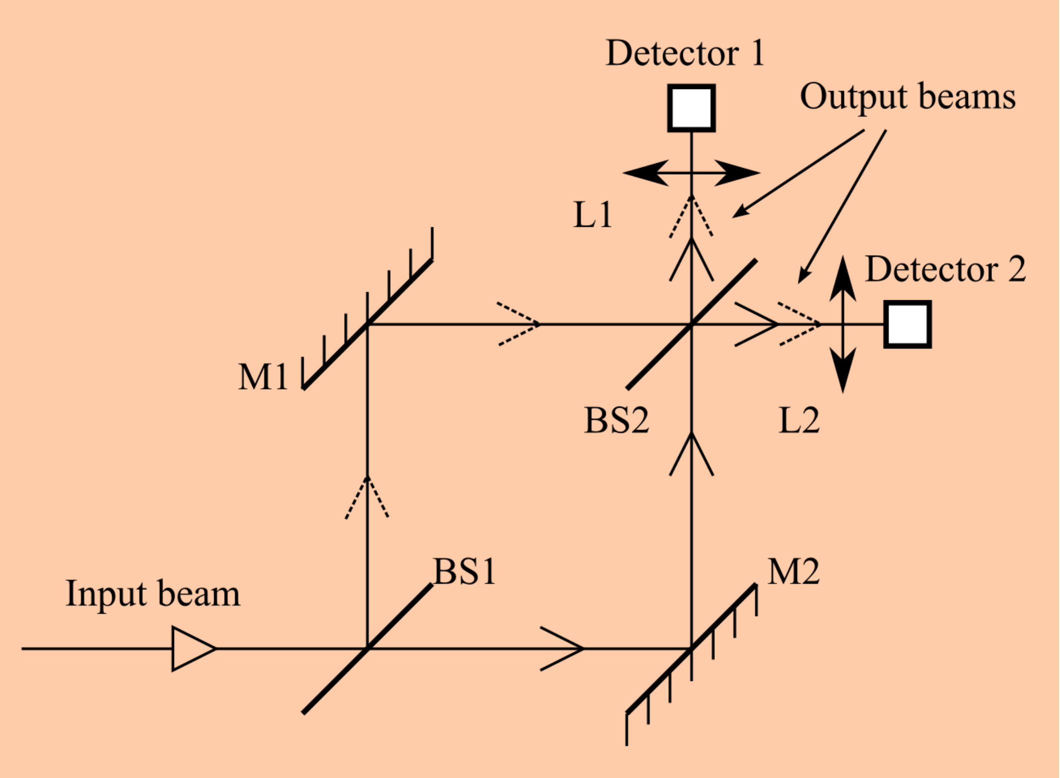

Figure 2.3: The Mach-Zehnder interferometer. Two output planes can prove useful in imaging interferometer alignment (see Section 2.2.3) or phase quadrature data reduction schemes (see Section 2.2.3).

input beam is solved. An interferometer with this configuration is called a wide angle Michelson interferometer (WAMI) [45]. The detector is uniformly illuminated, but at the same time, due to the existing difference in arm lengths (which induces a relative time delay) the recombined light beams still interfere. Given this time delay τ, the detected output signal is

$$D(t) = a_1^2 I\left(t - t_1\right) + a_2^2 I\left(t - t_1 - \tau\right) + 2a_1 a_2 \sqrt{I\left(t - t_1\right) I\left(t - t_1 - \tau\right)} \cos \Delta\phi\left(t\right) \qquad (2.13)$$

2.2.3 Optical velocimetry

Velocimetry as a general field of study concerns itself with the measurement of the velocity of materials under various dynamic conditions. In this section an introduction to interferometric based methods of velocimetry applied to moving surfaces will be given.
Velocimetry measurements relying on the optical phase can be performed either through **displacement measurements**, or through **direct velocity determination** from the optical phase.

Displacement measurements are performed by placing the surface under study in one of the arms of an interferometer such as the ones described in Section 2.2.2, and recording the phase difference between the arms, which can usually be related to the displacement in the following way:

$$\Delta x = \frac{\Delta\phi}{2\pi}\frac{\lambda}{2}, \qquad (2.14)$$

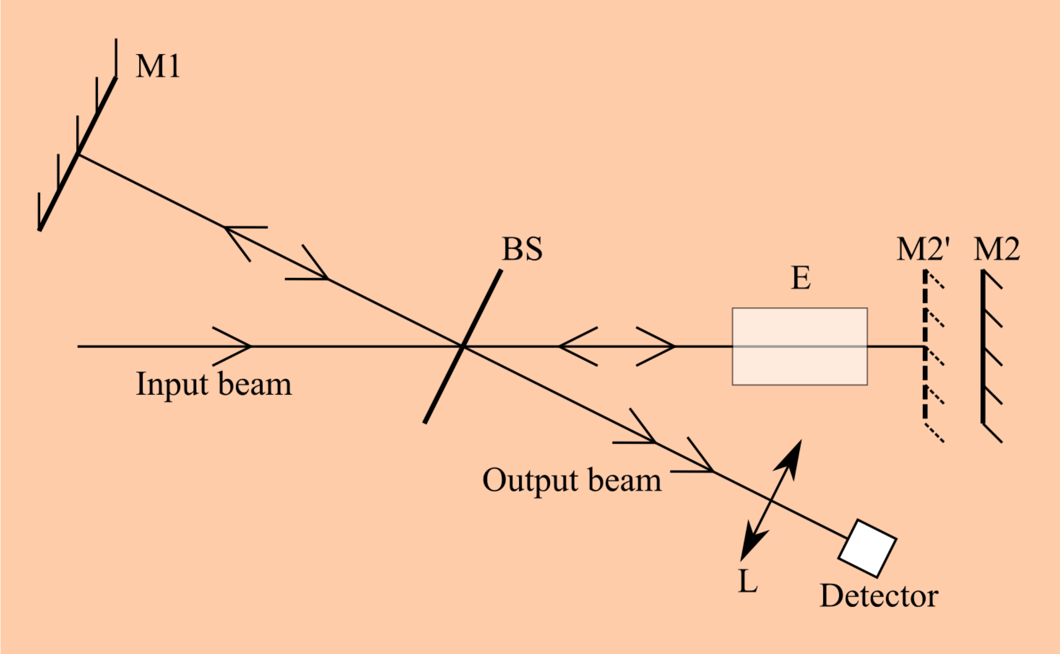

Figure 2.4: Schematics of the wide angle Michelson interferometer (WAMI).

Δx being the displacement, $\Delta\phi$ the phase difference and λ the wavelength of the light source used as diagnostic.

This kind of measurements are limited though to targets which have a surface of very good optical quality.

Direct velocity determination relies on the relativistic Doppler effect. Light of wavelength λ_0, reflected off a a moving surface, has a new wavelength λ given by

$$\lambda = \lambda_0 \frac{1 - v/c_0}{1 + v/c_0}. \tag{2.15}$$

For $v/c_0 \ll 1$ (usually under 0.001)

$$\lambda/\lambda_0 \approx 1 - 2v/c_0. \tag{2.16}$$

Thus, by analysing light reflected from a surface in motion, usually using a WAMI or modified Mach-Zehnder interferometer configuration in which the arms are of different length, velocity can be directly related to the observed phase change. Compared to displacement measurements, direct velocity determination can be used for target surfaces of various optical quality.

A special type of interferometer with which this method can be implemented and which will be used extensively in this work is described below.

Velocity Interferometer System for Any Reflector - VISAR

In [46], using a WAMI (Wide Angle Michelson Interferometer) modified configuration, Backer and Hollenbach estimated the velocity of a diffusely reflecting surface by measuring the above

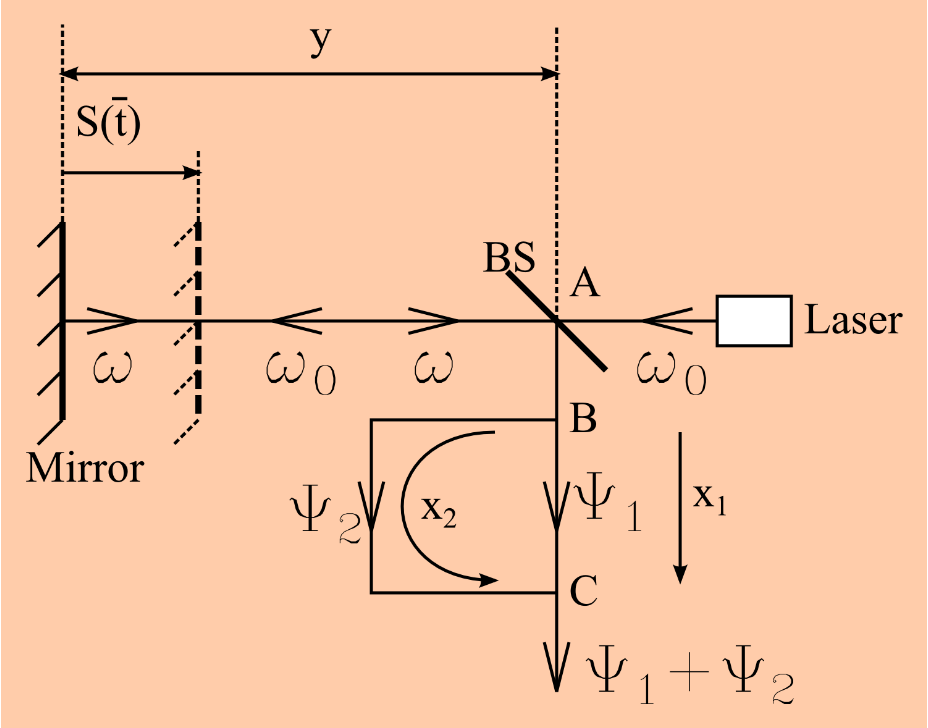

Figure 2.5: Working principle of the laser velocity interferometer [47].

mentioned Doppler shift. Essentially, it can be described as two WAMIs working on two polarizations of the input, one of the polarization being phase-shifted to the other with a 1/8 wave plate. Each polarization hits a dedicated detector and through certain data reduction techniques is analysed to obtain the velocity of the surface.

A thorough analysis of this velocity interferometer is given in [47]. The approximations made in [46] are examined and conditions in which they are valid are derived. Following the approach taken in [47] and referring to Figure 2.5, the time dependence of the amplitude of the non-monochromatic light at C is obtained by examining the propagation of wave crests leaving A, after reflection on the target surface. Point B will be considered to coincide with A, the representation in Figure 2.5 with A and B separated is just for convenience.

First, at position A, light going towards the target is monochromatic of angular frequency ω_0, so that its amplitude may be represented by

$$\Psi^A(t) = \cos(\bar{\delta} + \omega_0 t) \tag{2.17}$$

where $\bar{\delta}$ is an arbitrary constant.

Crests leaving A at time T hit the mirror at position $S(\bar{t})$ at time $\bar{t} = T + [y - S(\bar{t})]/c$ and arrive back at A at time $\bar{t} + [y - S(\bar{t})]/c + \tau_D$, where τ_D is the reflection delay time. Hence

$$\Psi^B\left(\bar{t} + \tau_D + \frac{y - S(\bar{t})}{c}\right) = \Psi^A(T) = \cos\left[\bar{\delta} + \omega_0\left(\bar{t} + \frac{S(\bar{t}) - y}{c}\right)\right]. \tag{2.18}$$

The delay time τ_D corresponds to the phase shift suffered at reflection on the target and is around 10^{-17} s, representing a phase shift of $3 \cdot 10^{-2}$ rad, which in practical experiments does not change by more than $3 \cdot 10^{-6}$ rad during the measurement. This change can be neglected, as it produces no distinguishable movement of the fringes.

Light leaving the mirror at time T arrives back at A at time $\bar{t} - \left[S(\bar{t})/c - y/c\right]$, therefore a more convenient variable can be defined as $t = \bar{t} - S(\bar{t})/c$.

At point B, the phase ϕ_B can be extracted from $\Psi^B = \cos(\phi_B)$ as

$$\phi_B(t + y/c) = \phi_B(y/c) + \omega_0 \left[t + 2S(\bar{t})/c\right], \tag{2.19}$$

where $\phi_B(y/c) = \bar{\delta} - y\omega_0/c$.

Ψ_1^C, Ψ^B and Ψ_2^C contain the same phase information, but at different times $t+(x_1+y)/c$, $t+y/c$ and $t+\tau+(x_1+y)/c$, respectively, where $\tau = (x_2 - x_1)/c$ is the difference in time it takes light to go through the arms of the interferometer. Considering that light is split at point B usually in two parts of equal intensity, we obtain

$$\Psi_1^C\left(t + \frac{x_1+y}{c}\right) = \frac{1}{2}\Psi^B\left(t + \left(\frac{y}{c}\right)\right) = \Psi_2^C\left(t + \tau + \frac{x_1+y}{c}\right). \tag{2.20}$$

From Eq. 2.19 it follows that

$$2\Psi_1^C\left(t + \frac{x_1+y}{c}\right) = \cos\alpha_1; \quad 2\Psi_2^C\left(t + \frac{x_1+y}{c}\right) = \cos\alpha_2, \tag{2.21}$$

where $\alpha_1 = \cos\left[\phi_B\left(\frac{y}{c}\right) + \omega_0\left(t + \frac{2S(\bar{t})}{c}\right)\right]$ and $\alpha_2 = \phi_B\left(\frac{y}{c}\right) + \omega_0\left(t - \tau + \frac{2S(\overline{t-\tau})}{c}\right)$. The intensity after interference at point C is given by

$$I = \left(\Psi_1^C\right)^2 + \left(\Psi_2^C\right)^2. \tag{2.22}$$

Considering Eq. 2.21, we obtain

$$I\left[t + \left(x_1 + y\right)/c\right] = \frac{1}{4}\left[1 + \cos\left(\alpha_1 - \alpha_2\right) + \cos\left(\alpha_1 + \alpha_2\right) + \frac{1}{2}\left(\cos 2\alpha_1 \cos 2\alpha_2\right)\right]. \tag{2.23}$$

The high-frequency terms in the interference pattern at C can be ignored. For visible light, the term has a frequency around 10^{15} $(1 + 2U/c)$ Hz. In the experiments described in this thesis, the total observation time is around 10 ns, and the time resolution can go to 10 ps. Even in this case, over a response time of 10^{-12} s, the terms integrate to zero very well, if the measured velocities are roughly under $c/5$, as shown in [47].

As the $\frac{1}{4}$ factor is just a proportionality coefficient, it can be ignored and the final expression for the intensity at point C calculated as

$$I\left[t + \left(x_1 + y\right)/c\right] = 1 + \cos\omega_0\left[\tau + \frac{2S(\bar{t}) - 2S(\overline{t-\tau})}{c}\right] \tag{2.24}$$

The usual velocity interferometer equation

$$I\left[t + \left(x_1 + y\right)/c\right] = 1 + \cos\left[\omega_0\tau + \frac{\omega_0\tau}{c}U\left(\overline{t - \tau/2}\right)\right] \tag{2.25}$$

can be obtained from 2.24 by replacing $S(\bar{t}) - S(\overline{t-\tau})$ with $\tau U(\overline{t - \tau/2})$, for small enough τ.

Finally, the formula

$$\frac{\omega_0}{24\pi c}\left(\ddot{U} + \frac{3\dot{U}^2}{c}\right)\tau^3 \ll 1 \tag{2.26}$$

is derived as condition for the validity of the usual velocity interferometer equation [47]. Applying Eq. 2.26 to the experimental conditions of this work in which $\dot{U}$ is under 10^{13} m/s^2 and $\ddot{U}$ is at most on the order of the acceleration term, results that τ should be sensibly smaller than 10^{-8} s.

Push-pull VISAR

A modification to the conventional VISAR was proposed in [48] in which the light going back through the beam splitter in the WAMI configuration is used to improve efficiency. In a conventional VISAR, half of the light entering the system does not reach the detectors, but is lost by transmission through the beam recombination beam splitter. This light can be used by a second set of detectors. By subtracting the signals corresponding to each polarization, the background signal is eliminated. They can be written as a simplified form of Eq. 2.25 in the following way

$$I_x = [\sin(\Phi(U)) + B] - [\sin(\Phi(U)) + B] = 2\sin(\Phi(U)), \tag{2.27}$$

$$I_y = [\cos(\Phi(U)) + B] - [\cos(\Phi(U)) + B] = 2\cos(\Phi(U)). \tag{2.28}$$

where $\Phi(U)$ represents how the optical phase difference Φ between the two arms changes with observed velocity U and can usually be written as

$$\Phi(U) = \omega_0 \tau (1 + U/c). \tag{2.29}$$

Finally, the velocity is given by

$$U(t) = \Phi^{-1}\left(\arctan\frac{I_x}{I_y}\right). \tag{2.30}$$

In experiments where background intensities are high and signal levels varying, the 'push-pull' technique greatly reduces the uncertainties in velocity analysis.

Imaging VISAR

A classic VISAR can be extended to an imaging VISAR, in which velocity is measured on a surface instead of a single point [36, 37, 49]. The ambiguities in fringe movement (related to velocity direction) inherent to a point VISAR can be solved in this way, besides obtaining 2D data. Therefore, in more recent work such as [36, 37] polarized light is not used any more, compared to the work performed in [49] in which an imaging 'push-pull' configuration is used. In practical applications, only a line-profile of the velocity is recorded, usually on streak cameras such as the ones described in Section 3.4.3. In the case of shocks, fringe jumps appear.

An imaging VISAR was used in this work, therefore a detailed description of this interferometer will be given in Section 4.4.1, together with the corresponding experiment configuration.

2.2.4 Interferogram analysis

The results obtained with imaging interferometers usually take the form of interferograms, pictures of interference patterns. In each point of these images the optical phase can be calculated by analysing the fringe pattern in the entire interferogram.

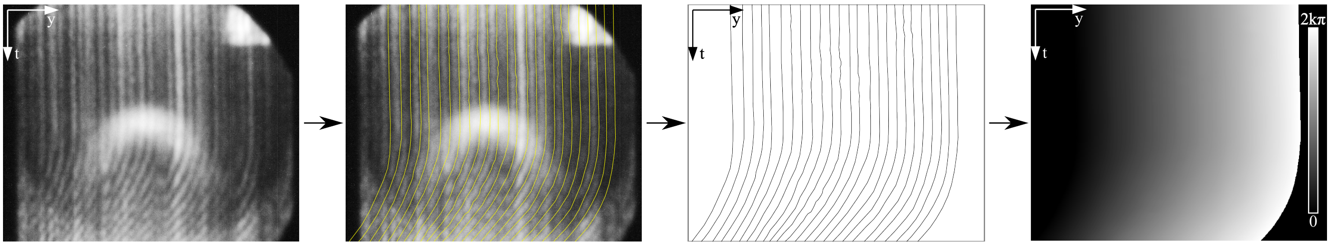

Figure 2.6: Skeletonizing of fringes along minima and phase-map interpolation.

Fringe tracing

The most direct way of analysis is by tracing the fringes along their local extrema, indexing them, setting the value of pixels on the fringes as integer multiples of 2π proportional to the fringe indices and finally interpolating across all the other pixels to get a complete phase-map. The fringe tracing can be done manually or automatically. In Figure 2.6 a manually traced interferogram is shown, with the corresponding phase-map resulting after interpolation and unwrapping to values outside $[0, 2\pi]$.

Methods for automatic fringe tracing work well only for interferograms with little noise, in all the other cases manual fringe tracing must be performed.

Fourier Transform based methods

An alternate way of obtaining the phase-map is by looking at the Fourier transform of the image, introduced by [50] as the Fourier Transform Method (FTM). Following the approach in [37], the FTM begins by assuming that the recorded fringe intensity can be represented as a real-valued function, given by

$$S(x,t) = B(x,t) + A(x,t)\cos\left[\phi(x,t) + 2\pi f_0 x + \delta_0\right]. \tag{2.31}$$

The background pattern can be considered to have a constant fringe frequency f_0 and phase offset δ_0, though in practice, due to imperfections in the interferometer optics and distortions introduced by the recording camera, it varies slightly. Information about the actual phase map is contained in $\phi(x,t)$, which is a phase modulation superimposed on the carrier wave $2\pi f_0 x + \delta_0$. The function $B(x,t)$ represents a slowly varying background intensity, or the average unmodulated signal intensity, while $A(x,t)$ represents the fringe amplitude, such that $|A| \leq B$. An equivalent representation of Eq. (9) is

$$S(x,t) = B(x,t) + C(x,t)\exp\left(2\pi \mathrm{i} f_0 x + \mathrm{i}\delta_0\right) + const. \tag{2.32}$$

where $C(x,t) = A(x,t)\exp\left[\mathrm{i}\phi(x,t)\right]/2$. By computing the one dimensional Fourier transform over x, at fixed y, the background function $b\left(f,t\right)$ can be separated from the phase information contained in c, as given by

$$s\left(f,t\right) = b\left(f,t\right) + c\left(f - f_0, t\right) + c^*\left(f - f_0, t\right) \tag{2.33}$$

After that only a range of the power spectrum around the c-lobe at positive frequencies is selected, the rest of the spectrum is set to zero (including the negative frequencies in c^*).

Applying the inverse Fourier transform results in the complex valued function

$$D(x,t) = C(x,t)\exp\left[2\pi \mathrm{i} f_0 x + \delta_0\right]. \tag{2.34}$$

The wrapped phase can be obtained from this function as

$$W(x,t) = \arctan\left[\mathrm{Re}(D), \mathrm{Im}(D)\right]. \tag{2.35}$$

The wrapped phase function $W(x,t)$ can then be unwrapped to obtain the original phase.
By applying the bandpass spatial filter, the resolution is decreased. Finally, it depends both on the fringe density and the filter bandwidth. A rough resolution estimation is that the number of independently resolvable spatial elements available for velocity extraction is a few per fringe.

3 Study of near critical states of metals by intense heavy ion beams

We have studied thermodynamic properties of metals, focusing on lead in high energy density (HED) states at $2 - 20 \cdot 10^3$K and 0.01 – 10 GPa, using an intense heavy ion beam of SIS-18 synchrotron as a driver. Numerical simulations have shown [7] that with the HIHEX technique, using beam intensities between 10^9 - 10^{12} uranium ions per bunch, the entire phase diagram of many materials of interest can be studied. The critical temperatures and densities of many metals, as shown in 3.1, are such that traditional shock wave methods cannot achieve them simultaneously. However, using isochoric and uniform heating of matter with intense heavy ion beams, followed by isentropic expansion of the heated material, the required temperatures can be easily achieved by depositing the corresponding specific energy in the sample.

The EOS of lead in P-ρ-T variables can be seen in Figure 3.1. The following regions are marked: M - melting region, H - principal and porous Hugoniots, DAC diamond anvil cell data, IEX - isobaric expansion data, S - release isentropes, R - boundary of two-phase liquid-gas area and the critical point, lines of constant ionization degree α and plasma non-ideality parameter γ.

Evaporation, condensation and compression of a material in two-phase liquid-gas states near its binodal, spinodal and the critical point, metal – dense plasma transition were investigated in this work using optical diagnostic techniques such as fast multichannel pyrometry/reflectometry and imaging interferometry. As can be seen in Table 3.1, the critical region of lead is around 5000 K and 2 kbar, a temperature and pressure range which can be achieved with current uranium beam intensities available at GSI.

For further studies of refractory metals, such as tungsten and tantalum, higher intensities are required, which will be provided by the new accelerator facilities at FAIR. In this chapter, first a theoretical description of the interaction of ion beams with matter is presented, then a review of the accelerator facilities of GSI. Afterwards a detailed description of the diagnostic instruments that were used is given, followed by the results obtained during beam-time experiments at the HHT area of GSI.

3.1 Interaction of ion beams with matter

The main energy loss mechanism for energetic heavy ions (energies above 1 AMeV) is the energy transfer to the target electrons. Given the fact that the main interest in this work lies in using heavy ion beams to heat matter, elastic (Coulomb) nuclear collisions are neglected due to the mass ratio factor m_e/m_i and nuclear reactions (inelastic nuclear interactions) at the energies relevant to this study are also ignored.

Ions can transfer their energy to bound electrons in the target material in cold stopping processes, or to free electrons in pre-ionized materials (such as plasmas).

Some theoretical aspects of cold stopping will be given in the following section, given that this is the method for obtaining WDM states of lead in this work.

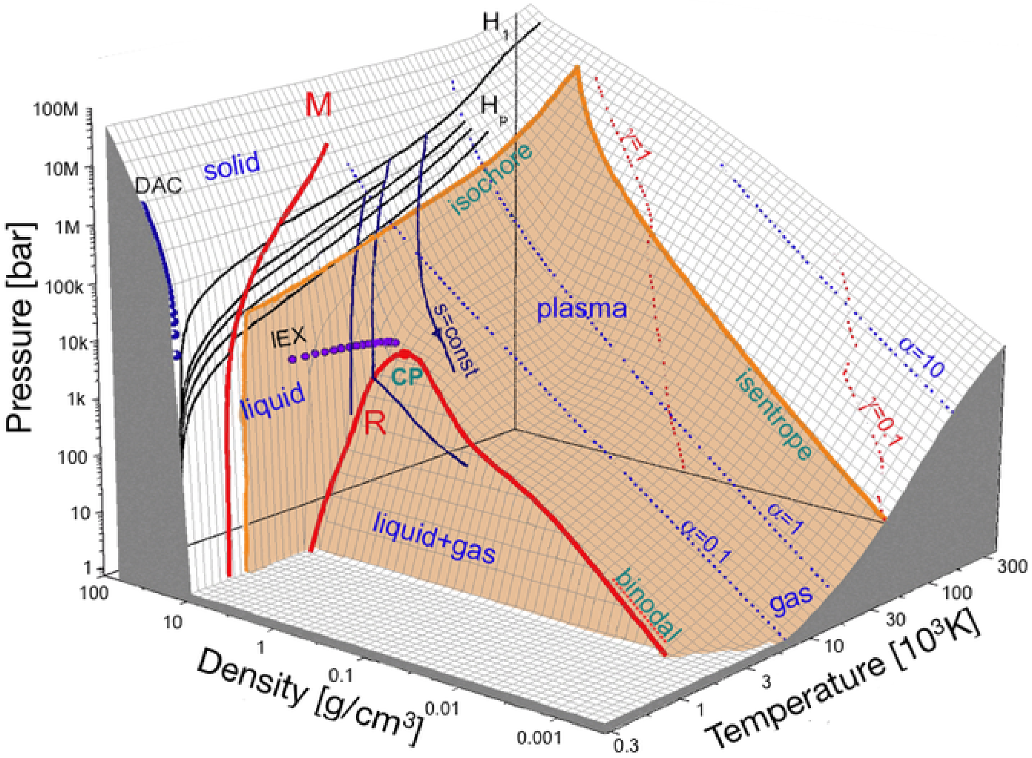

Figure 3.1: Phase diagram of lead [29].

	T_c(K)	P_c(kbar)	ρ_c(g/cm^3)
Lead	5500	2.30	3.10
Gold	8500	6.14	6.10
Zinc	3080	3.30	2.40
Copper	7800	9.00	2.28
Silver	7050	10.64	3.28
Beryllium	8600	2.00	0.40
Iridium	11650	6.20	3.10
Tin	8175	2.39	1.59
Uranium	9650	7.70	4.5
Aluminum	6390	4.45	0.86
Tungsten	13500	3.10	2.17
Niobium	19200	11.10	1.70
Tantalum	14550	7.95	3.85

Table 3.1: Estimates of the critical point parameters for some metals [7].

Cold stopping

In cold stopping processes, the *stopping power* S is defined by

$$S = -\frac{\mathrm{d}E}{\mathrm{d}x} = \frac{e^4}{4\pi\epsilon_0^2}\frac{\bar{Z_P}^2 n_e^b}{m_e v^2}\mathscr{L}, \tag{3.1}$$

where $\bar{Z_P}$ is the charge of the projectile ion (for completely ionized atoms $\bar{Z_P} = Z$, Z being the atomic number), $v = \beta c$ is the ion velocity, m_e is the electron mass and n_e^b is the number density of bound electrons. The negative sign signifies that the stopping power represents energy lost by ions during interaction with the target.

The factor $\mathscr{L}$ is the *stopping logarithm* or *stopping number* and appears after integrating the Rutherford cross section over all impact parameters b between two limiting values b_{min} and b_{max}. Classically, it is given by

$$\mathscr{L} = \ln\frac{b_{max}}{b_{min}}. \tag{3.2}$$

The distance travelled by an ion of initial energy E_0 in a medium until it is completely stopped is called *range*:

$$R\left(E_0\right) = \int_0^{E_0} S^{-1}\mathrm{d}E. \tag{3.3}$$

The energy deposition profile $S(x)$ can be calculated by integrating Eq. 3.1, if S as a function of $E(x)$ is known. The dependence $S(x)$ is called Bragg curve. $S(x)$ increases more pronouncedly as x approaches R, and it has a characteristic sharp maximum called the Bragg peak. At this point the ion very quickly deposits the rest of its energy and is stopped.

For heavy ions under 1 AGeV (like the uranium beams used in this work), the charge state will change significantly during stopping, from completely ionized $\bar{Z}_P = Z$ to neutral $\bar{Z}_P \approx 0$ near the end of the range. Therefore, due to its dependence on $\bar{Z}_P^2$ seen in Eq. 3.1, S will be strongly affected by this change.

Calculating the stopping number $\mathscr{L}$ proves to be very difficult for arbitrary ion energies. Following the work in [88] the stopping number can be rewritten as

$$\mathscr{L} = \mathscr{L}_{Bethe} + \Delta\mathscr{L} \tag{3.4}$$

where

$$\mathscr{L}_{Bethe} = \ln\left(\frac{2m_e c^2\beta^2\gamma^2}{I}\right) - \beta^2 \tag{3.5}$$

is the stopping number obtained by Bethe [87] and $\Delta\mathscr{L} = \sum\delta\mathscr{L}$ is the sum of the corrections that can be made to it. The effective ionization potential I of the target material in Eq. 3.5 can be calculated theoretically, though usually it is regarded as an empirical parameter.

Three corrections can be made to the Bethe stopping number: the Bloch, Mott and Ahlen corrections [90]:

$$\Delta\mathscr{L} = \delta\mathscr{L}_{Bloch} + \delta\mathscr{L}_{Mott} + \delta\mathscr{L}_{Ahlen} \tag{3.6}$$

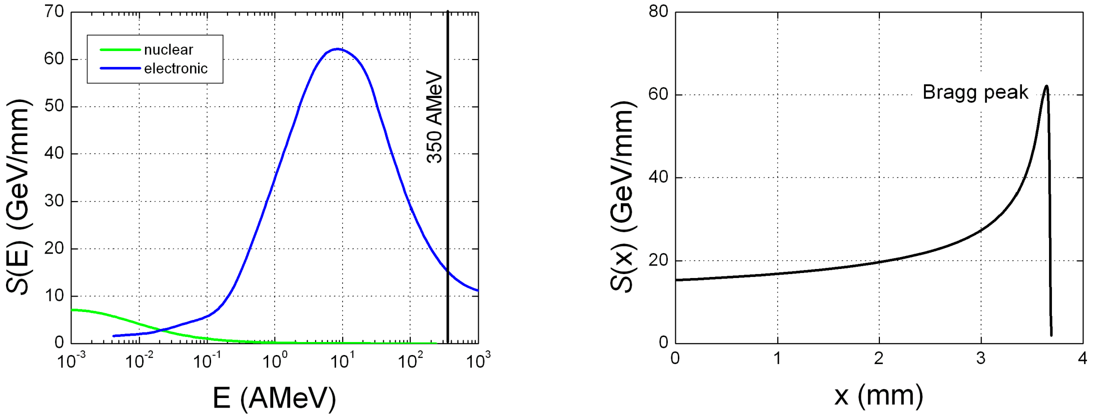

(a) **(b)**

Figure 3.2: Stopping power S for ^{238}U in lead, shown in (a) as function of initial ion energy per nucleon E, and (b) as function of penetration depth x for a given initial ion energy of 350 AMeV.

The Lindhard–Sørensen correction ($\delta\mathscr{L}_{LS}$) developed in [88] replaces the three above. Further corrections can be made, but as shown in [89], they can be neglected for heavy ions in the energy range 100-1000 AMeV.

Another important factor in calculating the stopping power S, besides the stopping number $\mathscr{L}$, is the charge state of the projectile $\bar{Z}$.

An ion penetrating through matter can go through different processes (electron capture, ionization, excitation or decay) before reaching a dynamical charge state equilibrium. The mean charge state changes with the change in ion velocity due to energy loss. To describe these processes, all the cross sections for the relevant electron configurations of the projectile are required.

An approximation which does not depend on the target material and works well for heavy projectiles in the 100-1000 AMeV range is given in [52] as

$$\bar{Z} = Z\left[1 - \exp\left(-\frac{0.95v}{Z^{2/3}v_0}\right)\right], \tag{3.7}$$

with $Z^{2/3}v_0$ being the orbital velocity of electrons in the projectile ions. An example of stopping power calculations performed with the SRIM code [53] for lead is given in Figure 3.2a, for a ^{238}U beam. The energy loss $S(x)$ shown in Figure 3.2b is calculated by numerical integration from this data, for an initial ion energy of 350 AMeV. The Bragg peak is clearly visible on the $S(x)$ curve, marking the maximum penetration depth.

Heating by intense heavy ion beams

In the previous section the physical processes occurring during the slowing down of heavy ion beams in cold or ionized targets have been discussed. It was shown that when heavy ions penetrate through matter, they lose their energy mainly due to the interactions with target electrons and the charge state of the projectiles changes as well. In all the previous discussions it was implicitly assumed that there is no influence of the incident beam on the target. However, the energy that the beam ions lose resides in the target. In the case of an intense beam focused to a small spot on a target, the amount of energy deposited by the beam in the target volume can modify matter properties of the irradiated samples significantly. Macroscopic portions of the target material can be heated to high (10^3 - 10^5 K) temperatures, generating a high energy density (HED) state. Matter in this state can have solid and super-solid densities and pressures in the range of megabars. The physical properties of the target change dramatically: thermophysical and hydrodynamical effects such as phase transitions, propagation of shock and rarefaction waves become important.

The heating of matter caused by an intense heavy ion beam can be characterized by the specific deposited energy $\mathscr{E}$. This quantity gives the amount of energy deposited by the beam per unit mass of the target material, expressing the capability of a heavy ion beam to heat matter. The specific deposited energy can be estimated using the following formula:

$$\mathscr{E} = \frac{N}{\pi r_b^2} \frac{S(E)}{\rho}, [\mathscr{E}] = \text{kJ/g} \tag{3.8}$$

where N is the number of ions in the beam, r_b is the beam spot radius and $S(E)$ is the stopping power of the material with density ρ to the ions of energy E. This formula gives an exact value of the specific energy deposition only for the case of instantaneous heating and a uniform transverse intensity distribution of the beam. In other cases, $\mathscr{E} = \mathscr{E}(x, t)$ and Eq. 3.8 should be used only for rough estimations.

Since the stopping power is roughly proportional to the target density, $S \propto \rho$, the specific deposited energy depends only weakly on the target density. Therefore, $\mathscr{E}$ is determined mainly by the properties of the ion beam, $\mathscr{E} \propto N$, $\mathscr{E} \propto 1/r_b^2$.

$\mathscr{E}$ amounts to the internal (thermal) energy of the target material induced by the beam heating. Thus, together with density, it defines the thermodynamical state of matter. Given the equation of state (EOS) of the target material, other thermodynamic quantities (such as temperature and pressure) can be obtained. For example, for a specific energy of 1 kJ/g deposited in a target at solid density, temperatures of about 0.6 eV, 1.17 eV and 0.1 eV are induced in lead, aluminium and neon targets, respectively.

Matter under such extreme conditions will be used in the experiments described in this chapter to generate the near-critical states relevant to this work.

3.2 GSI accelerator facilities and the HHT experimental area

In this section a general view of the accelerator facility at the GSI Helmholtzzentrum für Schwerionenforschung GmbH in Darmstadt will be given, as well as a detailed description of the HHT experimental area. GSI provides unique accelerator facilities. Already at the end of the 1980s experiments on volume target heating were performed using the MAXILAC-RFQ accelerator, with Kr^+ beams, in 45 AkeV millisecond pulses [58].

Plasmas generated in solid density materials became available with the setting into operation of the heavy ion synchrotron SIS-18 in 1990 and the High Temperature (HHT) experimental area in 1991. In 1994, a Ne^{10+}, 300 AMeV beam of $2 \cdot 10^{10}$, about 1 μs long was used to perform experiments with rare-gas solids, though at a very low specific energy deposition of only 0.06 kJ/g [59].

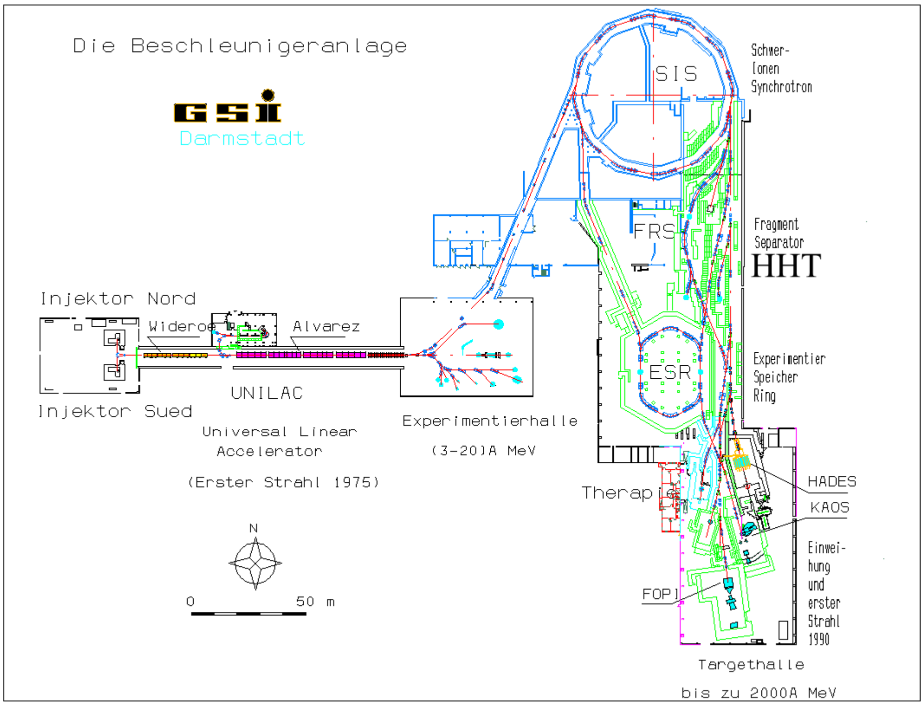

Figure 3.3: Layout of the GSI accelerator facilities [57].

To increase the specific energy deposition in the target, the ion beam must be focused to a smaller spot. A plasma lens was developed and introduced in 1994 as the final focusing system, reducing the diameter of the spot to ≈800 μm (FWHM) and increasing the deposited energy [60]. By 1996 an intensity around $2 \cdot 10^{10}$ was reached with $^{40}\text{Ar}^{18+}$ ions allowing for hydrodynamic experiments in metallic targets [61], with deposited energies around 1 kJ/g in the Bragg-peak region for solid lead targets. This was achieved by depositing the ion beam energy as fast as possible, before the target material expands too much, using a reduced pulse length from 1 μs to 250 ns. The pulse length can be further reduced to around 100 ns using the fast bunch rotation technique [67].

3.2.1 SIS-18

The heavy ion synchrotron SIS-18 is capable of delivering highly energetic ion beams, with particle intensities around 10^9 - 10^{10} and energies up to a couple of AGeV.

SIS-18 represents the final accelerating stage before HHT, with a circumference of approximately 217 meters, and maximum magnetic rigidity $B\rho$ of 18 Tm.

To increase the beam intensity in the ring without increasing the UNILAC intensity, a multiturn injection scheme is used: the ions are injected over several revolution periods and fill the entire transverse phase space acceptance of the ring.

Also, an electron cooler is in operation since 1998 at SIS-18, with which the ion beam intensity can be further increased by several times. The ion beam interacts in the electron cooler with a coaxial low-emittance electron beam, between succesive multiturn UNILAC injections. Thus the transverse emittance of the ion beam is reduced, increasing its phase space density. As a result, the total number of particles that can be accumulated in the ring is increased.

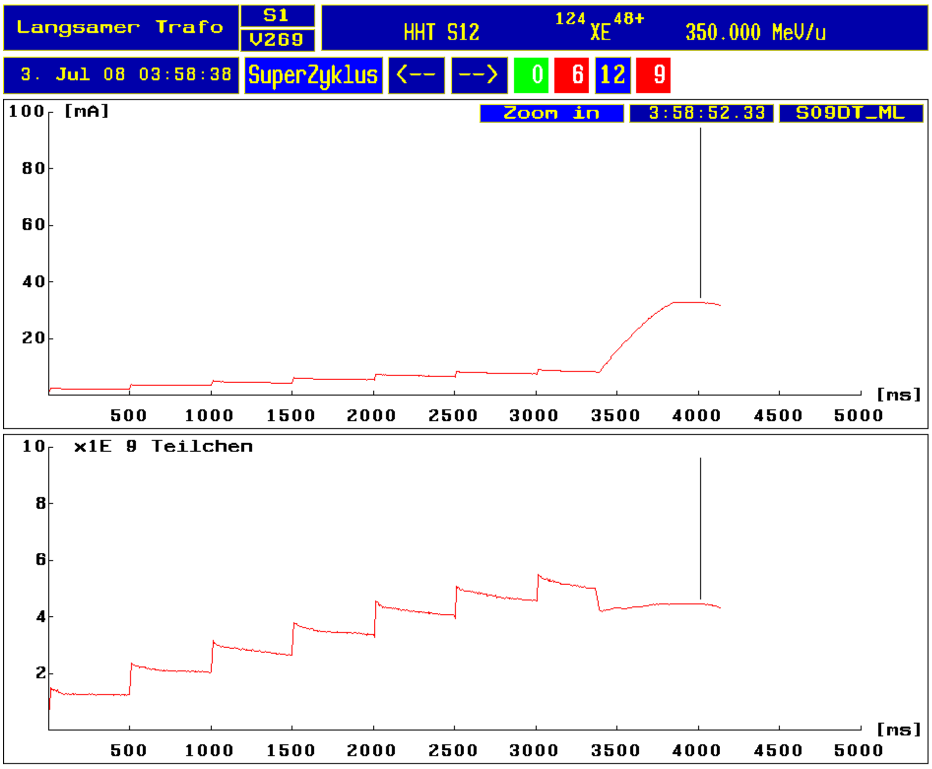

Figure 3.4: Evolution of beam intensity (upper half of the image) and ion count (lower half of the image) in SIS-18.[75].

Using 5-15 injections for $^{238}U^{73}$ ions, an intensity of about $4{\cdot}10^9$ particles/pulse has been reached at HHT.

Injection

The heavy-ion beams are produced and pre-accelerated at the ion source area (Figure 3.3). Several types of ion sources can be used: PIG (PennInG ion source), MEVVA (MEtal Vapour Vacuum Arc), MUCIS (MUlti Cusp Ion Source). Then the ions are accelerated by the 120 m long UNILAC (UNIversal Linear ACcelerator), with a final energy between 1.4 AMeV and 20 AMeV. This accelerator has multiple sections.

The High Current Injector (HSI) was commissioned in 1999. First, the ion beam is accelerated from 2.2 keV/u up to 120 keV/u in the 9.35 m long IH-RFQ operating at 36 MHz. Afterwards the ions go through the IH-DTL made of two separate tanks (9.1 m and 10.3 m long). The beam energy after IH1 is 0.743 MeV/u, and after IH2 it reaches the full HSI energy of 1.4 MeV/u[62]. The HSI-beam is further stripped and one charge state is selected (e.g. 28+ for uranium beams) to be injected into the Alvarez accelerator [63]. The Alvarez accelerates the high intensity HSI beam without any significant particle loss. The typical injection energy into the SIS-18 is 11.4 AMeV. In the transfer line to the SIS-18 a foil stripper and another charge state separator system is used to further select the desired ions (e.g. 73+ for Uranium beams). The entire acceptance of the SIS-18 accelerator can be used by varying the beam position during injection. Thus the phase-space can be fully filled. This procedure is called Multi-Turn injection, because the ions are injected during several revolutions of the beam within SIS-18. This procedure was further improved to a Multi-Multi-Turn injection after the installation of the electron cooler. It

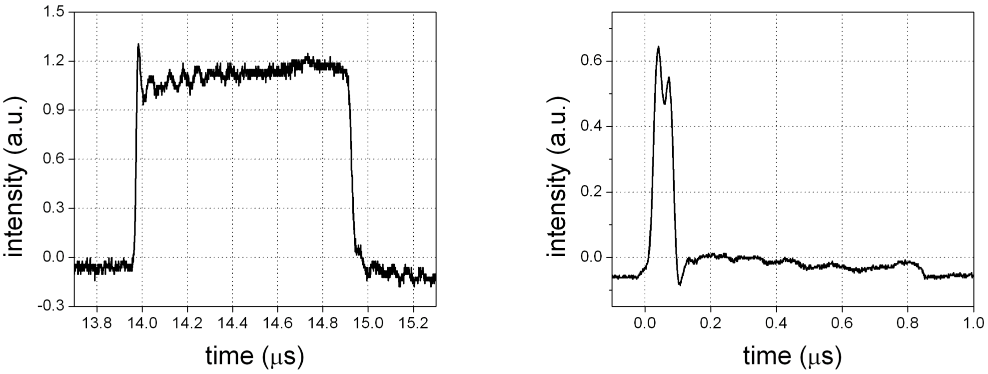

(a) Coasting beam profile.

(b) Compressed beam profile.

Figure 3.5: Ion beam temporal profiles. The area under the curves is proportional to the total ion count.

is illustrated in Figure 3.4 for a $^{124}\mathrm{Xe}^{48}$ beam, during a seven turn injection. The beam intensity as measured by a current transformer is shown in the first image, while in the second one the estimated ion count is plotted. After seven injections and ≈3.5 s the ring is completely filled and the acceleration begins. It can be seen that some of the ions are lost due to an effect described in [64, 65] during the RF capture of the beam. As the ions are accelerated, the current increases, while the ion count remains constant.

Acceleration

The acceleration phase begins as soon as the phase space is completely filled (approximately at time mark 3.5 s in Fig. 3.4).

The acceleration is performed at the fourth harmonics ($h = 4$) of the ion beam revolution's frequency for the accelerating RF-field. Therefore, during the acceleration phase, the beam consists of four particle bunches. The magnetic field and the frequency of the accelerating voltage must be increased synchronously with the ion energy. To be able to accelerate ions injected from the UNILAC at $\beta \approx 0.15$ to $\beta = 0.6..0.9$, the cavity frequency must be variable in the range $\nu = 0.8..5.4 MHz$.

To recombine (rebunch) them, the accelerating voltage is decreased to a minimum to redistribute the beam uniformly over the circumference of the ring, forming a so called 'coasting beam' that can be seen in Figure 3.5a. Afterwards the accelerating voltage (at the first harmonics $h = 1$ this time) is increased to recompress the coasting beam into a single bunch.

Extraction

The final step consists in extracting the beam out of the SIS-18 after the acceleration phase and the beam rebunching have taken place, using a fast extraction mode in the beam is bent from its orbit in SIS-18 by a fast magnetic kicker (<20 ns) to an extraction channel in the septum magnet. In the present work, after extraction, the ions are guided to the HHT beam-line.

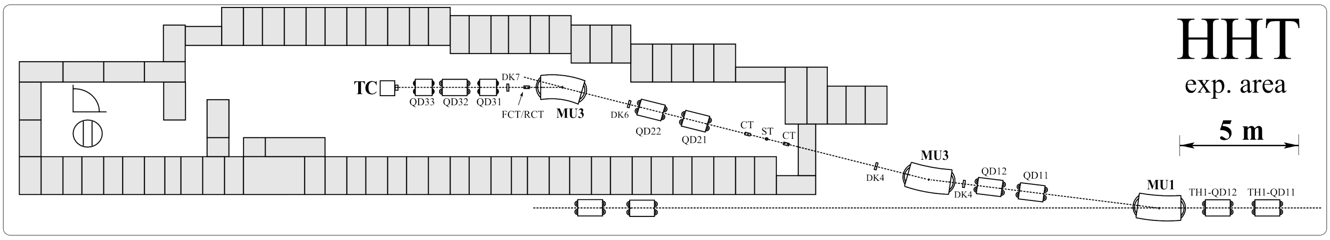

Figure 3.6: Layout of the HHT experimental area [57].

Compression

By quickly raising the accelerating voltage to the first harmonics, the coasting beam can be compressed into a single bunch of approximately 250 ns. With the fast bunch rotation technique described in [67], better compression can be achieved, down to pulses shorter than 100 ns, as shown in Figure 3.5b.

3.2.2 HHT experimental area

The heavy-ion beams are extracted from the synchrotron and they reach the HHT experimental area through the beam-line shown in Figure 3.6. Its total length (from SIS-18 to target chamber) is around 75 m, with the last 30 m used only for the HHT area. The beam-line inside the HHT cave is composed of three bending dipole magnets, two quadrupole doublets and one quadrupole triplet, with various beam diagnostic and vacuum control instruments built in.

3.2.3 Data acquisition system

Recently, a new automated system for data acquisition and hardware control (DAQ/HC) was commissioned at the HHT area. This system streamlined the previously manual process by providing access to every device in a unified manner. Each device's nature, properties, function and hardware connection are wrapped into abstract classes written in Python, following a unified programming interface called Device API. Each instrument has a class derived from the Device Driver written for it. This class is instantiated as an object that runs locally on the computer that is directly connected to the instrument (via RS-232, GPIB, USB, Ethernet or any other kind of connection) and exposes a fixed set of methods defined through the Device API.

The architecture of the DAQ-HC is shown in Figure 3.7, and the main components are described below.

A Device Server initializes the Device Driver object (remotely or locally) and acts as in intermediary between clients and the Device Drivers. The Device Server communicates with the Device Driver object through a transport layer (API-TL), which can for example be a Remote Procedure Call (RPC) library.

The actual data acquisition and hardware controlling during a beam-time is performed by a specialized GUI client named APEMAN ('Acquisition for Physics Experiments'). It prepares and arms all the instruments for actual data acquisition, sends beam requests to the accelerator control system, retrieves data recorded during the shot and stores everything in a database located on a data file server. The database can be afterwards accessed using SQL.

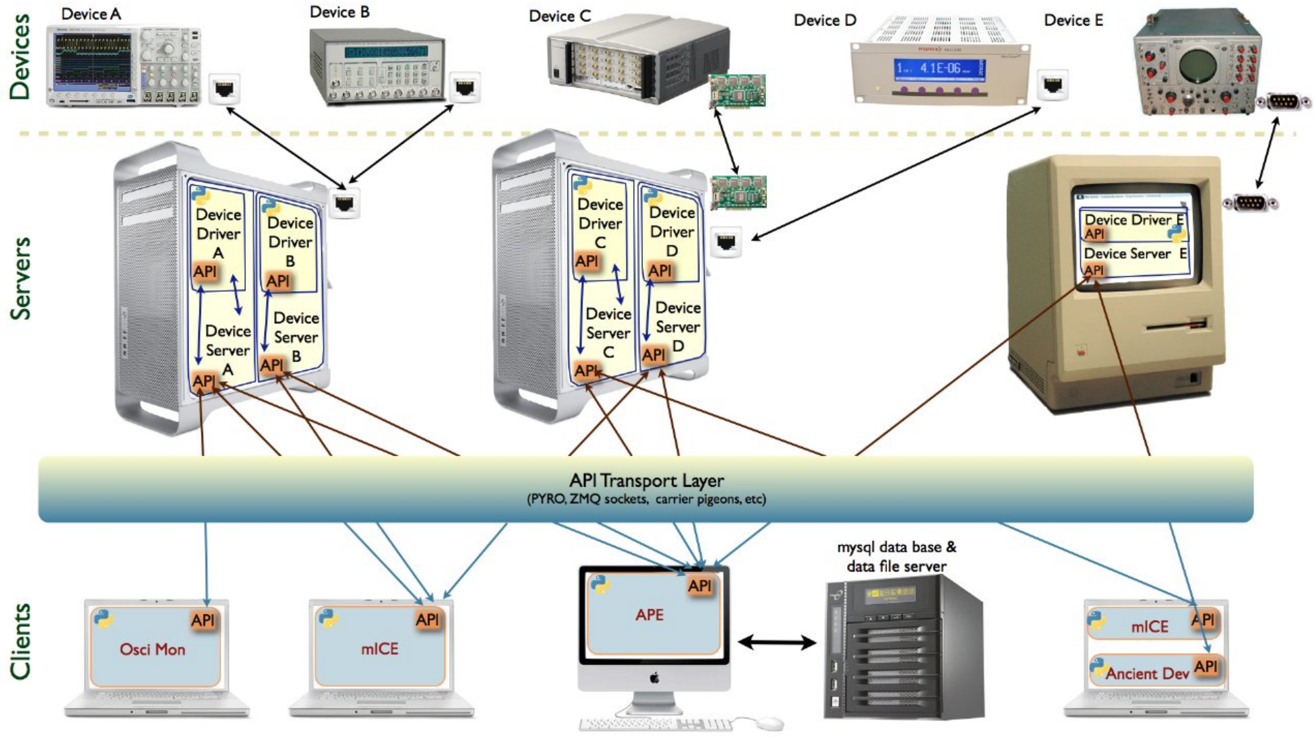

Figure 3.7: HHT DAQ/HC schematics.

The slow control and device monitoring part is realized by a number of specialized GUI or command line clients. In particular, the mICE ('devIce Control for Experiments') GUI client is used to set and inspect the attributes of any set of devices. The DAQ/HC system, being written only in Python, is highly portable on different operating systems: Microsoft Windows, Linux/UNIX or OS X. The only platform dependent parts could be some Device Drivers, if the low-level device access libraries are provided by the device manufacturer for a particular platform only (such is the case with the streak cameras at HHT, which run only on Microsoft Windows).

3.2.4 Target chamber and target design

The target chamber at HHT houses the target assembly, target manipulator (Figure 3.8a) and pyrometer collection optics (Figure 3.26). It can be filled with different gases (helium, argon) or brought to a vacuum of 10^{-5} mbar.

3.3 Experiment description

The general target geometry is a modification of the one described in the HIHEX concept [7, 26]. An elliptically focused ion beam is used to heat the material, by homogeneous energy deposition in the region before the Bragg peak. As can be seen in Figure 3.2b, for a few millimetres after target penetration, the stopping power curve is almost flat. Because in the original HIHEX configuration different physical parameters are measured on different sides of the foil, it is highly susceptible to errors due to horizontal beam-target misalignment. This misalignment induces different energy deposition levels, and consequently different phase trajectories during the material expansion and impact on the windows. Therefore a single-sided planar configuration was

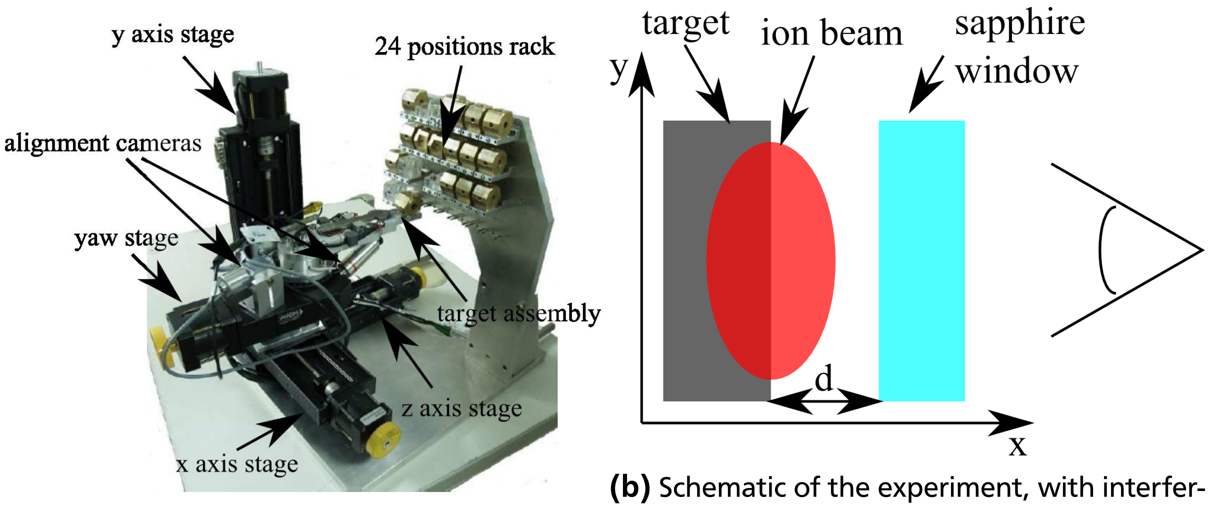

(a) 6-axis target manipulator and target assembly rack inside the vacuum chamber.

(b) Schematic of the experiment, with interferometer and pyrometer looking from the right.

Figure 3.8: Target manipulator and target configuration for the ion beam driven experiment.

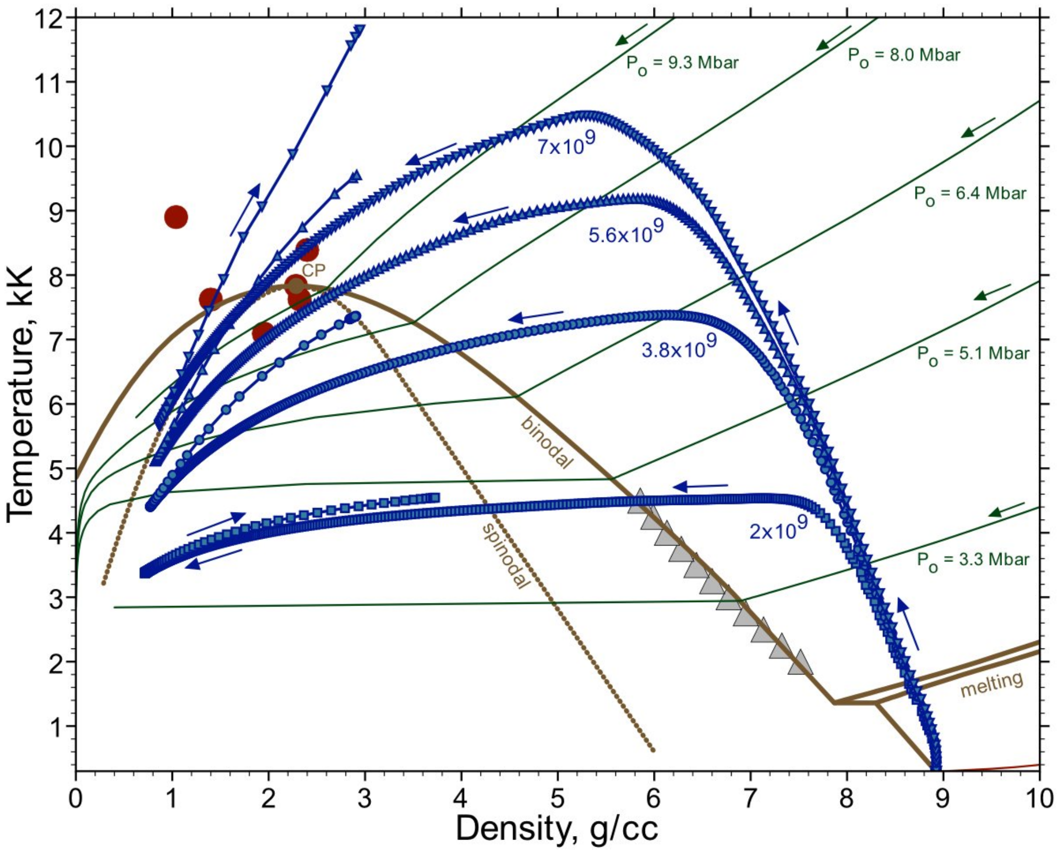

Figure 3.9: T – ρ phase diagram of copper and phase trajectories for the heavy ion experiment [76].

developed and commissioned in the experiments described in this chapter.

Instead of the thin foil used in previous experiments, a thick piece of material is placed with its polished side parallel to the beam axis. The ion beam is focused to an elliptic spot near the sample's surface, either inside or outside. A ≈1 mm thick transparent sapphire (Al_2O_3) window is placed parallel to the target surface, at a distance of ≈1 mm, as shown in the schematics in Figure 3.8b. The window side facing away from the target has a narrow-band reflective dielectric coating applied, centred on the interferometer's diagnostic laser's wavelength (532 nm). The fast multi-channel pyrometer described in Section 3.4.5 is focused on the window side facing towards the target, in order to record the temperature of the material hitting the window.

The speed of compression and final pressure can be varied by changing the distance d between the target surface and the sapphire window.

Also, different energy deposition levels can be achieved by varying the ion beam intensity, thus exploring different regions of the phase diagram (including the near-critical states).

In order to assess the physics performance of the proposed experiment, preliminary simulations have been performed for copper using a one-dimensional hydrodynamic code and a wide-range semi-empiric EOS [77]. A beam of 350 AMeV uranium ions with an elliptic focal spot of 0.4 x 0.8 mm (FWHM), with a Gaussian distribution of intensity both in space and in time was used, of 100 ns (FWHM) duration and intensity variable from $2\cdot10^9$ to $7\cdot10^9$ ions per pulse.

The resulting phase diagram of copper in density–temperature variables is shown in Figure 3.9. The phase boundaries – boiling and melting curves – are represented by brown solid lines. Red circles represent different theoretical estimates of the critical point location, and grey triangles show the only available experimental data from resistive heating experiments with which semi-empirical EOS in this phase diagram region are obtained [76].

Green lines are the release isentropes from different shock-compressed states, with the corresponding shock pressure, and with blue smybols and lines are represented the phase trajectories that can be obtained with ion beams. By scaling the data to lead, it is clear that powerful shock waves with Po≈3 Mbar are required, while with heavy ion beams for sample heating the same region can be accessed much easier.

Following one of the blue lines for a given beam intensity, starting from the normal conditions of solid metal, the sample is being quasi-isochorically heated and then expands into the buffer gas. During the expansion, the phase trajectories are crossing the binodal (boiling curve). When the sample material is reaching the window, the phase trajectory turns back. Depending on the initial energy deposition level and the gap width, it may then either closely follow its expansion isentrope, or encounter a stronger temperature rise due to a shock-like impacting on the window. Some trajectories may therefore escape the two-phase liquid-gas region. In this manner, the whole area of interest in the phase diagram shown in Figure 3.9 can be covered in a controllable way.

3.4 Diagnostic instruments

The main diagnostic instruments used in this experiment are an imaging displacement interferometer and a fast multi-channel pyrometer, with the relevant data acquisition devices, such as image intensified cameras for ion beam and target alignment, streak cameras for recording of interferograms and fast digital signal converters.

3.4.1 Imaging displacement interferometer

An imaging Michelson interferometer such as the one described in Section 2.2.2 was used, having as diagnostic laser a continuous wave Verdi system at 532 nm and 2 W.

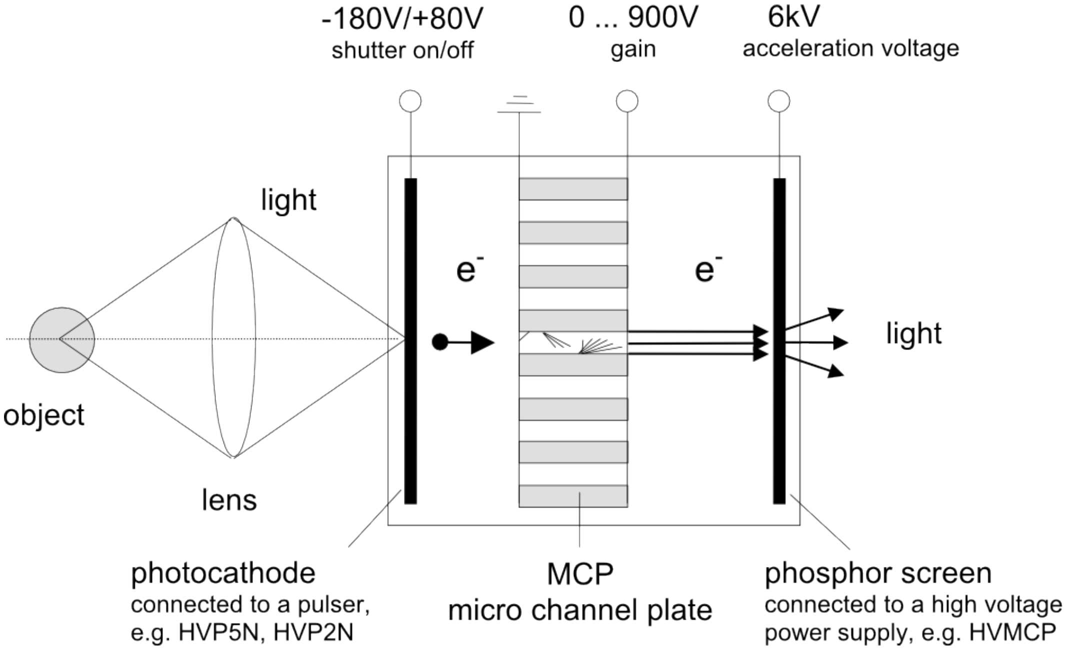

Figure 3.10: Operating principle of image intensification.

Due to using a long coherence length laser (coherence length of several meters), the arms of the interferometer do not have to be of precisely the same length. The observed target surface is imaged on the streak camera, on the beam splitter and on the fringe tuning mirror.

The optical field must be kept flat through the entire imaging system, that is why a doubly afocal set-up is used.

By having a conjugate pair of imaging planes on the beam splitter and the fringe tuning mirror, the laser beam in the reference arm is prevented from clipping the image on the beam splitter for large angles.

Specific optical schematics are given in Sections 3.5 and 3.6 describing the experimental set-ups used in the beam-times at HHT, as they underwent improvements in time.

3.4.2 Image intensified camera

Two intensified and cooled iCCD (intensified CCD) cameras were used for alignment purposes and acquiring images during shooting of the targets. The cameras permit fast shutter times, down to a few nanoseconds and a so-called 'Double Shutter' mode, in which two different pictures can be taken with a time separation of a couple μs. This is done using an 'Interline-Transfer'-CCD chip. A true 'Multiframe' mode of operations is not allowed though due to the relatively long afterglow of the phosphor screen, which would superpose on the second taken image. The 'Double Shutter' mode was used to obtain some information on the expansion of the target right after being hit by the ion beam during the commissioning of the imaging displacement interferometer in May 2010. The operating principle of these cameras is shown in Figure 3.10. Photons hit a photocathode which then emits electrons that are multiplied in a variable gain MCP multiplier. The resulting electrons are accelerated in a 6 kV accelerating electrical field and they impress a phosphor screen which is then imaged on a CCD.

In operation at HHT, the cameras are equipped with long focal distance objectives and are focused at infinity, so that a 300 mm focal length lens can be installed before the target to

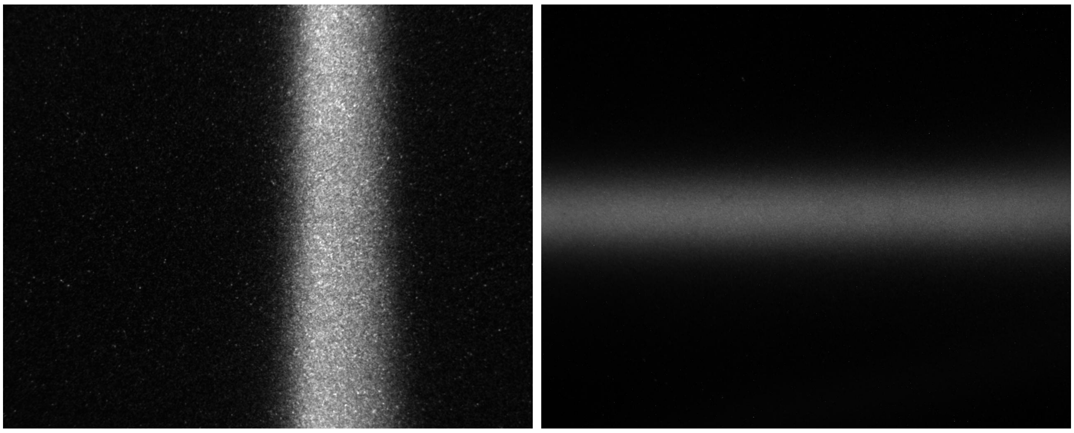

(a) view in the XZ plane **(b)** view in the YZ plane

Figure 3.11: Argon luminescence ion beam alignment with DICAM camera at an exposure time of ≈1 μs.

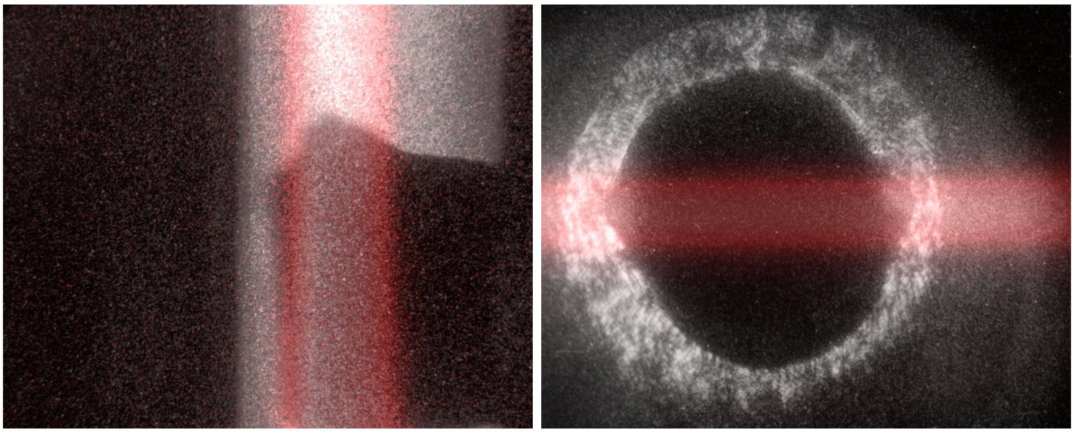

(a) view in the XZ plane **(b)** view in the YZ plane

Figure 3.12: Lead target during ion beam shot, at an exposure time of 5 ns. Beam position in both planes as obtained during argon luminescence alignment is marked with red and superposed on the images of the target.

complete the imaging system. Fields of view of a few millimetres are normally obtained, with sub-millimetre depth of field.

A usual target alignment procedure performed with these cameras is described below;

1. The cameras are mounted to look at perpendicular planes YZ and XZ.
2. Spatial calibration is done with a millimetric grid drawn on transparent plastic.
3. For the focusing and spatial alignment of the ion beam, it is repeatedly shot into the argon filled target chamber to produce fluorescence trails that are recorded with the iCCD cameras. Thus the centre and width (FWHM) of the ion beam can be estimated [79].
4. With the target manipulator, under real time camera surveillance, the target is brought in the correct position and orientation along the ion beam axis. Afterwards a reference image is saved.

Step 3 of the procuedure is represented in Figure 3.11. The ion beam position is marked in both planes and used in correctly aligning the target to the beam. The target after being brought in the correct position and orientation, as seen by the alignment DICAM cameras, is depicted in Figure 3.12 during an actual shot, with the ion beam from Figure 3.11 superposed in red.

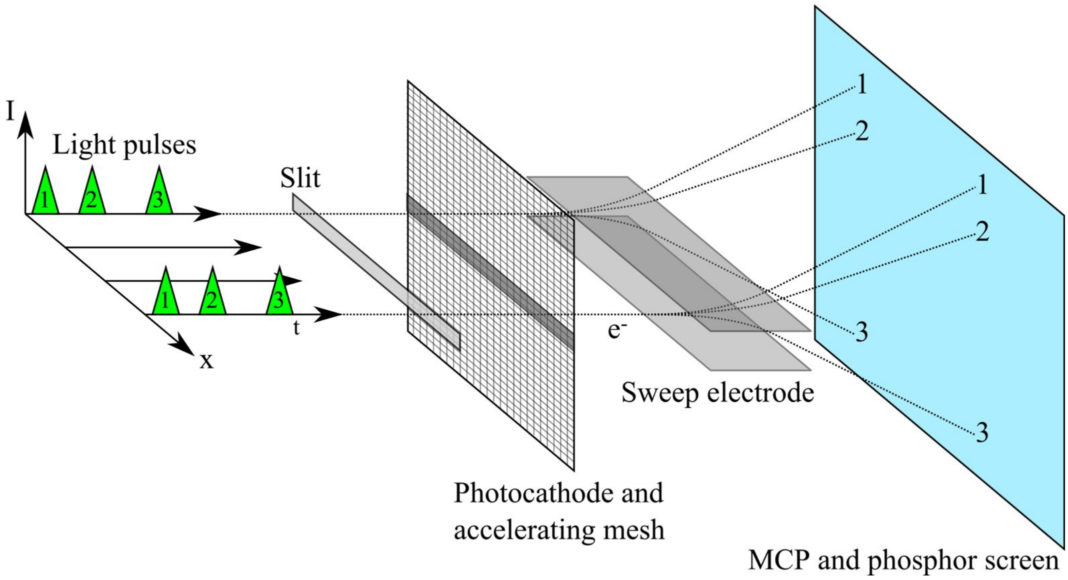

Figure 3.13: Operating principle of a streak camera.

3.4.3 Streak camera

A streak camera resembles in construction an image-intensified camera. The Focus mode allows for the alignment of the target on the camera in real time, while in Streak mode, using a variable electric field, the temporal profile of the light intensity falling on the slit is obtained. In Figure 3.13 light goes through a narrow slit and hits the photocathode behind it. The emitted electrons go through a time-varying electrical field, are scanned across an MCP, intensified and then they hit a phosphor screen. The resulting photons are recorded with a CCD. Characteristic operating parameters are the slit width, the gain and the streak time.

To achieve high temporal resolution it is necessary to use a narrow slit. In the same time, if the slit is not wide enough and the streak time is very short, the signal can get too low to be detected. Therefore a compromise between temporal resolution and signal intensity must be reached.

3.4.4 Acousto-optic modulator

An acousto-optic modulator (AOM) from ELECTRO-OPTICAL PRODUCTS CORPORATION [51] was used to inject the probe laser for short periods of time (microseconds) into the optical system, in order to protect the DICAM and streak cameras. Such a device, also called a Bragg cell, uses the acousto-optic effect to diffract an incident beam of light using sound waves (usually at radio-frequency). A piezoelectric transducer is attached to a material such as glass and it is driven to vibrate by an oscillating electric signal, which creates sound waves in the glass. The index of refraction is changed in a periodic manner by the spatial pressure variation. Incoming light scatters (Brillouin scattering) off the resulting periodic index modulation and interference occurs in a similar way to what is observed in Bragg diffraction (as shown in Figure 3.14).

The intensity of the diffracted beam can be optimized by varying the incidence angle. The switching time can go as low as a couple of microseconds, but here a time of 10 μs was used.

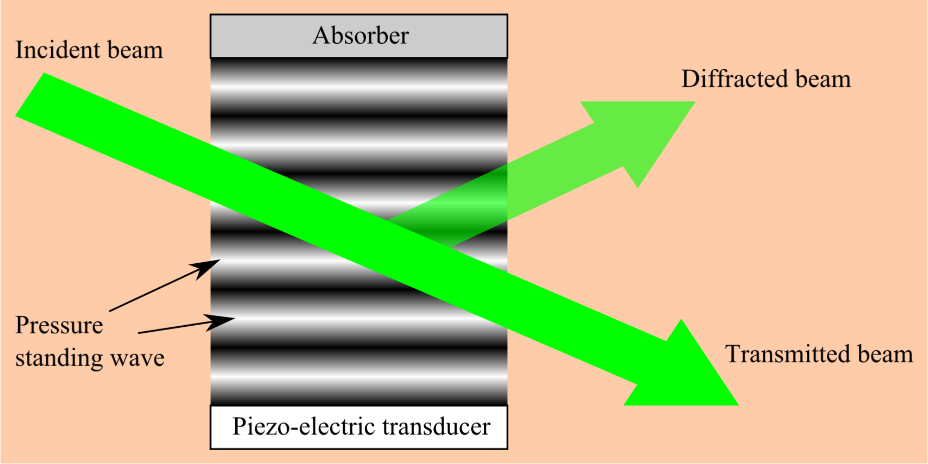

Figure 3.14: Operating principle of an acousto-optic modulator.

3.4.5 Pyrometer

Pyrometers are devices used to perform contact-free temperature measurements. They measure the intensity of the emitted electromagnetic radiation in different wavelength ranges, and then, by reconstructing the spectrum, the temperature can be estimated.

Thermal radiation

The Stefan–Boltzmann law [82, 83] states that the black-body irradiance depends only on the black body absolute temperature:

$$\frac{P}{A} = \sigma T^4, \tag{3.9}$$

where $\sigma = 5.670373 \cdot 10^{-8}$ W m^{-2} K^{-4} [80] is the Stefan-Boltzmann constant, P is the total emitted power and A is the total area of the object.
At temperatures lower than the surrounding temperature, the object absorbs more energy than it emits, while at higher temperatures the opposite happens. When the object is in thermal equilibrium with its surroundings, there is no net energy flow between them.
The spectral radiance was approximated first by the Rayleigh-Jeans law:

$$L_\lambda(T) = \frac{2ckT}{\lambda_4}; L_\nu(T) = \frac{2\nu_2 kT}{c_2}, \tag{3.10}$$

where c is the speed of light, k the Boltzmann constant, T the absolute temperature, λ the wavelength and *nu* the frequency. The Rayleigh-Jeans law describes the black-body radiation well at large wavelengths, but at lower ones leads to the 'ultraviolet catastrophe', when the radiance goes to infinity as the frequency increases.
Another approximation was given by Wien's law [84]:

$$L_\lambda(T) = \frac{C_1}{\lambda_5 \exp C_1/\lambda T} \tag{3.11}$$

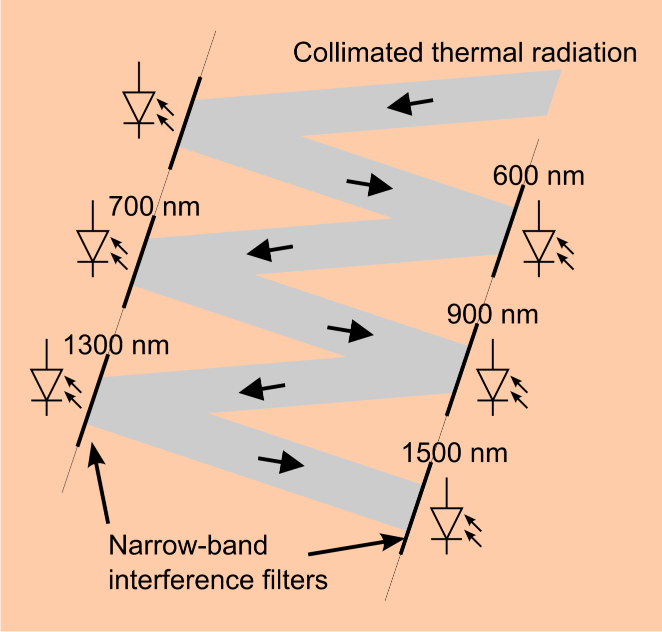

Figure 3.15: Pyrometer spectral analyser schematic set-up: light falls on a series of narrow-band transmission interference filters. Each selected wavelength range is analysed using a photodiode located behind each filter.

Finally Planck's law gave the correct description of the spectral radiance:

$$L_\lambda(T) = \frac{2h\nu^3}{c^2}\frac{1}{\exp h\nu/kT - 1}; L_\nu(T) = \frac{2hc^2}{\lambda^5}\frac{1}{\exp hc/\lambda kT - 1}. \qquad (3.12)$$

Experimental set-up

The pyrometer used at HHT was developed in [15, 39, 40]. Temperature is determined for a spot of 200 μm in diameter, by recording thermal radiation in five VIS-NIR wavelength bands: 600 nm, 700 nm, 900 nm, 1300 nm, 1500 nm (see Figure 3.15). Temperatures above 1500-2000 K can be determined in this configuration.

The emissivity coefficient $0 < \epsilon < 1$ plays an important role in the determination of temperature. For black body radiation $\epsilon = 1$, but for real bodies it must be experimentally obtained. To this purpose, a 4 W laser diode emitting at 809 nm was used to measure the back reflection from the target surface. Further improvements to the pyrometric system are described in [75]. The light collection optics are situated in the target chamber, while the spectral analyzer and the data acquisition system are located in the HHT measurement room, thermal radiation being conveyed through quartz optical fibres.

3.5 Commissioning of the imaging displacement interferometer

During preliminary experiments, tests were performed with the interferometer system decoupled from the pyrometer. The pressure range measurable with the imaging displacement interferometer was estimated.

Uranium ion beams of 1 μs duration at 350 AMeV and $\approx 2 \cdot 10^9$particles/pulse were used.

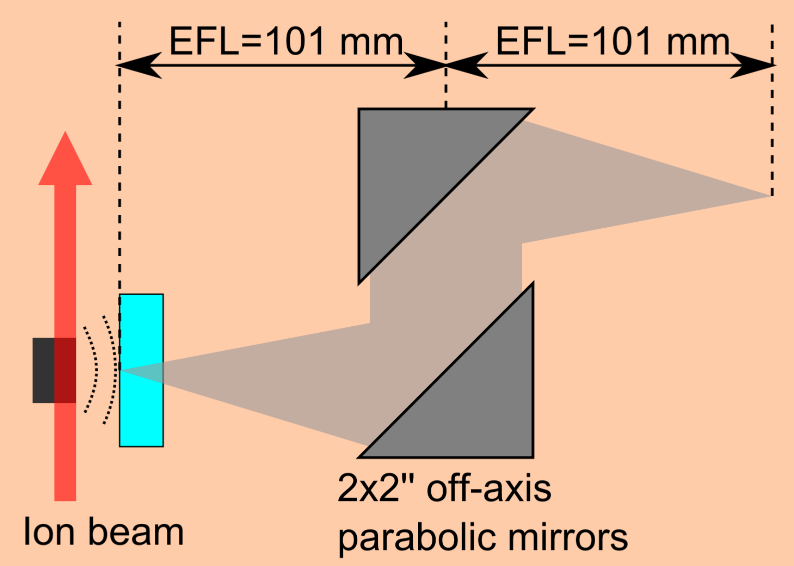

Figure 3.16: Pyrometer light collection schematic set-up: two 90° off-axis parabolic mirrors with an effective focal length (EFL) of 101 mm focus the emitted light on a 200 μm optic fiber.

3.5.1 Experimental set-up

The modified Michelson interferometer described in Section 3.4.1 was developed and commissioned in these experiments, with the optical schematics shown in Figure 3.17. The interferometer was mounted on a movable table as seen in Figure 3.18. A removable mirror in front of the streak camera (Figure 3.19c) allows, when inserted in the optical path, for the fringes to be visualized on an alignment camera. By remotely tilting the alignment mirror in the reference arm of the interferometer, the fringe spacing and orientation can be tuned.

Also, by having it shift the image to the alignment camera, and not to the streak camera, better precision in imaging the same location on the sapphire window is achieved, without having to consider the repeatability in mirror repositioning. On the alignment camera only a precision around 1 mm is needed to keep the region of interest within the field of view, as the CCD chip size is around 1 cm, precision which was easily obtained (actually it was clearly under 100 μm). A vertical line on the target surface was imaged on the slit of the streak camera. Because of the relatively high errors in target manufacturing which lead to a total loss of fringes on the alignment camera, a second alignment camera was mounted looking at the target chamber window through which the diagnostic laser was injected. On this window the residual reflection of the laser beam was visible, for both incoming and outgoing beams, and by tilting the robotic arm around the y and z axes in large steps the beam could be made roughly collinear. Fine tuning of the fringes was performed using the same robotic arm, in fine steps, until around 10 vertical fringes were visible on the fringe alignment display. Time calibration of the streak camera was performed using a short pulse LED (1 μs), as depicted in Figure 3.20. The spatial calibration of the streak camera was done with a millimetre grid drawn on a transparent plastic foil, as can be seen in Figure 3.21a. Due to the short focal length of the lenses in the imaging system from Figure 3.19b (75 mm, 100 mm), the final resolution was relatively poor, the marks on the millimetre grid being barely visible.

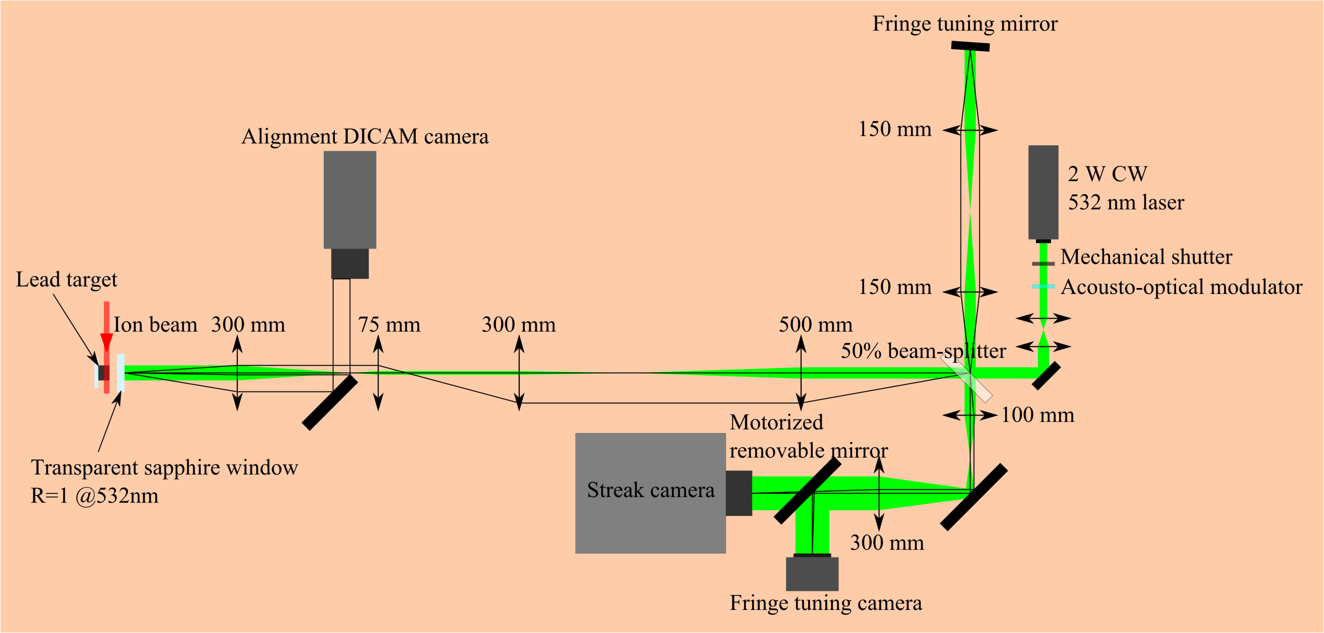

Figure 3.17: Schematic set-up for the imaging displacement interferometer during the commissioning phase.

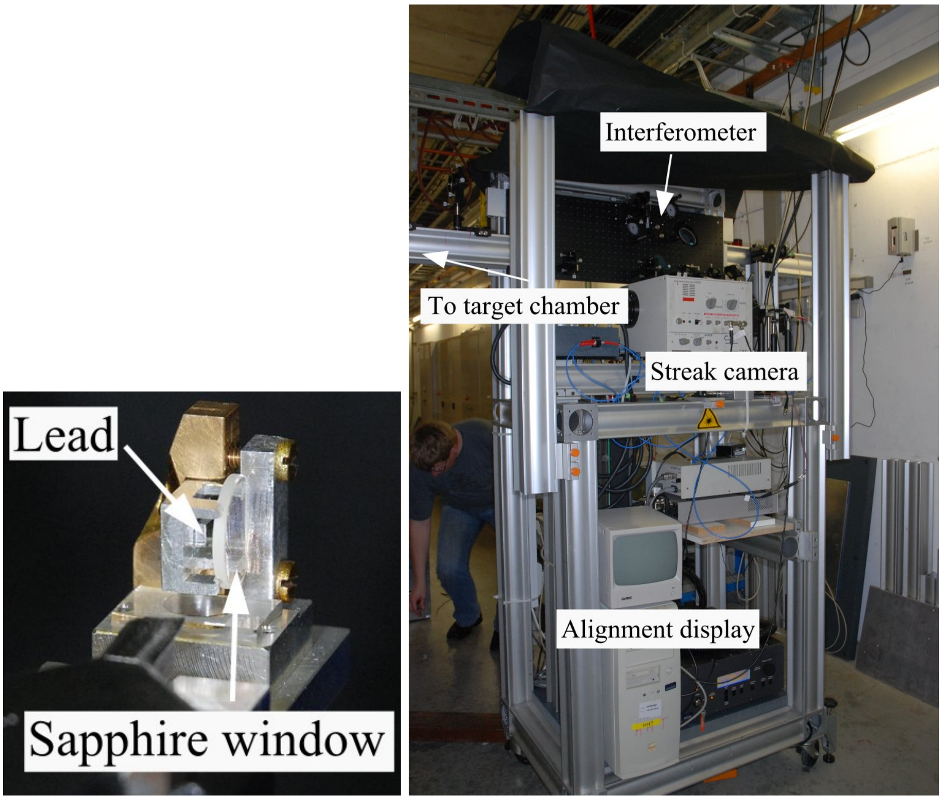

Figure 3.18: Commissioning set-up with the target configuration on the left and the moveable interferometer set-up on the right.

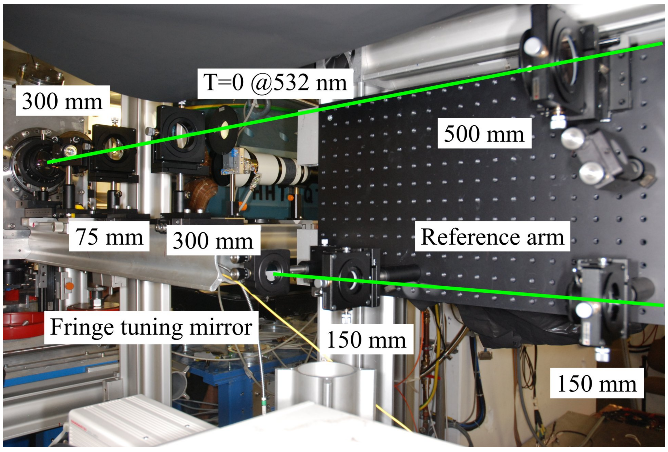

(a) Imaging system to target chamber.

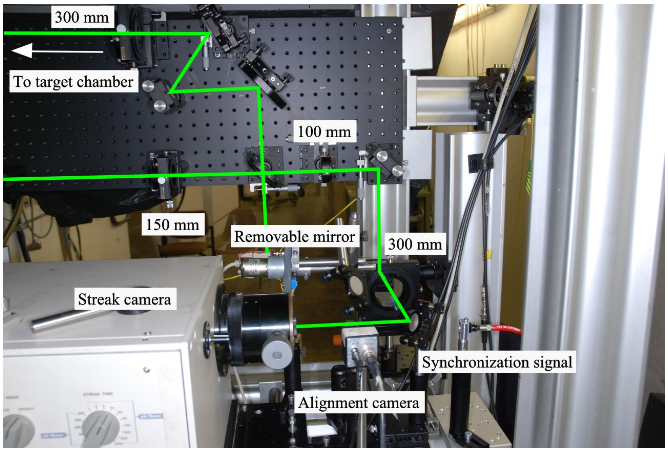

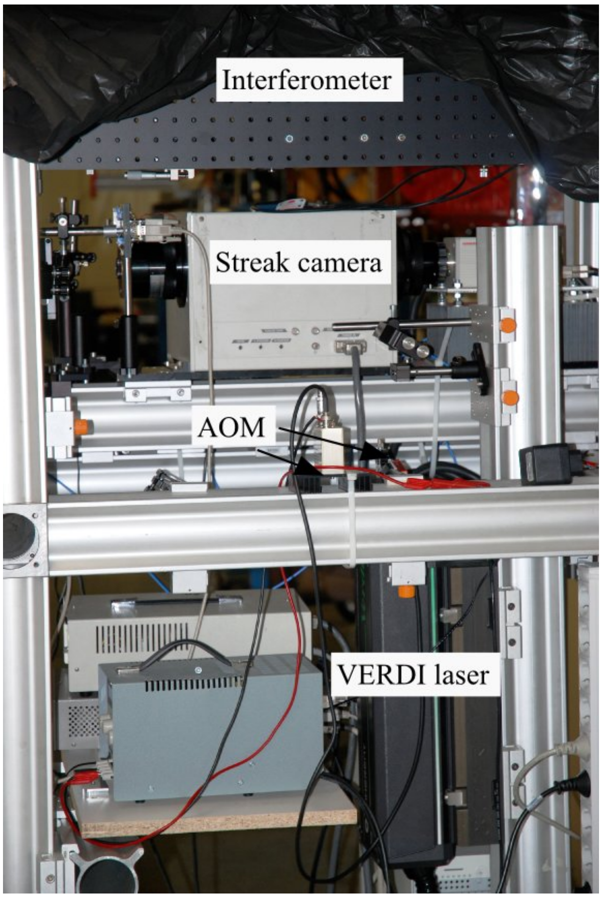

(b) Imaging system to streak camera.

(c) Laser injection.

Figure 3.19: Imaging displacement interferometer optics during commissioning.

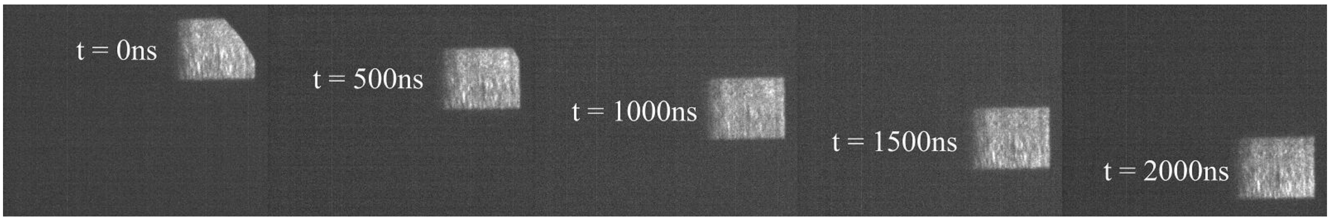

Figure 3.20: Time calibration of streak camera during commissioning of the imaging displacement interferometer.

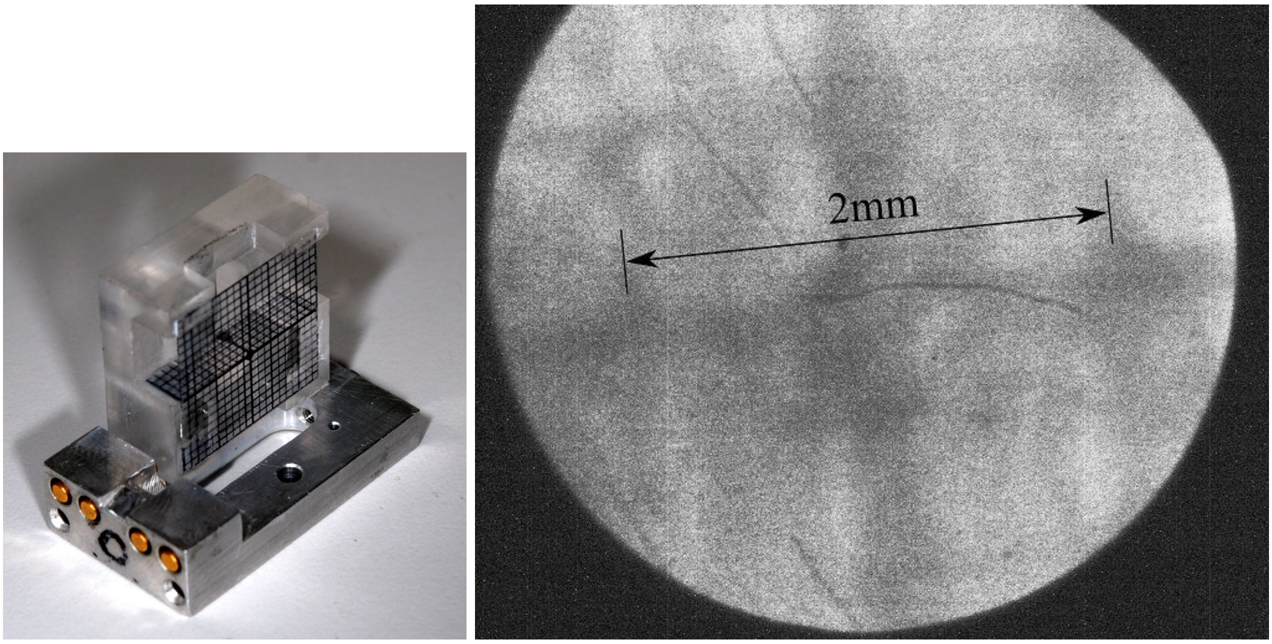

(a) Millimetre grid target. **(b)** Image of millimetre grid on streak camera.

Figure 3.21: Spatial calibration of streak camera during commissioning of the imaging displacement interferometer.

3.5.2 Interferogram analysis and results

Spatial loss of illumination across the field of view was clearly visible on the interferograms, most probably because of clipping in the optical path. As shown in Figure 3.22a, on the left side of the picture the signal intensity decreases to unusable levels. Only the better illuminated right side of the interferograms could be used. The Fourier transform based method described in Section 2.2.4, was implemented to analyse the interferograms.

Pressure is calculated from velocity by considering the fact that sapphire at kbar pressures is still in the elastic regime, in which pressure p and particle velocity U_P can be related through the following equation

$$p = U_P \cdot Z, \tag{3.13}$$

given the acoustic impedance $Z = 44.3 \cdot 10^6$ kg/m^2 of sapphire [81].

Particle velocity is given by

$$U_P = \frac{U_S}{2}, \tag{3.14}$$

where U_S is the recorded surface velocity. The period of oscillations on the velocity and pressure profiles (Figure 3.22c) is 188 ns, corresponding to the time required by sound waves in sapphire to travel back and forth between the front and rear window surfaces which was calculated to be 180 ns from literature data on the speed of sound in sapphire crystals of 10.7 km/s [92] and the measured thickness of the sapphire window of 963 μm.

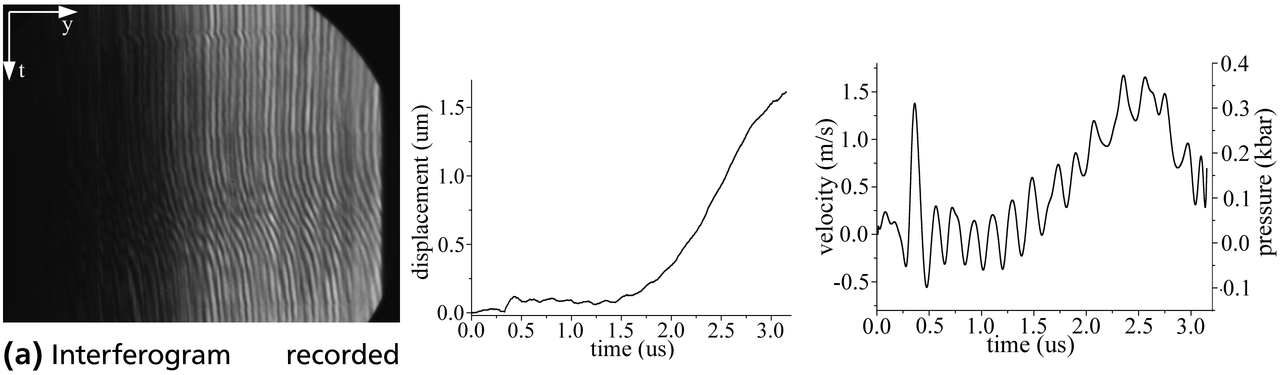

(a) Interferogram recorded with the streak camera.
(b) Displacement profile.
(c) Velocity and pressure profiles.

Figure 3.22: Results obtained during commissioning of the displacement interferometer.

3.6 Experiments with simultaneous pressure and temperature measurement

An improved version of the interferometer commissioned in the previous beam-time was developed and commissioned during this beam-time to permit the simultaneous recording of pressure and temperature profiles. The intensity of the ion beam was almost doubled.

3.6.1 Interferometer light injection and collection optics

To perform simultaneous measurements of pressure and temperature, the pyrometer and interferometer must look at the same side of the target. Due to the poor optical quality of the parabolic mirrors on the pyrometer head, they cannot be used as light collection system for the interferometer. Therefore, a specially designed achromatic system formed of two lenses was simulated in Zemax to see if the chromatic aberration can be reduced sufficiently.
Zemax is a widely-used optical design and analysis program developed by Radiant Zemax, LLC of Redmond, Washington, USA. It can perform standard sequential ray tracing through optical elements, non-sequential ray tracing for analysis of stray light, and physical optics beam propagation. It includes an extensive library of stock lenses from a variety of manufacturers. Zemax has a powerful suite of optimization tools that can be used to optimize a lens design by automatically adjusting parameters to maximize performance and reduce aberrations.
An imaging system was considered, formed of two identical lenses optimized for best RMS focus across the 600-1500 nm wavelength range. Each lens was considered to be a triplet made of N-SF6, N-SK2 and LF5, with thickness and radii of curvature given in Figure 3.23. Three incident optical fields are represented, at various angles of incidence. For each triplet, an RMS spot diameter around 100 μm was the best result, with a dependence on wavelength characteristic of an apochromat (Figure 3.24). The final imaging system is represented in Figure 3.25, with an RMS spot diameter of 200 μm. Different wavelengths are represented in different colours, compared to the field representation in the previous two figures. The RMS spot size of $\approx$100 μm does not allow precise measurements over the 200 μm spot imaged on the fibre, therefore a different system had to be implemented.
A 10 mm diameter sapphire window, coated on one side to reflect 532 nm, was used at 45° to inject and collect the interferometer laser beam. The spectral width of the coating was below the centre of the first filter in the pyrometer at 600 nm.

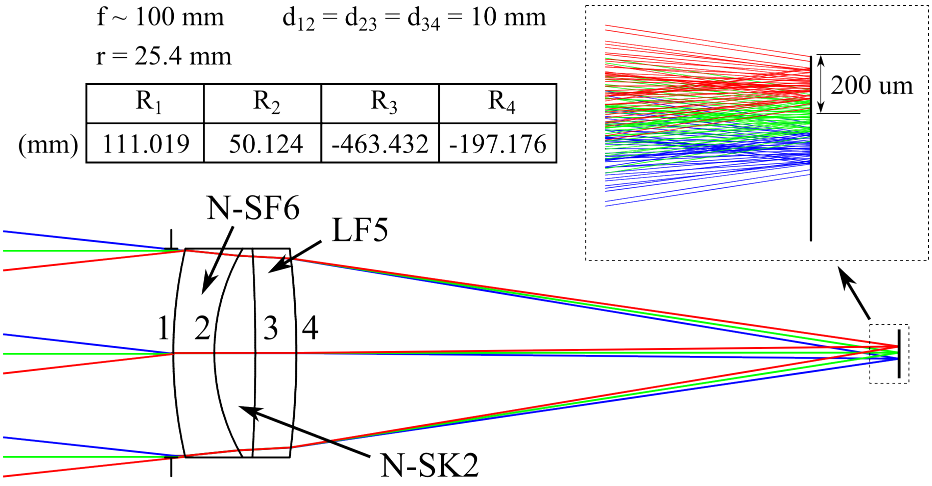

f ~ 100 mm $d_{12} = d_{23} = d_{34} = 10$ mm

r = 25.4 mm

	R_1	R_2	R_3	R_4
(mm)	111.019	50.124	-463.432	-197.176

Figure 3.23: ZEMAX simulation of optimized achromatic triplet system for 600-1500 nm range.

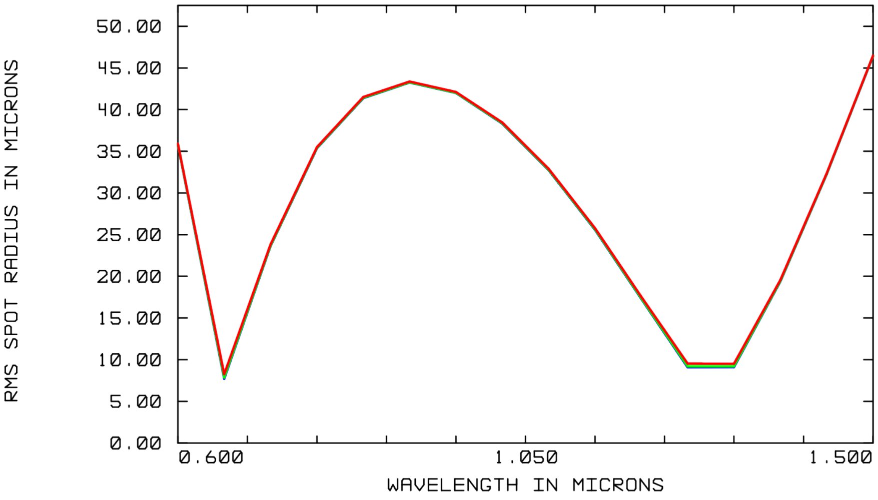

Figure 3.24: ZEMAX simulation of RMS spot size as function of for the optimized achromatic triplet system.

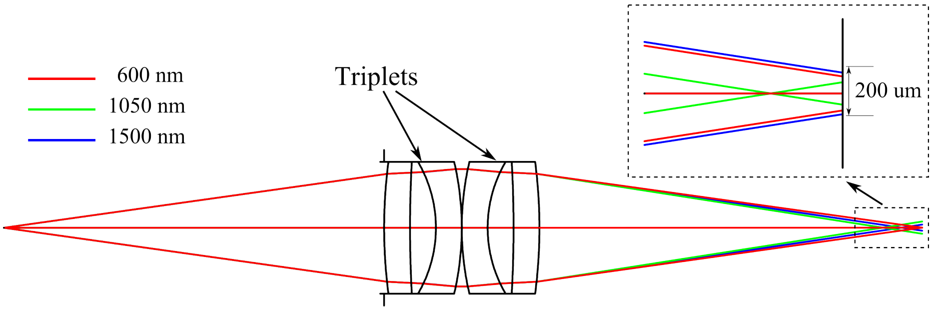

Figure 3.25: ZEMAX simulation of optimized imaging system.

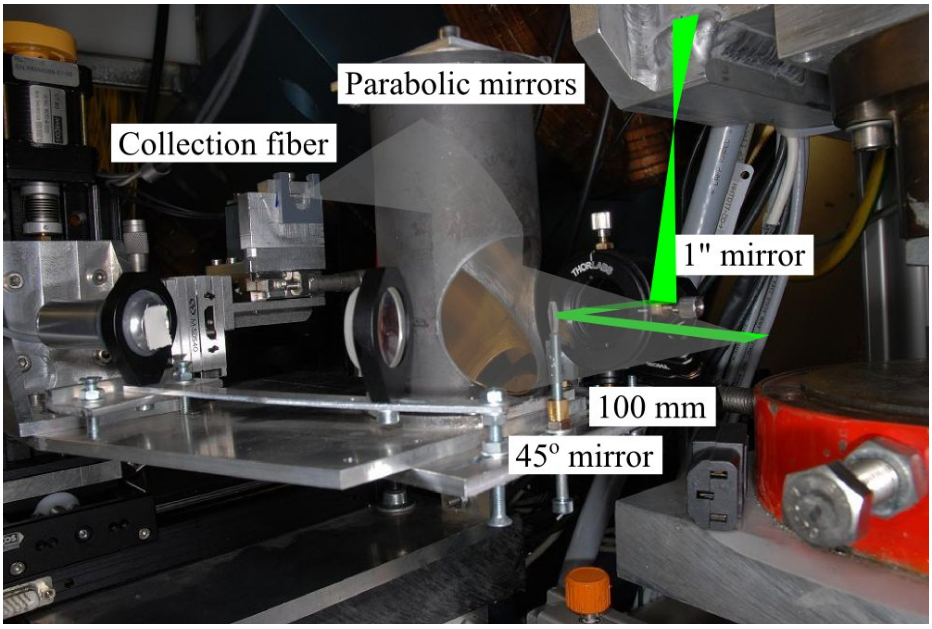

Figure 3.26: Imaging displacement interferometer optics on the pyrometer.

3.6.2 Experimental set-up

The previously commissioned displacement interferometer described in Section 3.5.1 was improved, mounting the light collection optics for the interferometer on the pyrometer head inside the target chamber (Figure 3.26). Also, instead of the short focal length lenses which degraded the image resolution, longer focal length lenses were used. Thus a resolution better than 50 μm was achieved.

The imaging system and interferometer are represented in Figure 3.27. Compared to the previous imaging set-up from Figure 3.17 in which the target chamber window was traversed by a parallel laser beam, such a window is now positioned between the last two imaging lenses, thus being traversed by a non-collimated beam. This configuration generates some astigmatic aberration, which resulted in a slight deviation of the final fringes from a perfectly straight shape. For a density of more than 20 fringes per screen though, the deviation is too small to be observed, and could be safely ignored. The target holder depicted in Figure 3.28 consists of a metallic frame in which two transparent sapphire windows are fixed. This frame is mounted on the robot arm and thus can be easily aligned into the right position.

The lead sample is glued on one of the windows and can be visualized through it with a DICAM camera (Figure 3.11b). Clipping can occur in the target arm due to the small aperture ($10mm$) of the 45° mirror in front of the collecting mirrors of the pyrometer. The lead sample's surface must be precisely aligned parallel to the back surface of the coated sapphire window in order to avoid large robot correction angles ($>1°$) that would lead to clipping. Time calibration of the streak camera was performed using a Nd:YAG MiniLase laser, with a pulse length of 7ns, as can be seen in Figure 3.30. The image of the target on the beam splitter is rotated by roughly 45 °, therefore the group of four mirrors shown in Figure 3.31a was used to rotate the image back into the correct orientation. The spatial calibration of the streak camera was done with the same millimetre grid from Figure 3.21a drawn on transparent plastic, as can be seen in Figure 3.31b.

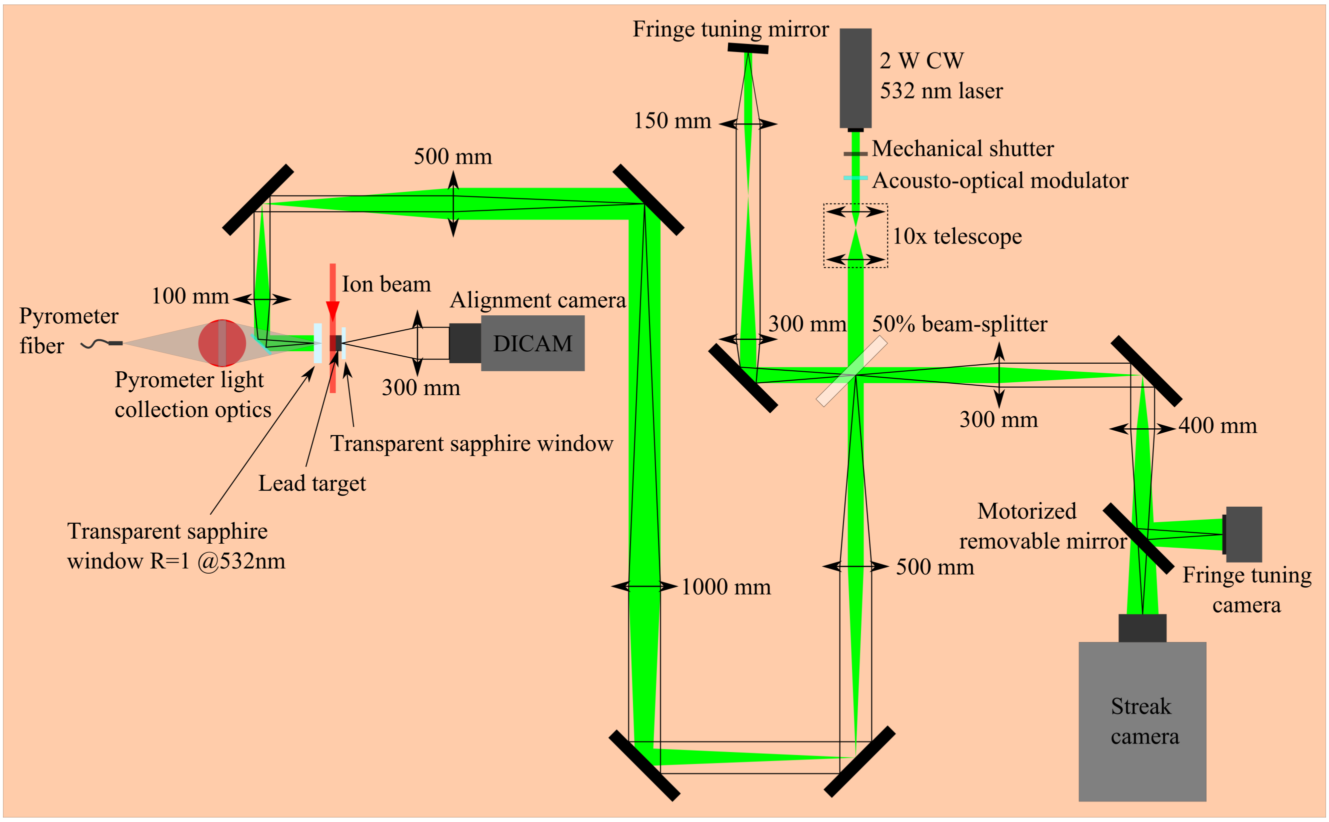

Figure 3.27: Schematic set-up of the simultaneous temperature and pressure acquisition system.

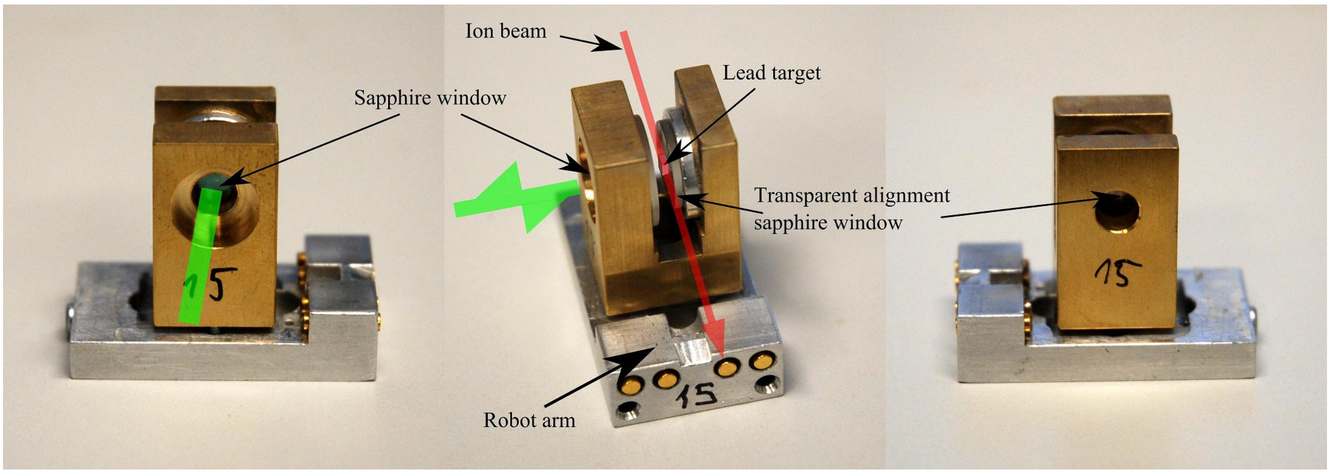

Figure 3.28: Lead target holder for simultaneous temperature and pressure acquisition. On the left image is depicted the side of the holder as seen by the interferometer and pyrometer optics, in the middle the lead target being hit by the ion beam, and on the right the side of the holder as seen by the DICAM alignment camera in the YZ plane.

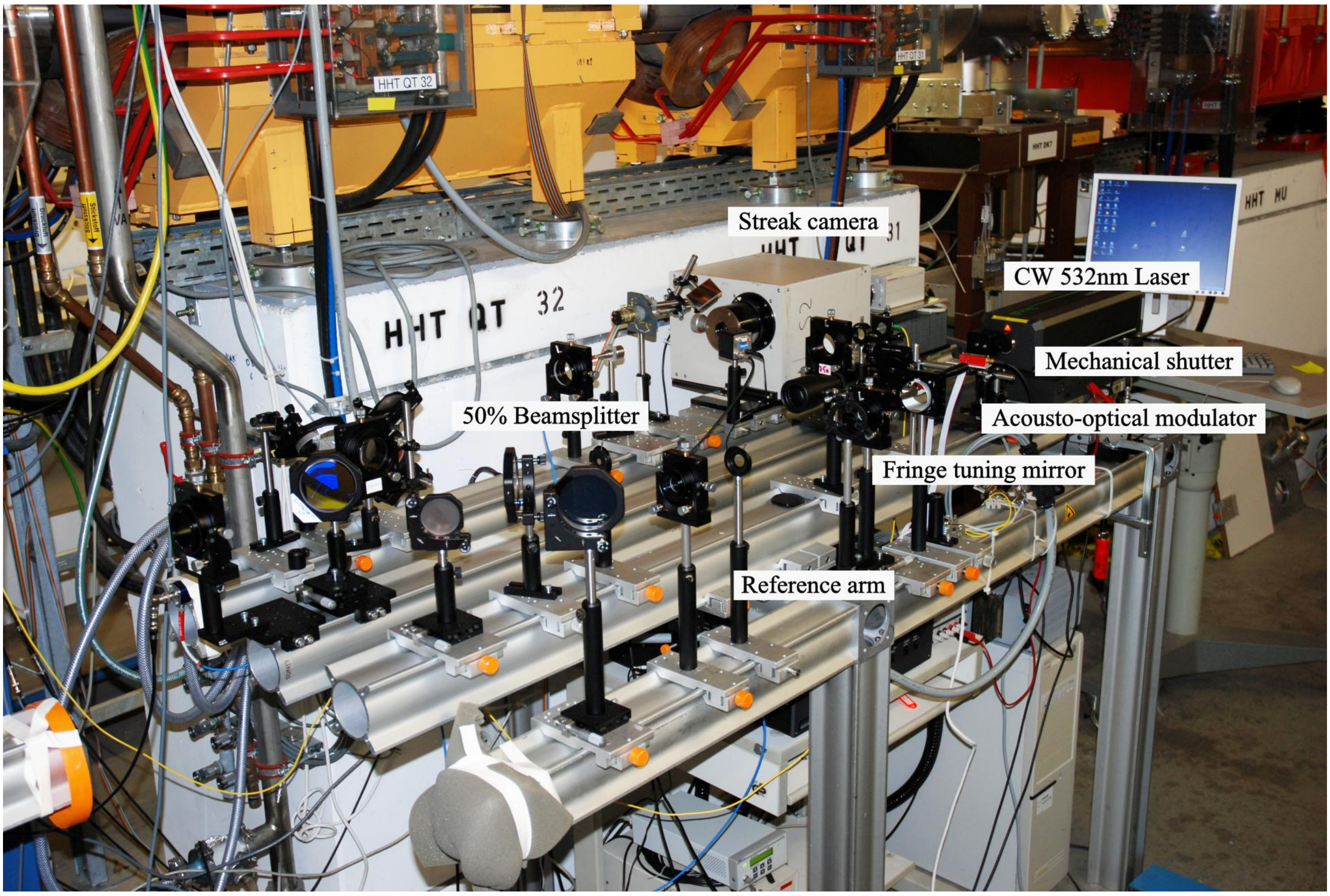

Figure 3.29: Displacement interferometer set-up during simultaneous pressure and temperature acquisition experiments.

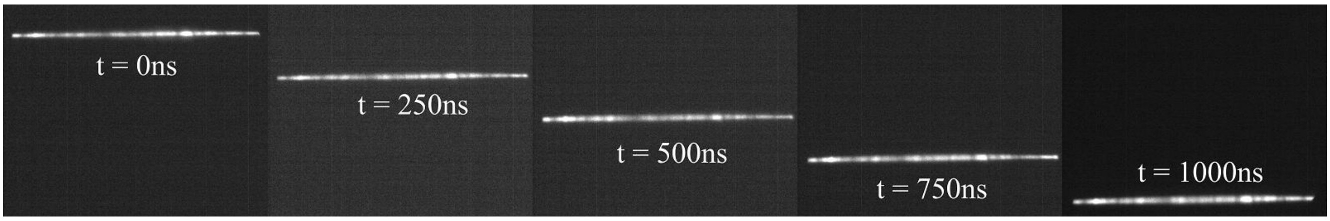

Figure 3.30: Time calibration of streak camera during simultaneous pressure and temperature acquisition experiments.

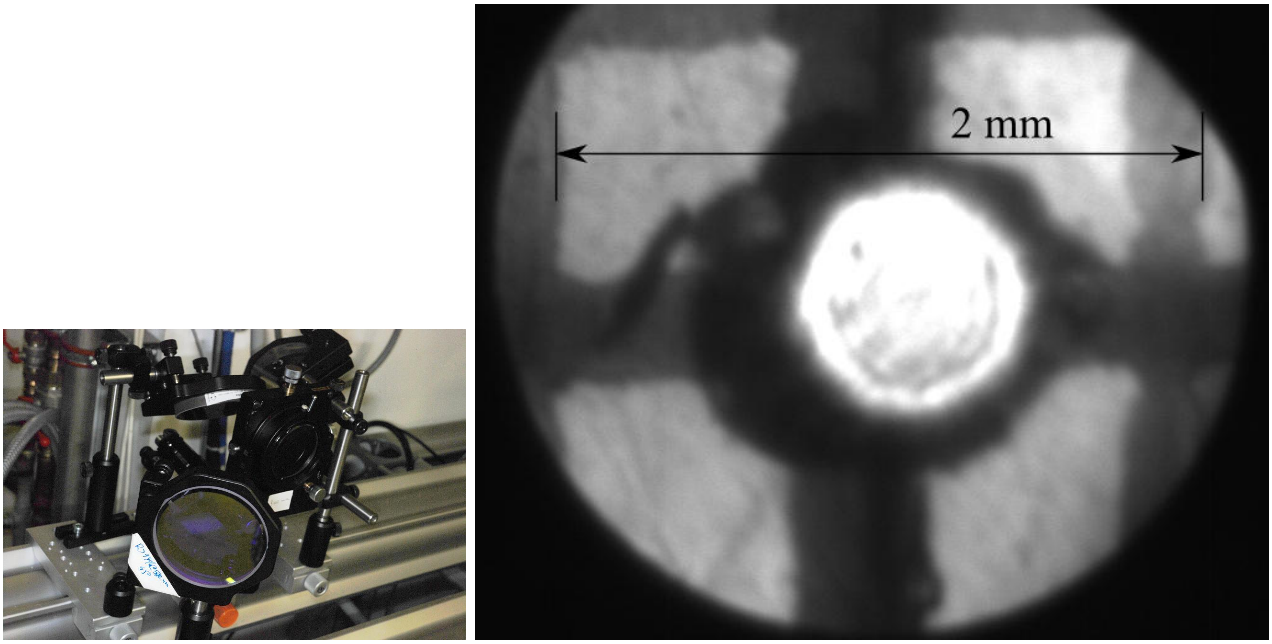

(a) (b)

Figure 3.31: Image rotation set-up shown in (a) and spatial calibration of streak camera with millimetre grid in (b), showing a clearly improved spatial resolution, during simultaneous acquisition of temperature and pressure experiments.

3.6.3 Interferogram analysis and results

The interferograms were traced manually by skeletonizing fringes along intensity minima. B-spline interpolation along the spatial coordinate (that is for each row in the streaked pictures) was performed, and then the phase was unwrapped using a simple algorithm which iterated through the rows and added an integer multiple of 2π to each of them until the difference between adjacent rows was reduced under 2π. the time derivative of the resulting phase map was calculated and converted to a velocity history. Pressure was calculated from surface velocity using the same procedure described in Section 3.5.2.

During the heating phase, the sample melts and starts to evaporate at the free surface, while a boiling wave travels towards the interior of the metal target. During expansion of the lead vapour, its temperature decreases rapidly, until liquid droplets appear.

When the expanding lead consisting of a mixture of vapour and liquid metal droplets impacts on the sapphire window, it is compressed and further heated (see Figure 3.33, after t ≈ 400 ns). According to the EOS model [8], weak (quasi-isentropic) shock compression will transform the material into pure vapour state and the droplets shall disappear. On the other hand, a certain time is needed for the phase transition, which is dependent on the dimension of the droplets. Using a high enough heating rate, the liquid droplets can be overheated up to the spinodal temperatures.

The time $\Delta t \approx 100$ ns of droplet evaporation to a pure vapour state is the duration of the

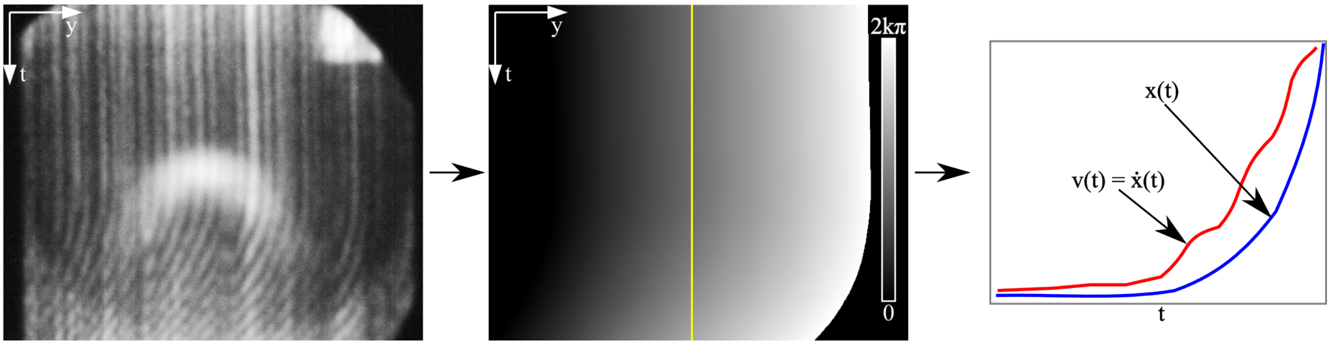

Figure 3.32: Displacement and velocity temporal profile determination: the unwrapped phase-map obtained from the interferogram on the left is shown in the middle, colour-coded with black for zero optical phase difference and white for the maximum value of the phase given by the total number of fringes; on the right is shown the derived displacement and velocity profile in a point on the surface.

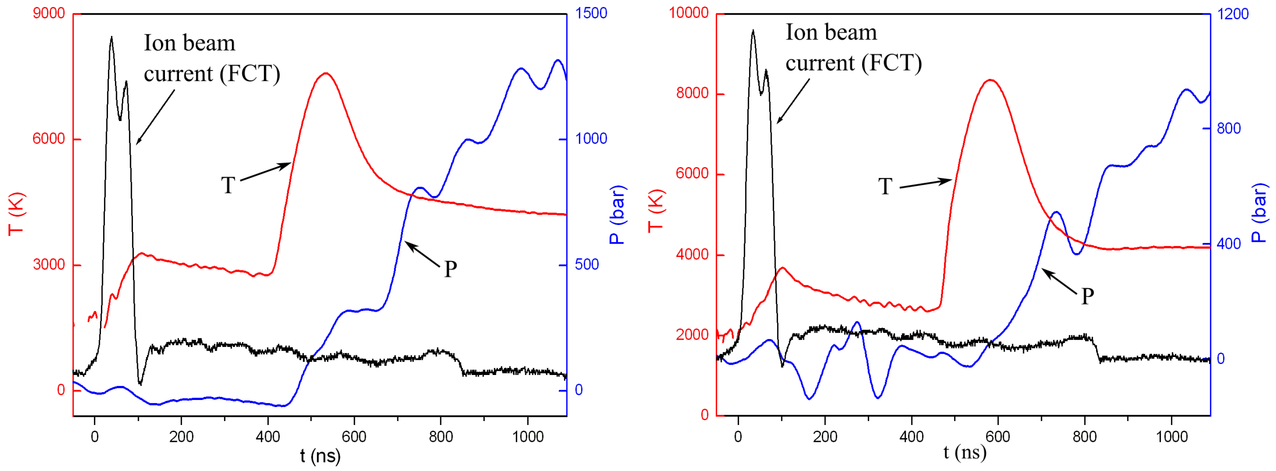

(a) Shot 654, $2.85 \cdot 10^9$ particles/pulse, gap between lead and sapphire window of 740 μm.

(b) Shot 667, $3.18 \cdot 10^9$ particles/pulse, gap between lead and sapphire window of 929 μm.

Figure 3.33: Pressure and temperature profiles obtained with the imaging displacement interferometer and the pyrometer for lead targets heated by uranium ion beams.

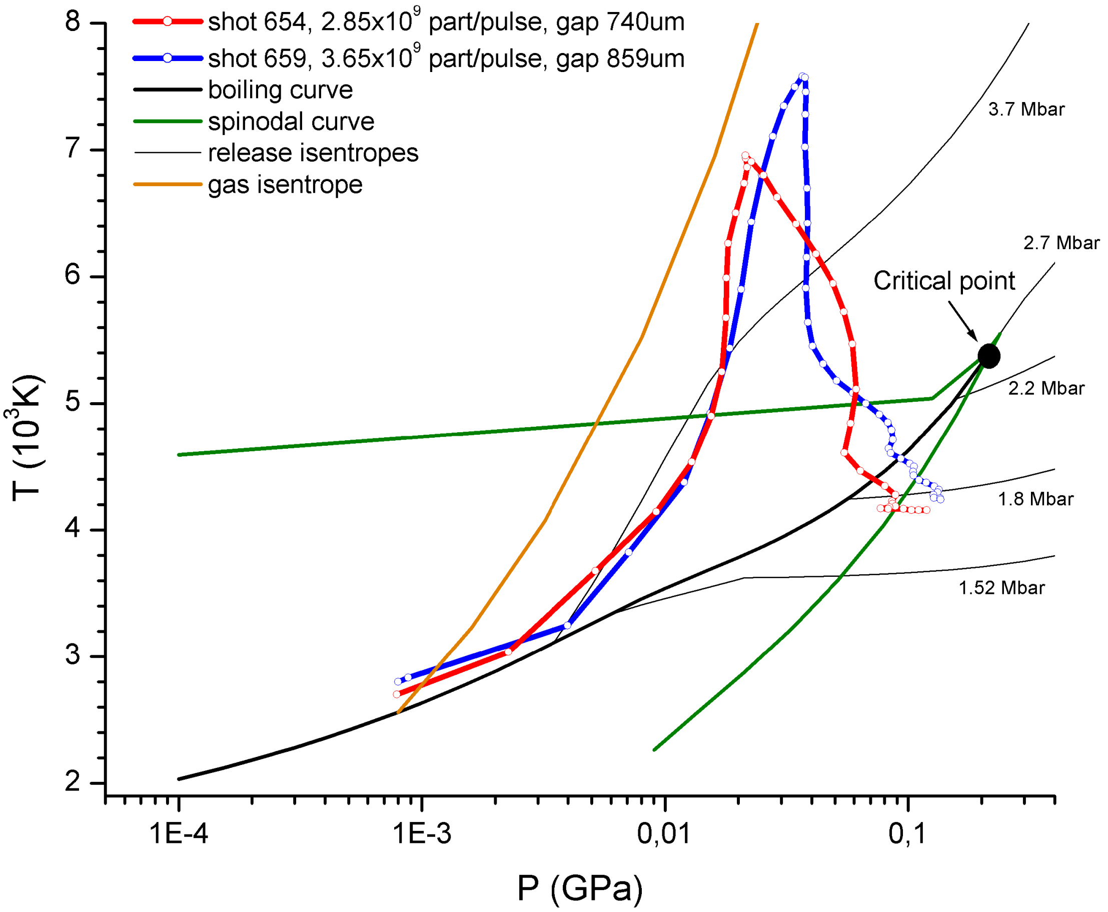

Figure 3.34: T-P phase diagram of near critical states of lead generated with heavy-ion beams: release isentropes from various multi-Mbar pressures end in the boiling curve; the path followed by lead in two heavy-ion experiments is shown in red and blue, as it starts from a point on the boiling curve, approximately follows an isentrope until it intersects the spinodal curve, afterwards kinematic effects govern the dynamics of the superheated material, to finally reach an area near the boiling curve or the 1.8 Mbar release isentrope [93].

rising slope in Figure 3.33 beginning at ≈450 ns up to maximum temperature. In isothermic conditions it can be linked to the size of the droplets using the following equation

$$\Delta t = \frac{\rho_l R_P^2}{2 m_a D N_s}, \tag{3.15}$$

where $rho_l \approx 5$ g/cm^3 is the density of liquid, R_P the droplet radius, $m_a = 208/6.023 \cdot 10^{23}$ g the mass of an lead atom, $D = 5$ cm/s^2 the diffusion coefficient and $N_s = 2.43 \cdot 10^{19}$ cm^{-3} the density of atoms in the saturated vapour [93]. N_s is calculated from the ideal lead gas isentrope from Figure 3.34 starting on the boiling curve at the same pressure as compressed lead on the sapphire window. Finally, the droplet radius R_P is found to be 0.41 μm.
The measurements were proven to be reproducible, with stable results from shot to shot.

4 Laser driven planar isentropic compression of iron

In the work presented in this chapter a laser-driven shockless method of compression is employed in the study of iron at high pressure and density, but relatively low temperature. This technique produces continuous information along the compression isentrope, compared to a single point on a Hugoniot that is obtained in a shock wave experiment.

Isentropic ramp compression methods involve applying a variable load on the target, which can be done in several ways: temporally shaped magnetic pulses [94], reservoir expansion [21], high explosives [95] and temporally shaped laser pulses, a technique we will be focusing on in the following sections. Laser spot smoothing techniques are employed to obtain a top-hat intensity distribution from the normal gaussian one.

4.1 Achieving isentropic compression

To isentropically compress a sample up to pressures as high as possible (in the range of several megabar), the temporal profile of the pressure loading must be optimized to avoid shock generation. This analysis can be performed in the framework of the method of characteristics (Figure 4.1a), following the approach taken in [74]. The compression wave generated by the driver travels at the instantaneous sound speed c, more material being brought to the same pressure.

For materials with simple EOS, c is a monotonically increasing function of pressure p, causing the ramp wave to steepen as it propagates. This steepening can be described in the framework of characteristics of the continuum equations.

The characteristics can be represented in two dimensions (position and time) as curves along which disturbances are propagated (Figure 4.1a). For a material with a scalar EOS there are two families of characteristics, propagating forward, respectively backward, at the sound speed c with respect to the flow. While the flow remains ramp-like, the characteristics continue as straight lines in position-time space.

Given that the equation of state has no explicit time dependence, the ramp is monotonic and propagates through homogeneous material (reflections at interfaces being thus excluded), the characteristics are straight lines.

As soon as two characteristics propagating in the same direction intersect, a shock appears. The description complicates considerably after that, as the characteristics start passing through shocked material in which the particle and sound speeds differ, causing the characteristics to bend.

To obtain maximum pressure values in the ramp without generating a shock, the pressure profile of the driver shall be optimized by requiring that the first shock develops as late as possible. For a fixed total rise time of the ramp, the ideal shape would thus be the one for which a shock forms simultaneously over the entire pressure range, that is, the situation in which all the characteristics intersect at the same position and time.

Considering that there is insignificant time-dependence in the response of the material to the loading applied by the driver, the ideal ramp shape can be taken as self-similar with respect to time before the shock formation. That is, inverting the time axis results in a broadening ramp wave, which traced back to the Lagrangian point where the driver is applied (at a distance l_0

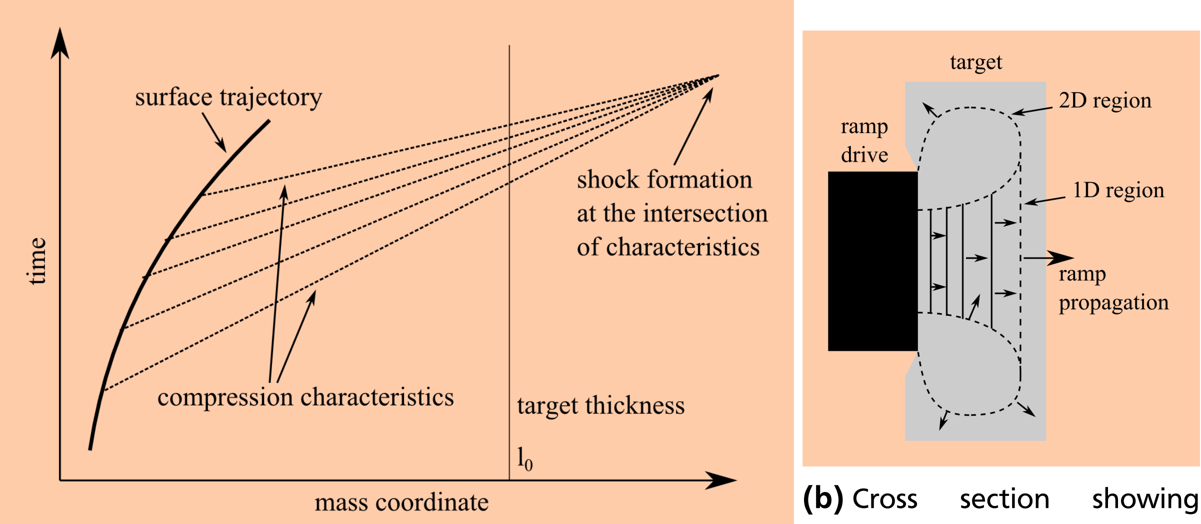

(a) Evolution of characteristics.

(b) Cross section showing lateral release propagating into ramp-loaded material.

Figure 4.1: Ramp loading experiment schematics.

through un-shocked material) gives the ideal loading history.
The cross section through a target during compression in a ramp loading experiment can be seen in Fig. 4.1b. The one-dimensional ramp progresses in the target, continuously being deformed by the edge release in the two-dimensional region. Solid contours in the one-dimensional region represent the contours of equal pressure in the ramp, increasing as getting closer to the drive. The direction of propagation of the waves is shown by arrow in the target. The two-dimensional region propagates laterally more than axially because it does it through material of increasing c.

4.2 nhelix and PHELIX facilities and the Z6 experimental area

These two laser facilities available at GSI were developed along the idea of allowing simultaneous laser and ion beam experiments, in the experimental area Z6. First studies related to the inertial fusion energy research obtained through the combination of laser and heavy-ion beam began in 1995.

4.2.1 nhelix - nanosecond high energy laser for heavy ion experiments

The first high energy laser system that became operational at GSI is the "nanosecond high energy laser for heavy ion experiments" (nhelix). In 2004 it underwent a significant upgrade[68]. The nhelix system is capable of delivering two beams of similar power, but different pulse energy and length: a first beam with 120 J in 14 ns (ns-beam), and a second beam at 5 J in 0.5 ns (sub ns-beam). It runs in a master oscillator-pulsed amplifier (MOPA) configuration, in which a low energy pulse generated by a master Nd:YAG oscillator is amplified in several silicate-glass rod amplifiers, of increasing diameter up to 64 mm.

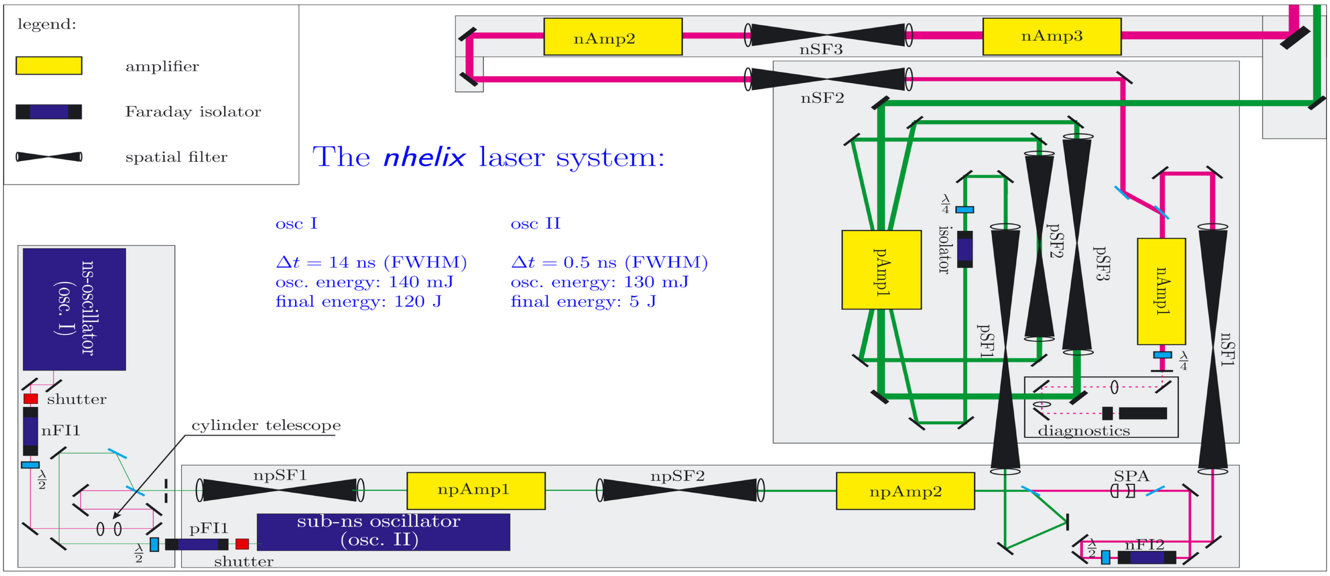

Figure 4.2: Layout of the nhelix laser system [68].

Nanosecond front-end

The ns-oscillator that was used in this work is the Coherent Powerlite 8000. Its elliptical output profile is reshaped with a cylinder telescope for better spatial intensity distribution (the purple line in Figure 4.2). Afterwards the pulse is inserted into the first amplification section (npAmp1 and npAmp2) through two thin film polarizers with which the ns and sub-ns beams of p-polarization and s-polarization, respectively, are brought together. During this phase, the initially gaussian shaped intensity profile changes to a flat top distribution due to the decreasing gain of rod amplifiers towards the centre axis. Such a profile leads to diffraction problems at edges in the optical path, and has to be corrected with a soft polarizing aperture (SPA) before injection in the next amplification section.
After this reshaping, the beam is guided into the double-pass amplifier, prevented from back-reflecting light into the chain by a Faraday isolator. The final step is amplification in two rods with diameters of 45 mm and 64 mm, respectively, and then the laser beam is relayed into the target chamber.

Sub-nanosecond front-end

The sub-nanosecond front-end is used generally for Thomson scattering characterization of targets. It outputs 0.5 ns long pulse of 5 J. The final amplification of the sub-ns beam is realized in a geometrical triple pass configuration.

4.2.2 PHELIX - Petawatt High Energy Laser for heavy Ion eXperiments

The PHELIX project was started in 1998 as a joint venture between GSI, Lawrence Livermore National Laboratory (LLNL) and the Max Born Institute in Berlin [69]. The desired parameters of the laser system were energies of 5 kJ in long (nanosecond) pulses or alternatively pulses of ultra-high peak power (>1 PW) for focused intensities above 10^{21} W/cm^2, making it one of the

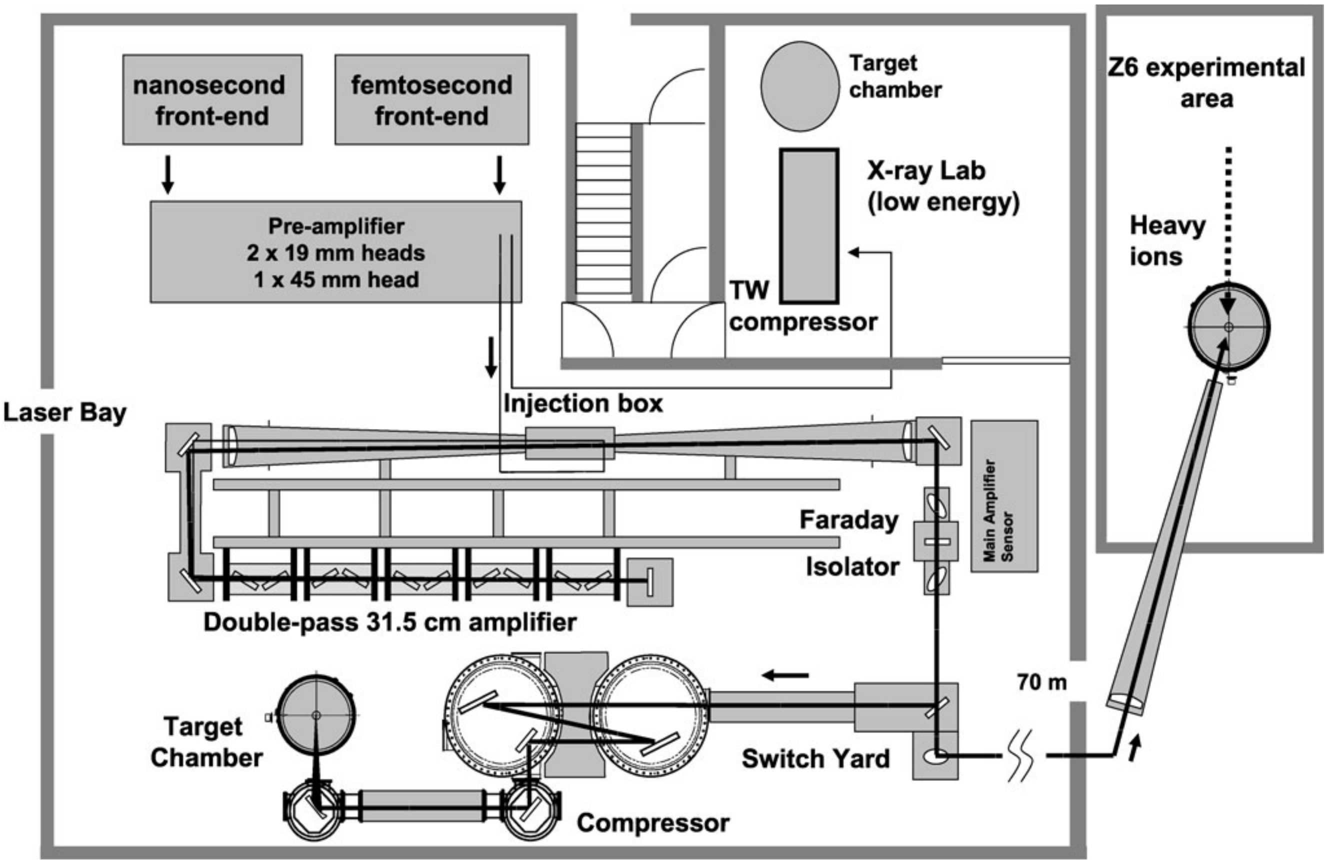

Figure 4.3: Layout of the PHELIX laser system and Z6 experimental area [71].

few HEPW (High Energy Petawatt) laser in the world.

The main amplifier (MA), the high-voltage pulsed power system and diagnostic tools were built using components from the NOVA laser-system coming from the French Commissariat à l'énergie atomique (CEA) and LLNL. The main system consists of a Nd:glass solid-state laser. Current maximum energies reach 0.5-1 kJ/pulse and power up to 0.5 PW. Two front-end systems are used which output either pulses (1-20 ns) or ultra-short (500 fs) pulses.

The entire laser system is housed in a separate building, in which a thick concrete floor serves as vibration insulated optical table. From this building the laser beam goes either directly to the Laserbay or through an 80 m long pipe to the Z6 experimental area.

Final spot sizes of 10-30 μm are obtained in these experimental areas, corresponding to intensities up to 10^{21} W/cm^2 with which highly energetic states of matter can be reached.

Typical repetition rates are from 1 shot per 20 minutes to 1 shot every 2 hours, depending on the energy and power requirements. Laser triggering and control is performed with software developed under LabVIEW.

Femtosecond front-end

A commercially available Ti:sapphire laser oscillator from Coherent generates pulses at a frequency of 76 MHz, with a pulse duration of 100 fs and at an energy around 5 nJ. The resulting pulse must be spatially and temporally stretched before further amplification. This procedure is known as the Chirped Pulse Amplification (CPA) technique, through which amplification up to

petawatt levels is possible.
After this stretching, the pulse is amplified in two regenerative Ti:sapphire amplifiers, running at a repetition rate of 1 Hz. The energy is increased to approximately 30 mJ, with an intensity contrast over 60 dB realised with ultra-fast Pockels cells. Also two pulses with tunable separation, energy and aspect ratio can be obtained using a Mach-Zehnder interferometer.
Two dielectrically coated reflective gratings (MLD - multilayer dielectric grating) with grating constants of 1600-1800 lines/mm are used to recompress the pulse, which now has a diameter of ≈25 cm.

Nanosecond front-end

Pulses between 700 fs and 20 ns long, with custom shapes can be obtained with the system coming from LLNL. The amplified output of a commercial CW laser is modulated with an AOM to 100 ns pulses, that are shaped within an optical fibre system using an intensity modulator connected to a programmable wave generator.
The resulting 10 nJ pulses are further amplified within a regenerative Nd:glass ring amplifier up to energies around 20 mJ, at a repetition rate of 0.5 Hz.

Preamplifier

The preamplifier consists of two pumped Nd:glass rods 19 mm and 45 mm in diameter which bring the energy up to around 1 J. Both short and long pulses can be coupled and gradually expanded in Kepler telescopes, in order to bring the intensity below the laser damage threshold of the optical components. Wavefront errors are corrected with adaptive optics such as Shack-Hartmann sensors and deformable mirrors, or by spatially filtering the beam.

Main amplifier

The main amplifier (MA) works in a double pass configuration (DPA - Double Pass Amplifier). In this configuration the high energy pre-amplified pulse travels twice through two platinum free potassium-barium-aluminium-phosphate glass rods doped with 2% Nd^{3+} ions, at the Brewster angle to prevent reflections. Population inversion is obtained with two collinear reflective coated optical pumping flash-lamps running at 18 kV and 3.5 kA, giving 1 ms pulses. Also, the amplifier is optically isolated using a Faraday isolator to prevent optical feedback.

Frequency doubling system

This system was commissioned in 2010 for better generation and heating of plasmas, due to the better coupling of visible light. The Second Harmonic Generator (SHG) converts the infrared 10^{-9}-10^{-8} ns long laser pulses into green pulses at a wavelength of 527 nm. A DKDP (deuterated potassium dihydrogen phosphate) Type II crystal 310 mm in diameter and 25 mm thick is used as non-linear medium, optimized for conversion ratios up to 60%.

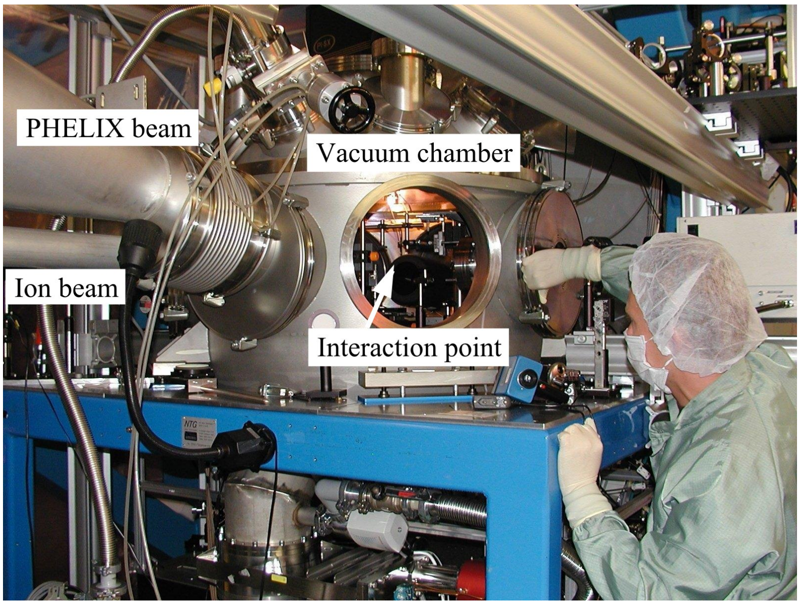

Figure 4.4: Target chamber in the Z6 experimental area of GSI.

4.2.3 Z6 experimental area

The Z6 experimental area is situated in the UNIversal Linear Accelerator (UNILAC) hall of GSI. Ion beams of energies up to 13 AMeV coming from UNILAC can be combined there with laser beams (coming from nhelix or PHELIX) in a common interaction area (Figure 4.4). The target chamber can be brought to a vacuum of 10^{-6} mbar, and the interaction point can be visualized through multiple windows, as for example with a Wollaston interferometer with multi-frame acquisition to observe the electron density in the resulting plasma [72].

4.3 Experiment description

The properties and behaviour of matter under extreme pressures and strain rates are of importance for many basic research domains such as astrophysics, physics of dense plasmas and planetary physics as well as for numerous applications. The theoretical description of matter in such states still remains uncertain, demanding further experimental studies supporting theoretical investigations. Detailed knowledge of the equation of state (EOS) and phase transformation kinetics are for example crucial for a correct description of the earth core and mantle, impact of meteoroids and projectiles, the modeling of giant planets [96] and inertial fusion research [97]. We will illustrate this with the case of the iron EOS, which is also the primary aim for the performed experiment. Iron is the most abundant element in the earth core, amongst impurities of Si, Ni and other light elements. As known from seismic data, the outer earth core is liquid, while the inner earth core is solid. Melting and solidification processes at the solid-liquid interface play an important role for the understanding of the convection in the earth core, which is also responsible for the generation of the earth magnetic field. In addition, simulations indicate the existence of a second bcc solid-state phase at pressures and temperatures close to the solid-liquid boundary of the earth core. The region of the phase diagram of iron relevant for earth core conditions can be seen in Figure 4.5a. With current methods it is difficult to reach: in static compression experiments, the achieved temperature and pressure are too low, whereas

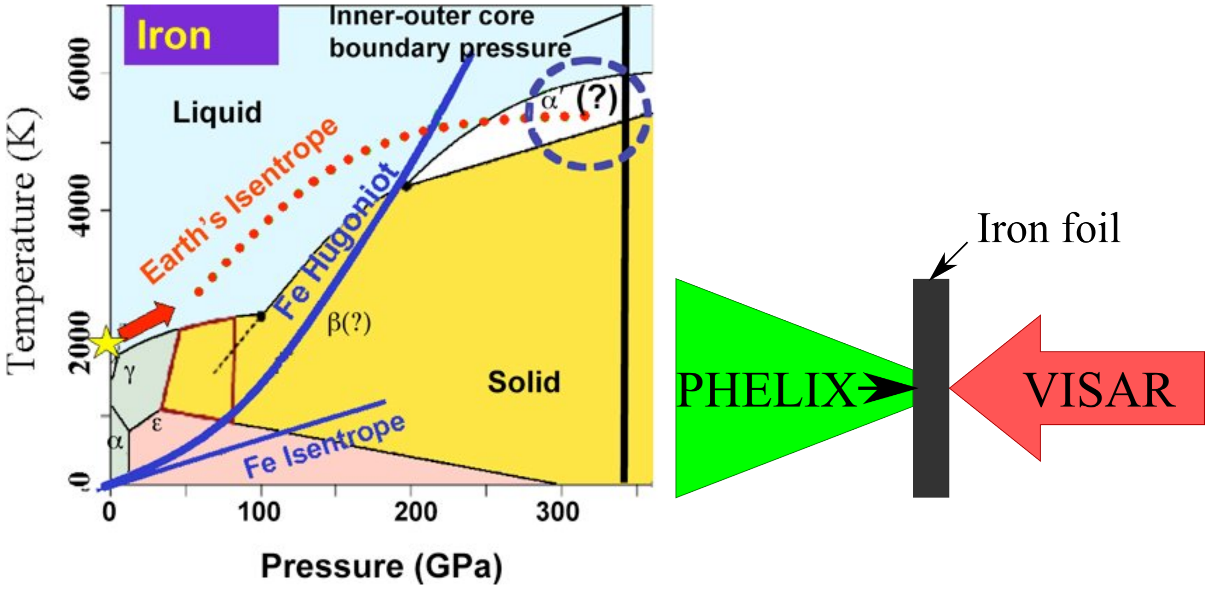

(a) **(b)**

Figure 4.5: (a) Phase diagram and (b) target set-up for isentropic compression of iron experiments with PHELIX.

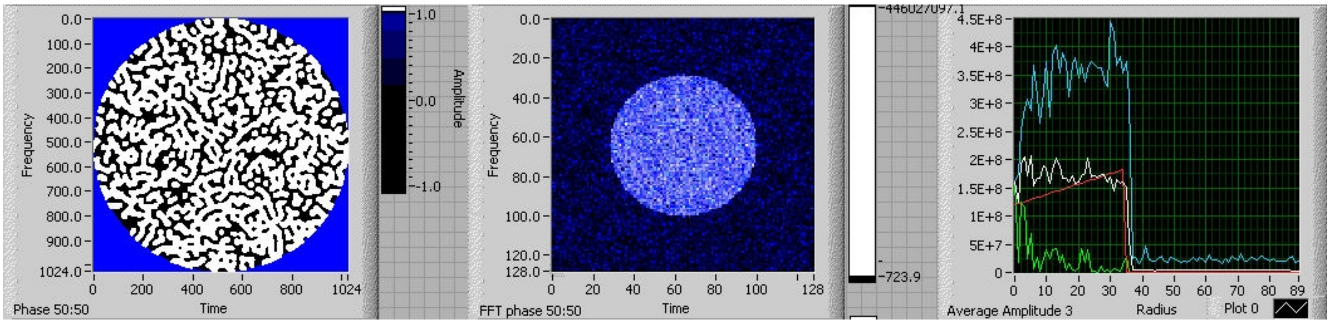

Figure 4.6: Profile flattening phase plate design: near field binary phase distribution (left), far field intensity distribution (middle) and the radially averaged intensity profile (right).

in shock-wave experiments the necessary pressure cannot be reached without overheating.
The technique implemented here consists in following an isentrope in the phase diagram, which permits higher compression at lower temperatures than when using shocks.
To reach the proposed region of the phase-diagram, the nanosecond front-end of PHELIX was used. Its Gaussian profile was converted to a top-hat profile using a custom designed diffractive phase plate shown in Figure 4.6. The design was realised using the method described in [98], by implementing a modified form of the Gerchberg-Saxton algorithm [99] for phase plates with binary patterns, for frequency doubled operation of PHELIX at 527 nm, pulses ≈150 J in energy and ≈10 ns long. With a diameter of 25 cm, it was mounted in the parallel beam before the final 1 m focusing lens. The resulting average intensity over the 1 mm focus was 10^{12} W/cm^2.

4.4 Diagnostic instruments

The main diagnostic instruments were two imaging line VISARs developed in the frame of this work, with two streak cameras from Hamamatsu as interferogram recording devices. The working principle of a streak camera was previously presented in Section 3.4.3, and of an imaging VISAR in Section 2.2.3. In the following section, the actual implementation of the developed interferometers is described.

4.4.1 Line imaging Velocity Interferometer System for Any Reflector - line VISAR

As discussed in Section 2.2.3, optical velocity measurements are based on the Doppler effect. The type of interferometer briefly discussed in Section 2.2.3 was implemented (Figure 4.7). The etalons were made of fused silica, antireflection coated for the visible spectrum on both surfaces, with an index of refraction n = 1.4607 at 532 nm. They had lengths h of 50 mm and 15.04 mm, corresponding to delay times $\tau = (2h/c)(n - 1/n)$ between the arms of 258.7 ps and 77.8 ps, respectively.

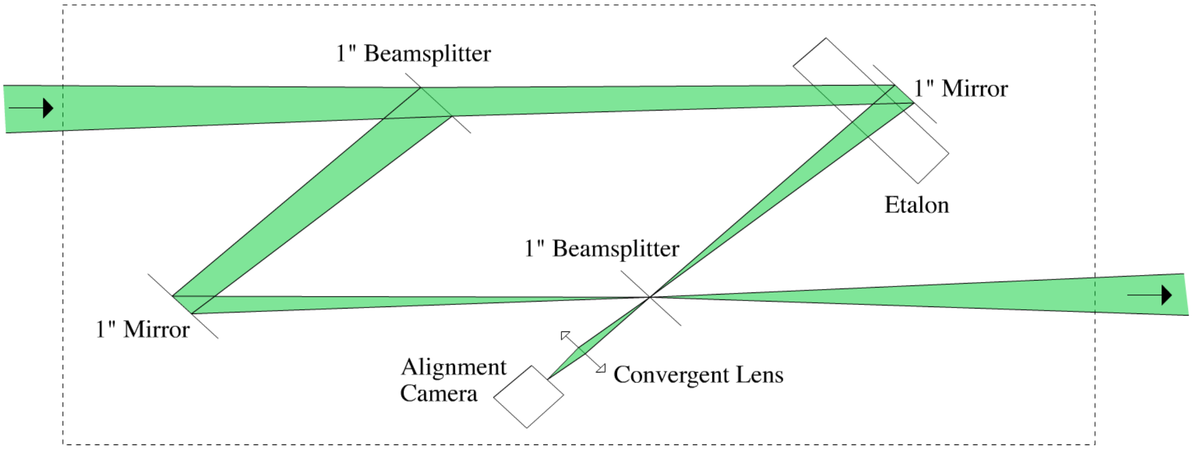

Figure 4.7: Schematics of the line VISARs deployed in isentropic compression of iron experiments.

Given the dispersion corrected VISAR sensitivity formula in [37]

$$VPF_0 = \frac{\lambda}{2\tau(1+2\delta)}, \tag{4.1}$$

where $\delta = 0.0318$ for fused silica at 532 nm, the velocity sensitivities are 1027.3 m/s/fringe and 3415.3 m/s/fringe, respectively.

Due to the relatively long delay times, attention must be given to the temporal coherence of the diagnostic light source. Usually a seeded pulsed laser provides the necessary parameters. In the work presented here, a glass fibre 0.6 mm in diameter was used to inject the laser beam into the optical system.

Alignment procedure

To obtain maximum measurement accuracy, the arms of the interferometer must be of equal length, within micrometric precision. For that purpose, this part of the alignment procedure is done with white light, with a coherence length of only a few micrometers.

A motorized linear stage is used to scan for white light fringes that appear only when the difference between the two arms is less than the coherence length.

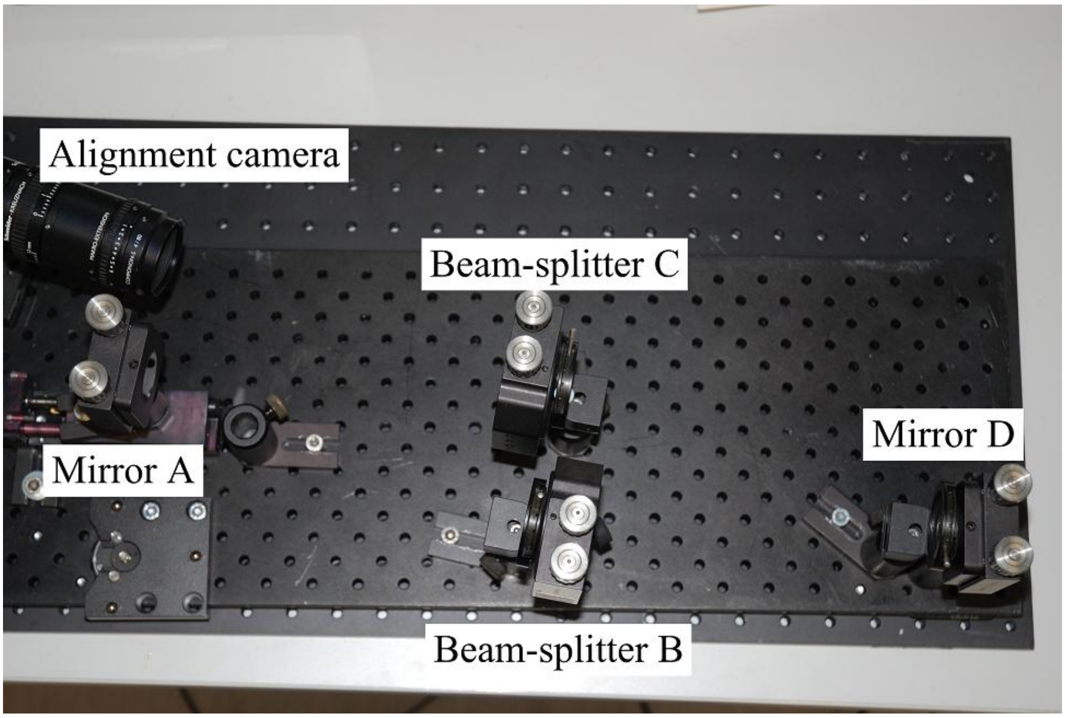

Figure 4.8: Sub-centimetre alignment of line VISAR.

After finding this position, the etalon is introduced and the translatable mirror is moved by the calculated distance to obtain again the spatial superposition of the images of the cross formed by the different reflections on the mirrors. At this point the white light fringes disappear. A detailed description of the alignment procedure of the interferometer is given below.

Rough alignment of the interferometer
a) The arms of the interferometer are brought to approximately the same length (difference under 1 cm) using a ruler (Figure 4.8).
b) An alignment laser beam is centred through beam splitter D and mirror B, defining the input axis (Figure 4.9a).
c) The alignment laser beam is centred on mirror A with beam splitter B (Figure 4.9b).
d) The alignment laser beam is centred on beam splitter C with mirror D (Figure 4.10a).
e) The output axis is defined by centring the laser beam on beam splitter C with mirror A (Figure 4.10).
f) The transmitted and reflected laser beams are made collinear using beam splitter C. At this point, fringes should appear (Figure 4.11). 4.11).

Spatial superposition of the beams
The beams going through the interferometer arms must be well superposed on the diagnostic cameras to correct for the short spatial coherence of the input light.
a) An image of the coated surface of beam splitter C is obtained on the alignment camera (Figure 4.12).
b) A cross hair is introduced in the input beam and imaged on beam splitter C, by getting an image of it on the previously set alignment camera (Figure 4.13).
c) The images of the cross-hair are superposed with mirror B (Figure 4.14a).

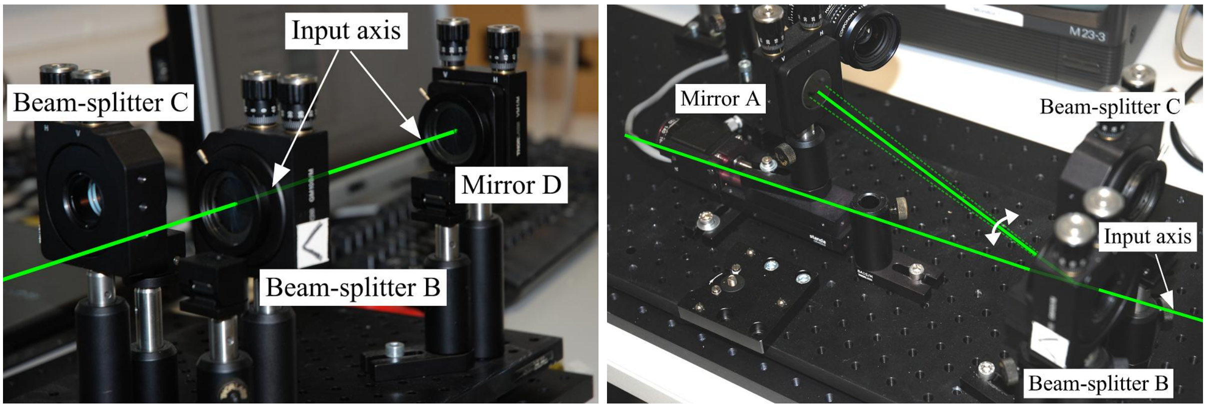

(a) (b)

Figure 4.9: Defining the input axis of a line VISAR (a) and centring on the motorized mirror (b).

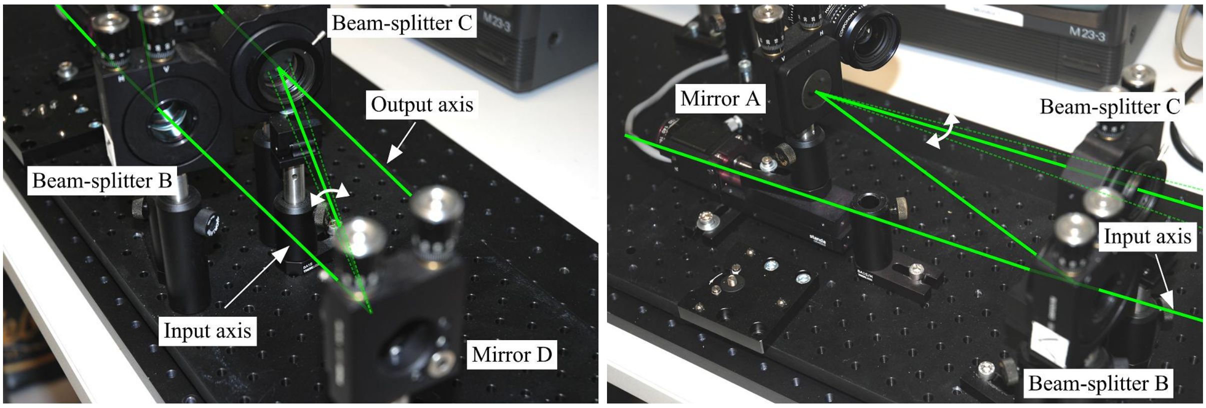

(a) (b)

Figure 4.10: Centring on the fixed mirror (a) and defining the output axis (b) of the line VISAR.

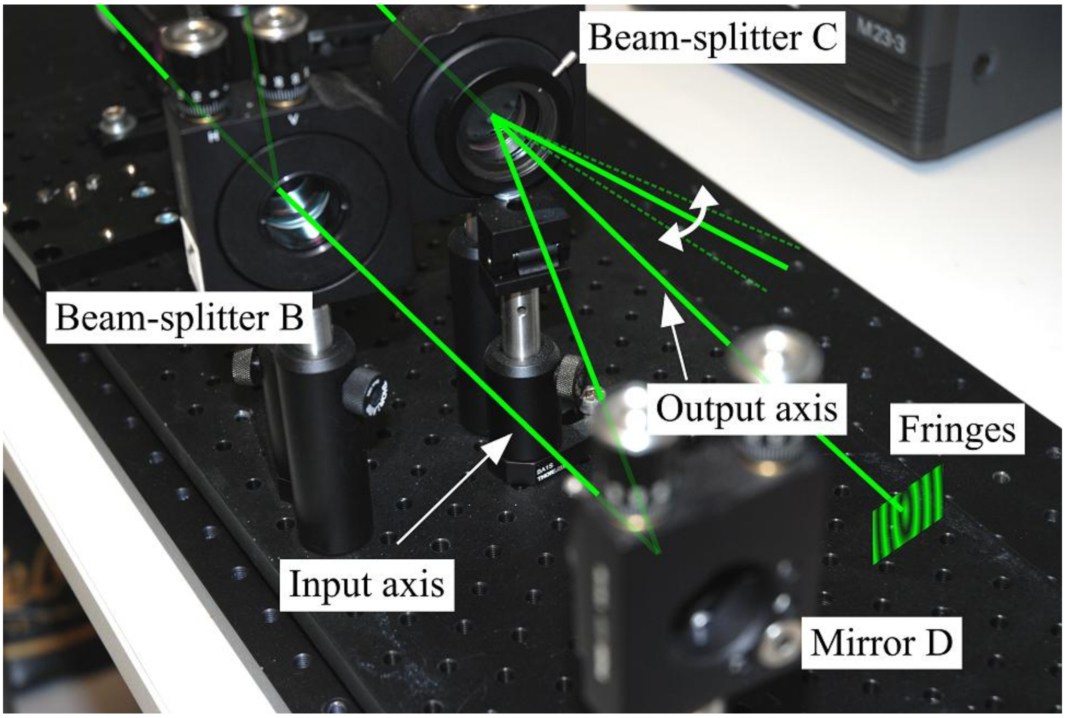

Figure 4.11: Obtaining fringes in laser light with a line VISAR.

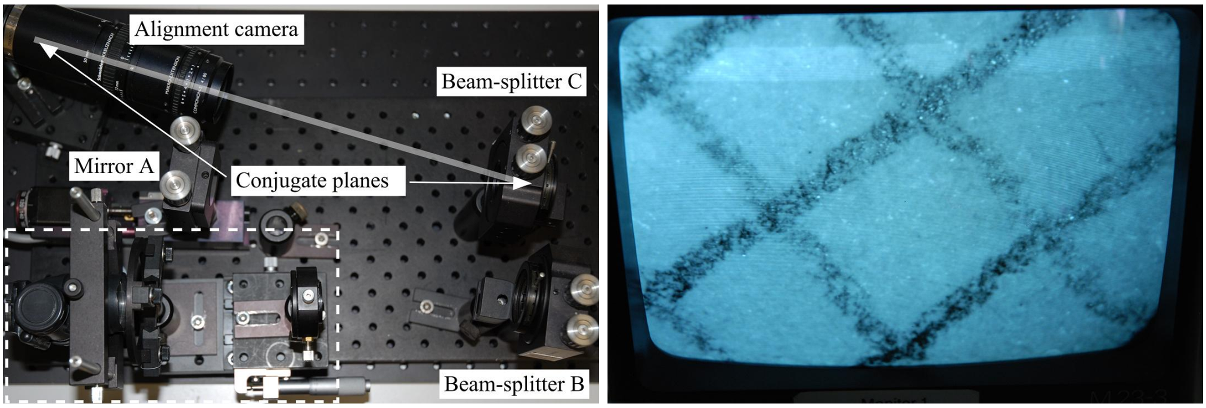

(a) (b)

Figure 4.12: Setting up a pair of conjugated image planes between the camera and beam splitter C: a grid target is brought on the coated surface of beam splitter C, and its image shown in (b) is obtained on the alignment camera.

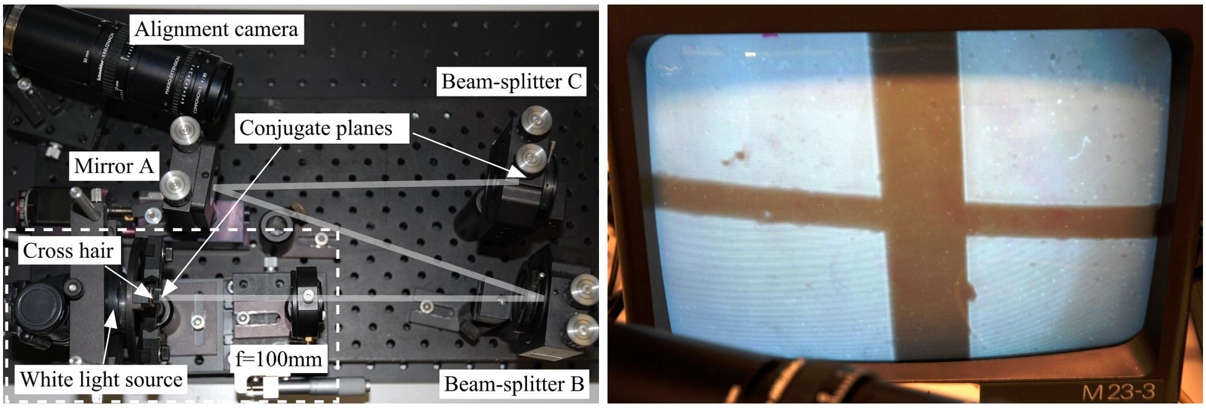

(a) (b)

Figure 4.13: Setting up a pair of conjugated image planes between the cross hair and beam splitter C: a cross hair is introduced in the input axis and imaged through a 100 mm lens on the alignment camera, which results in imaging it on the coated surface of beam splitter C, given the previous step.

d) The fringe spacing is changed with beam splitter C. A density of around 10 fringes on the screen is acceptable (Figure 4.14b).

Micrometric precision alignment of arms of the interferometer
a) The alignment laser is changed with a source of white light (a white LED).
b) An interference filter centred on the laser wavelength and of 10 nm bandwidth is inserted to increase the coherence length to approximately 30 μm.
c) The movable mirror is translated in one direction at low velocity (10 μm/s). The spatial superposition of the cross hair images must be maintained with mirror B. Also the fringe density must be checked every couple of millimetres and kept around five fringes per screen with beam splitter C (as seen in Figure 4.14b). After a distance of more than 10 mm travelled in one direction without finding fringes, the motor should be brought in the zero position and looking for fringes should be done in the opposite direction.

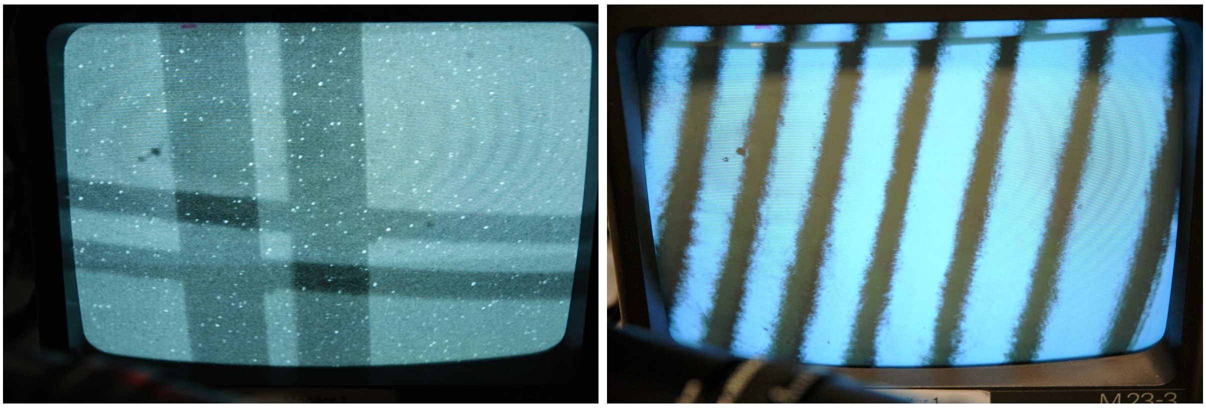

(a) (b)

Figure 4.14: Obtaining spatial superposition of beams (a) and setting the fringe density (b).

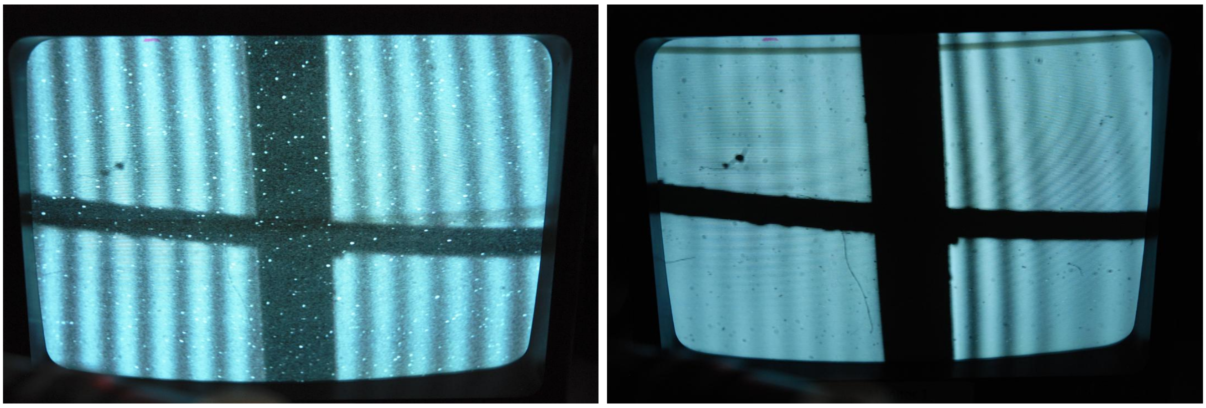

(a) (b)

Figure 4.15: White light fringes with the 10 nm filter inserted (a) and without it (b).

d) When fringes are found, the distance to the optimum position is under 30 μm. As can be seen in Figure 4.15a, the contrast does not vary across the $\approx$10 fringes on the display, as the OPD generated by the tilted beasmplitter C is under 10 μm, under the coherence length given by the interference filter.
h) With the interference filter removed, the movable mirror is translated in micrometre steps until the white linght fringes are centred on the cross-hair. The spatial superposition of the cross hair images must be maintained with mirror B.The fringe spacing is changed with beam-splitter C (Figure 4.15b). This time, only a few fringes can be seen, due to the very short coherence length under a few micrometres. Finally, when changing back to laser light, a fringe density around 10 fringes per display should be still visible.

4.5 Commissioning of the line VISAR in experiments with nhelix as driver

In this preliminary beam-time some tests were performed with the VISAR system, using nhelix as driver and a pulsed Continuum YLF laser as diagnostic beam. These experiments served to gain experience with target alignment and time synchronization procedures at Z6.

4.5.1 Experimental set-up

The MiniLase II used as diagnostic laser for the line VISAR operates at a wavelength of 532 nm, ≈7 ns pulse length. Being an unstabilized system, its coherence length is on the order of a few mm, which required the use of short etalons (1.5 mm fused silica in this experiment, corresponding to a velocity sensitivity of 34244m/s/fringe). Aluminium foils of 50 μm thickness were used, hit by nhelix pulses of ≈50 J at 532 nm, in the target geometry shown in Figure 4.5b (with PHELIX being replaced by nhelix).

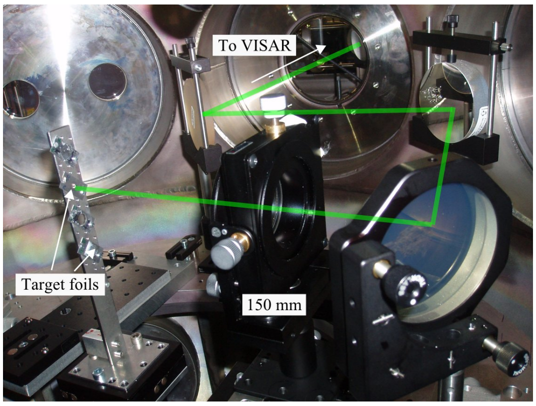

(a) Imaging system to target chamber.

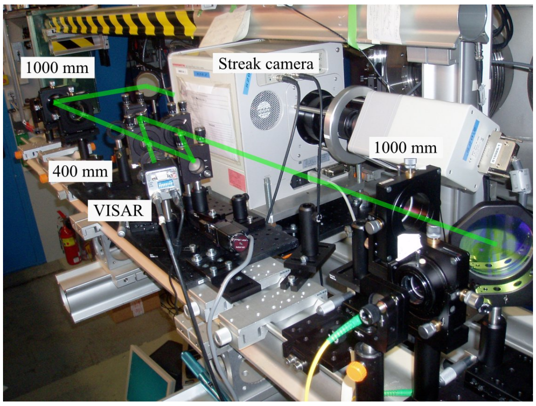

(b) Imaging system to streak camera.

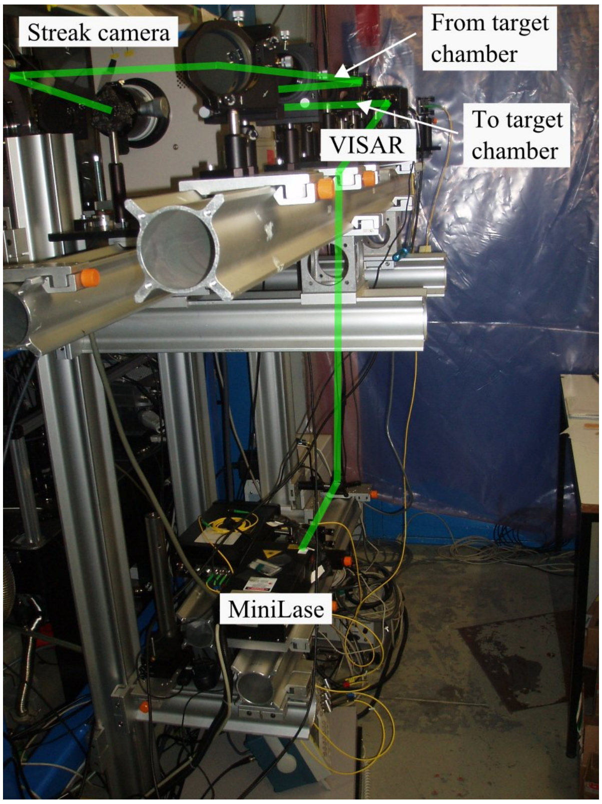

(c) Laser injection.

Figure 4.16: Interferometer and imaging optics during commissioning of the line VISAR.

4.5.2 Interferogram analysis and results

The interferograms showed poor fringe contrast due to the short coherence length of the diagnostic laser, even though short etalons were used (Figure 4.17a). Given the low velocity sensitivity of 34 km/s/fringe, no fringe movement could be observed during shots (Figure 4.17b). Also, because the wavefront of nhelix was not flattened, the expansion of the target material is markedly bi-dimensional.

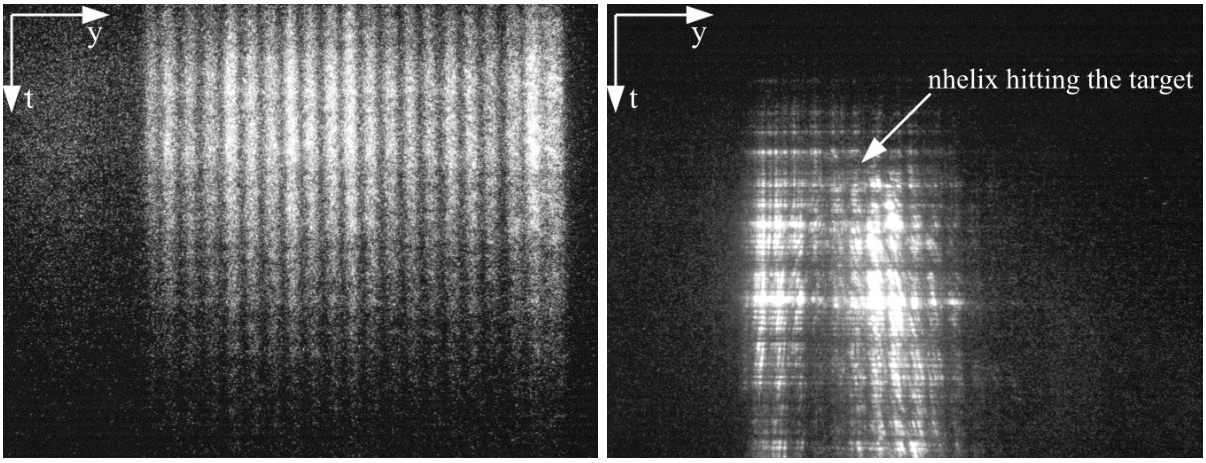

(a) **(b)**

Figure 4.17: Interferograms acquired during commissioning of the line VISAR: (a) reference interferogram in static conditions, with relatively poor fringe contrast due to short coherence length of diagnostic laser; (b) interferogram of shot 14 showing loss of reflectivity after hit, without fringe movement due to low velocity sensitivity.

4.6 Experiments with PHELIX as driver

During the main beam-time with PHELIX, nhelix was slightly modified to be used as diagnostic laser for the VISARs. Its pulse length was increased to 25 ns, and only one or two amplifiers were used. The coherence length was well suited for longer etalons (5 cm), therefore the fringe visibility and velocity sensitivity were greatly improved over the previous beam-time.

4.6.1 Experimental set-up

The two line VISARs were installed on a movable table. Due to major space constraints in the Z6 target area, the optical path of the imaging system was folded several times. The final image for both systems was rotated by 90°, the line imaged on the streak cameras corresponding to a vertical line on the target.

The line VISARs could be aligned during the experiment by having a 2 mW 543 nm alignment laser injected into the optical path.

The target can be illuminated using an optical fibre connected to a white light source that can be switched with the nhelix injecting fibre. An imaging system was used in the target chamber to align the PHELIX beam on the same spot that is imaged on the diagnostic system. The PHELIX beam in 10 Hz low energy mode is imaged together with a needle target that was previously moved into a reference position. The same needle target is imaged on the VISAR alignment cameras and the streak cameras in fixed positions that are marked.

The streak cameras were spatially calibrated with a stage micrometer with the finest divisions at 10 μm and spatial resolution was found to be better than 50 μm. Temporal calibration was performed with the PHELIX front-end at 150 fs.

Iron foils having thicknesses of 10 μm, 19 μm and 25μm were used as targets, light reflected on their free surface being collected with an F/3.0 lens, of focal length 150 mm and diameter 50.8 mm. This lens represented a compromise between light collection efficiency, imaging aber-

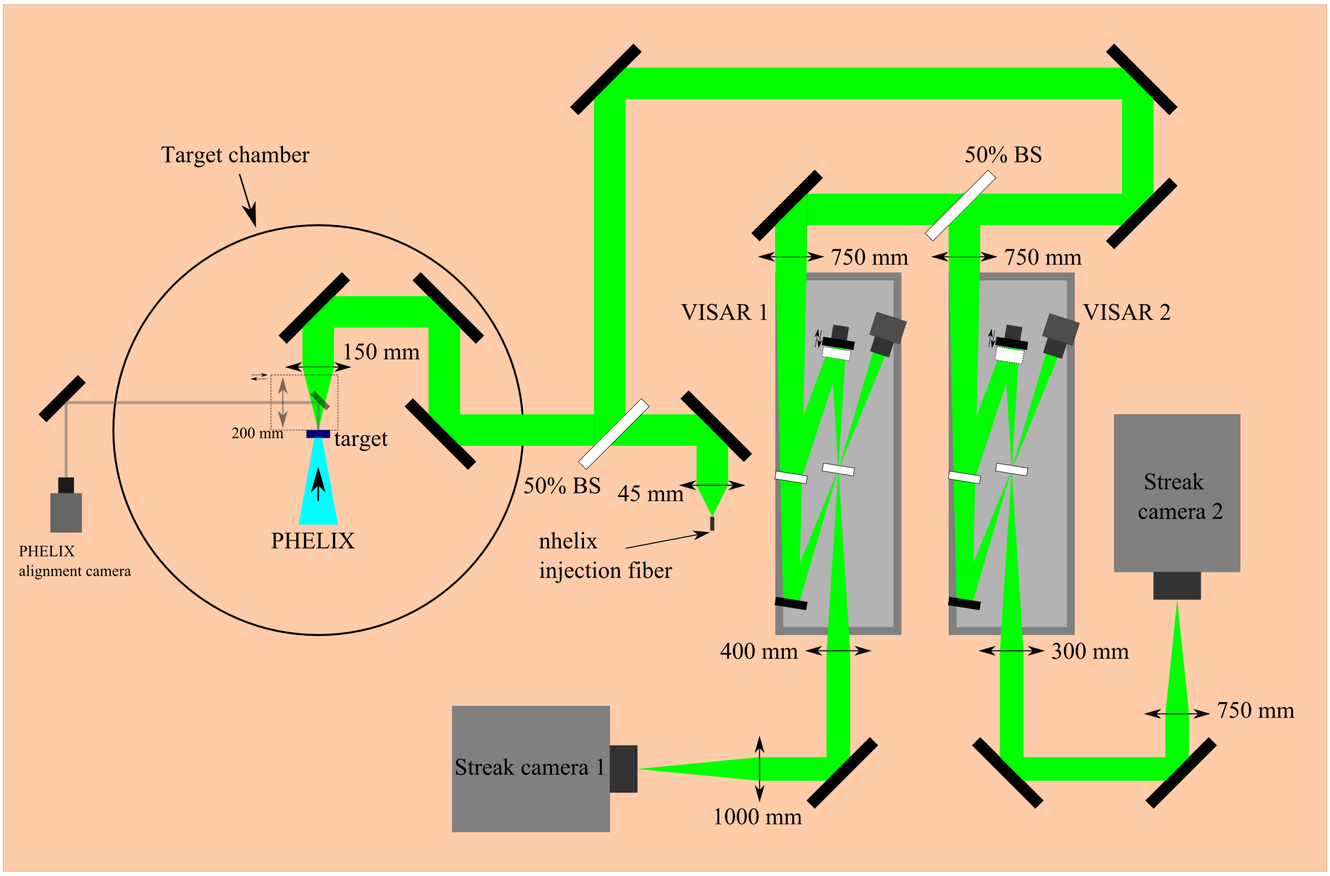

Figure 4.18: General schematics for the iron isentropic compression experimental set-up with PHELIX as driver, showing the dual line VISAR set-up on the right, and the target chamber set-up on the left.

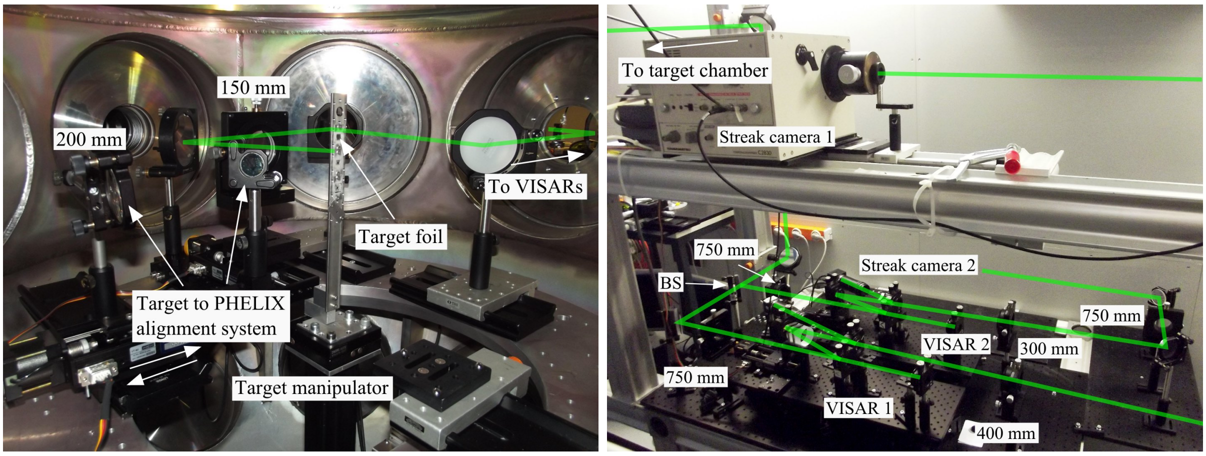

(a) Target chamber. **(b)** line VISARs optical set-up.

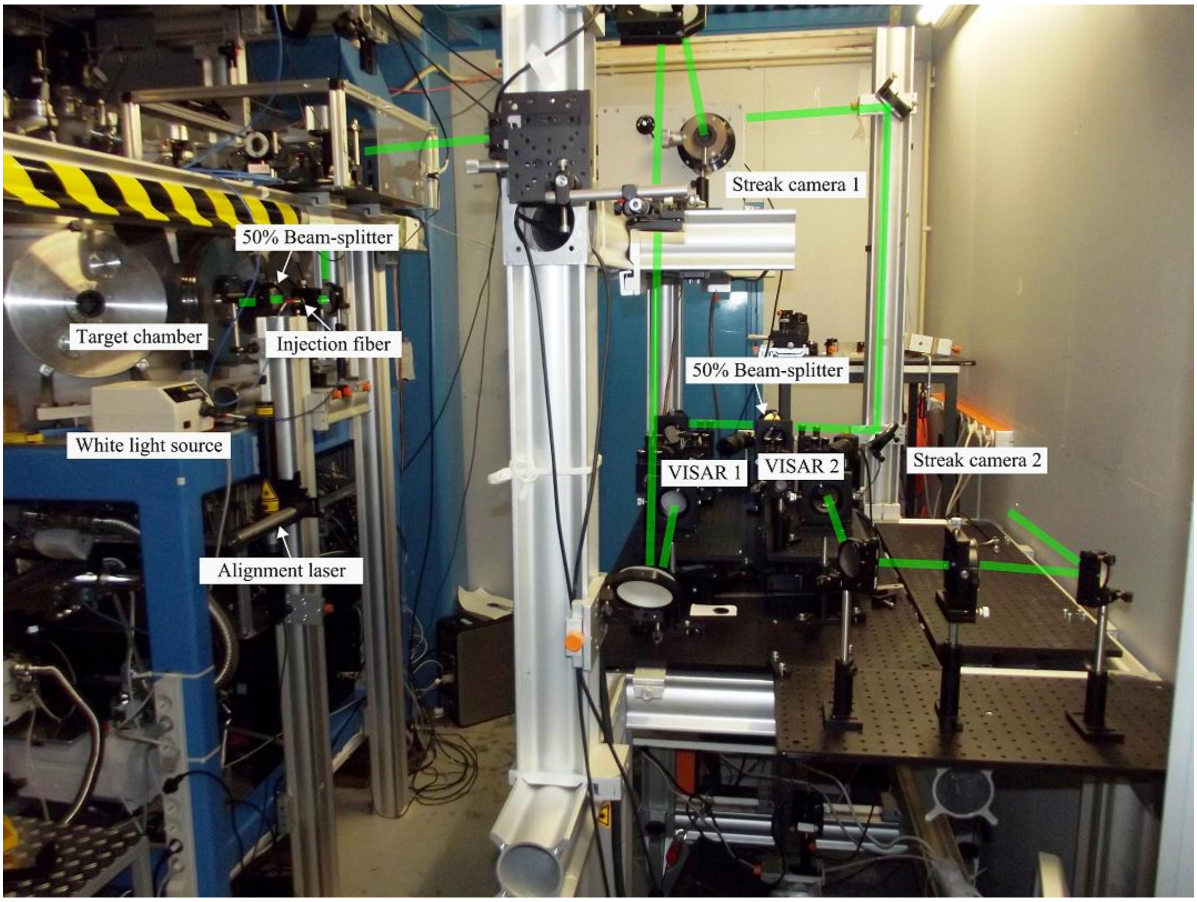

(c) Imaging and alignment optical systems.

Figure 4.19: Dual line VISAR experimental set-up, with the target chamber interior depicted in (a), a close-up of the line VISARs in (b) and a general view of the image relaying optical system from the target chamber to the interferometers and streak cameras in (c).

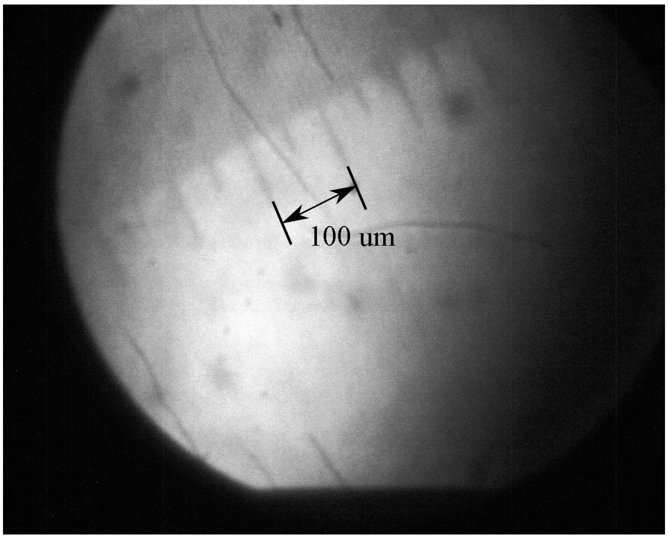

Figure 4.20: Spatial calibration of streak camera during iron isentropic compression experiments with PHELIX.

rations and damage caused by flying debris from the target. It was protected with a plexiglass shield, which at this distance from the interaction point lasted for more than 5 shots, which was the maximum number of foils that could be mounted on the holder. The coated (R=1 @532 nm) surfaces of the alignment beam splitters in the interferometers (beam splitter C in Figure 4.8 from Section 4.4.1) were used as intermediary imaging planes for the target surface, with the final imaging planes lying on the streak camera slits.

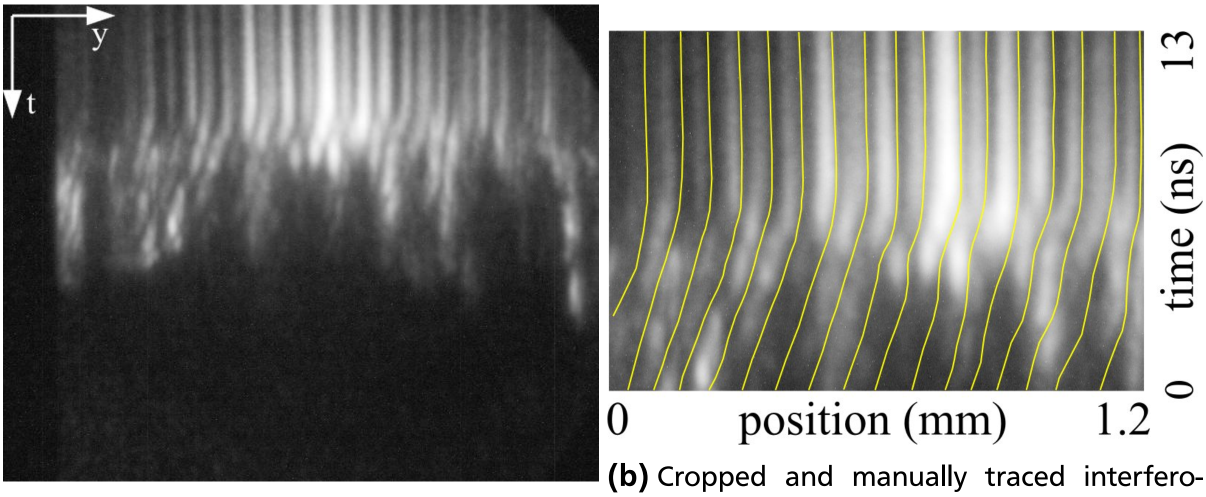

(a) Unprocessed interferogram.

(b) Cropped and manually traced interferogram in the region of interest.

Figure 4.21: Raw and processed interferograms for shot 18 on iron target of 25 μm, with 130 J at 527 nm.

4.6.2 Interferogram analysis and results

Interferograms were traced manually and the phase-map was obtained following a similar procedure to the one described in Section 3.6.3. The phase-map was afterwards converted to a

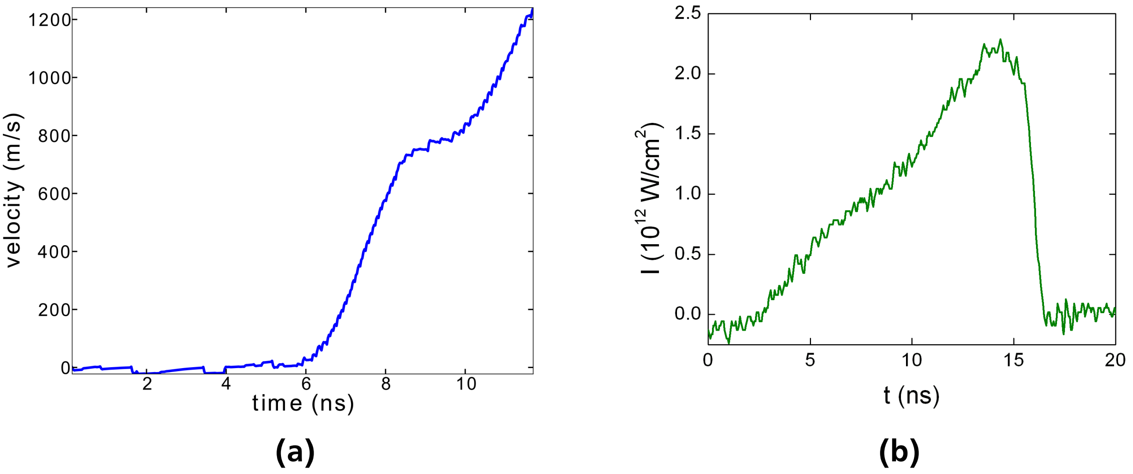

(a) **(b)**

Figure 4.22: Surface velocity profile (a) and the corresponding intensity profile for PHELIX (b), for shot 18 on Fe 10 μm at 130 J.

velocity map using the appropriate VISAR sensitivity.

As can be seen in Figure 4.21a, the reflectivity of the rear surface decreases rapidly after the target is hit, therefore the interferogram must be cropped to a smaller region of interest of good contrast, in order for the fringes to be properly traced (Figure 4.21b) and the phase-map to be correctly interpolated.

The lack of discontinuities in the velocity profile in Figure 4.22a confirms the absence of a shock. The plateau-like structure in the velocity profile from Figure 4.22a between 8 and 10 ns is related to the well known $\alpha - \epsilon$ phase transition in iron at 130 kbar [101]. During the transition a mixed phase exists in the sample, which is more compressible than both phases, therefore until the transition is completed, pressure remains approximately constant. The velocity at which the transition happens is related to the dynamics of the transition. The length of the plateau is given by the time needed to transform all matter from the α state to the ϵ state. The incubation time of the transition and length of the plateau depend on the compression rate, therefore by comparing different rates, information about the dynamics of the phase transition can be obtained [102].

To obtain the actual pressure profile, the iron isentrope shown in Figure 4.23b starting at room conditions was used. The relation between the measured surface velocity U_S plotted in Figure 4.22a and particle velocity U_P is given in [103, 104] by

$$U_P = \frac{U_S}{2}, \tag{4.2}$$

considering that iron expands in vacuum, therefore there is no impedance matching.

The resulting pressure profile can be seen in Figure 4.23a. The results obtained here are in good agreement with other results obtained in experiments conducted at the LULI2000 and Janus (LLNL) laser facilities [105]. In these cases the experimental set-up was approximately the same with the one described in this work, with two line VISARs and 12.5 μm thick iron targets (compared to 10 μm used here). The main lasers were running at 527 nm like PHELIX, delivering 50-400J on target in a shaped pulse with around 4-5 ns of duration, compared to the longer 15 ns pulses of PHELIX, with flattened spatial intensity profiles.

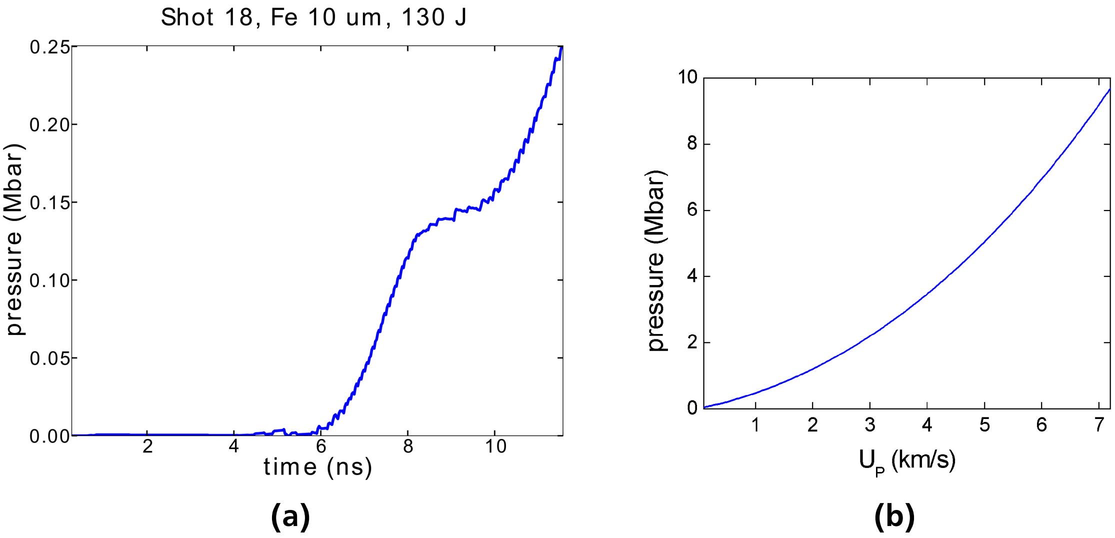

Figure 4.23: Pressure profile determination (a) using a calculated isentrope starting at room conditions (b).

As can be seen from Figure 4.22a, the plateau obtained with PHELIX at 130 J appears at a surface velocity of 800 m/s, corresponding to a particle velocity of 400 m/s, and lasts for approximately 2 ns. These values are similar to what was obtained in [105] for a pulse energy of 126 J (the green profile in Figure 4.24).

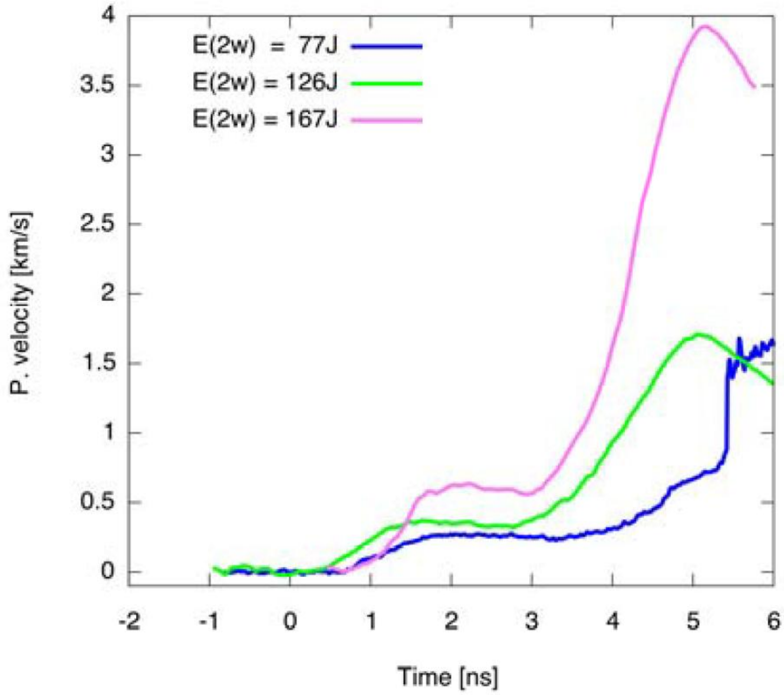

Figure 4.24: Particle velocity profiles measured at LULI2000 and Janus (LLNL). With increasing compression rate, the particle velocity for the plateau gets higher, while its duration decreases [105].

5 Conclusions and outlook

In this work two velocity/pressure investigation tools were developed and commissioned in WDM experiments: an imaging displacement interferometer for the m/s (kbar) range and a double line VISAR system for the km/s (Mbar) range. The interferometers were used in two different experimental research areas: near-critical states of metals induced by heavy ion beams and laser driven planar isentropic compression of iron. Both interferometric systems are of the imaging type, in order to take advantage of the advanced streak cameras available for temporal image recording. On the other hand, due to the fact that the velocity and pressure parameters characterising these experimental configurations differ by 2-3 orders of magnitude, the interferometric systems are implementing substantially different optical schemes.

Study of near critical states of metals by intense heavy ion beams

The imaging displacement interferometer was deployed in heavy-ion beam driven experiments at the HHT area of GSI in the study of lead near the critical point. The HED states were reached using sub-microsecond uranium beams, at 350 AMeV and $\approx 3 \cdot 10^9$ particles/pulse.

In the commissioning phase, the interferometer employed a configuration where pressure measurements were separated from temperature measurements. The reachable pressure range was estimated to several kbar and the velocity of sound in sapphire was measured in good agreement with literature data.

By integrating the light collection system of the interferometer on the pyrometer head, simultaneous recording of temperature and pressure was made possible, through which data for the $P - T$ phase diagram of lead was obtained up to 1-2 kbar and 8000 K near the critical point, with reproducible results from shot to shot. A droplet size of 0.41 μm in superheated states was determined, and kinematic effects were observed above the spinodal curve.

At higher ion beam intensities, such as up to $5 \cdot 10^{11}$ particles/pulse that will be available at FAIR, the critical region of other metals, especially refractory metals such as tungsten, tantalum or titanium will be probed by the same methods.

Laser driven planar isentropic compression of iron

The line VISARs were commissioned in laser driven isentropic compression experiments at the Z6 area of GSI in the study of iron at several hundred kbar pressures, especially during the $\alpha - \epsilon$ transition. The PHELIX system at 15 ns pulse length and $\approx$150 J pulse energy was used as driver to compress iron foils of 10-50 μm thickness. Velocities up to 1300 m/s corresponding to pressures up to 250 kbar could be measured. These were reached in less than 5 ns at high accelerations, but without shocks. Data collected in this work will be used in conjunction with data obtained at LULI at shorter pulse lengths ($\approx$5 ns) to model the dynamics of the $\alpha - \epsilon$ transition at different compression rates and laser pulse lengths.

Furthermore, pressures up to several Mbar can be obtained and recorded deploying a better designed PHELIX wavefront flattening phase plate, to reach the range relevant to Earth's core conditions, and planetary physics in general.

Outlook

In the commissioning phase of the imaging displacement interferometer, vignetting along the optical path induced non-uniform illumination across the field of view and short focal length lenses degraded the image resolution, issues that were solved by increasing the length of the target arm using lenses with longer focal lengths. This permitted better and easier alignment of the optical elements, but fringe contrast was decreased due to a mismatch in the length of the arms, despite the coherence length of several meters of the diagnostic laser. Contrast can be improved by choosing a more suitable reference arm length. The mechanical set-up of the final stage for injecting and extracting the laser beam, that was situated on the pyrometer head inside the target chamber, cannot be reached during final alignment with the chamber sealed. Because of this, errors in target holder manufacturing that result in clipping of the reflected beam could only be corrected for up to a certain degree (around 1-2°) by using the last mirror and lens before the chamber window. A possible solution to this problem would be to install a remotely controlled tip/tilt mirror mount for the last 1" mirror in the target chamber, with which, in conjunction with the last mirror outside the chamber, the position and angle of incidence of the laser beam on the target window could be modified. Injecting the diagnostic laser over a fibre, after being chopped with the acousto-optical modulator, could improve spatial uniformity of the light beam. The beam coming out of the fibre should be well collimated in order to have a parallel beam on the target.

As seen in Section 4.6, the line VISARs require laser sources with long coherence lengths (centimetres), which at the same time have to provide long pulses (tens of nanoseconds), at tens of kW. In the experiments described in this work, first an unseeded MiniLase was used, with long and energetic enough pulses, but of a very short coherence length of only a few millimetres. During the main beam-time with PHELIX, the nhelix system was modified to provide longer pulses at the required parameters. Currently, a Continuum custom YLF laser system is planned to serve as future diagnostic laser for the line VISARs. The oscillator runs at 1321 nm and it is Q-switched to output pulses with a duration of ≈90 ns FWHM. To obtain the necessary coherence length, the system will be stabilized by a Vortex seeder. Its infrared output is frequency doubled to 660 nm, at a final energy of ≈3 mJ per pulse. Due to the diffusely reflecting nature of the iron targets, speckle noise played an important role in reducing the fringe quality and contrast. It is possible by optimizing the imaging system to either decrease it to sub-pixel sizes or to have it considerably larger than the fringe width. The phase plate used to obtain a top hat profile from the gaussian one of PHELIX produced a relatively strong central hotspot which could not be satisfactorily reduced by defocusing. Therefore one-dimensional compression could not be properly achieved, and also the generated instabilities caused a significant losses of reflectivity, which degraded the quality of the interferograms. A revised design of the phase plate could mitigate these problems.

Bibliography

[1] E. Dewald, C. Constantin, C. Niemann, D.H.H. Hoffmann, J. Jacoby, T. Schlegel, S. Udrea, D. Varentsov, A. Tauschwitz, *Multiple shockwaves driven by heavy ion beams in solid matter*, GSI Scientific Report 2001 (2002).

[2] S. El Moussati, *Entwicklung, Aufbau und Test eines kontaktfreien Messverfahrens zur Bestimmung der elektrischen Leitfähigkeit dichter Plasmen*, Diploma thesis, Technische Universität Darmstadt (2009).

[3] C. Constantin, E. Dewald, C. Niemann, S. Udrea, D. Varentsov, U.N. Funk, D.H.H. Hoffmann, J. Jacoby, U. Neuner, P. Spiller, A. Tauschwitz, *Energy loss of relativistic heavy ions in matter*, GSI Scientific Report 2000 (2001).

[4] C. Constantin, *Multiple weak shock waves induced by heavy ion beams in solid matter*, PhD thesis, Technische Universität Darmstadt (2002).

[5] D.H.H. Hoffmann, R. Bock, A.Ya. Faenov, U. Funk, M. Geissel, U. Neuner, T.A. Pikuz, F. Rosmej, M. Roth, W. Süß, N. Tahir, A. Tauschwitz *Plasma physics with intense laser and ion beams*, Nucl. Instr. and Meth. B 161-163, 9-18 (2000).

[6] M. Kulish, V.Ya. Ternovoi, V.E. Fortov, V.K. Gryaznov, I.V. Lomonosov, V. Mintsev, D. Nikolaev, N. Shilkin, A. Shutov, D. Varentsov, D. Fernengel, A. Hug, J. Menzel, P. Ni, S. Udrea, D.H.H. Hoffmann, P. Spiller, N.A. Tahir, H. Wahl *Displacement interferometer technique for plasma pressure diagnostic*, GSI Scientific Report 2006 (2007).

[7] D. H. H. Hoffmann, V. E. Fortov, I. V. Lomonosov, V. Mintsev, N. A. Tahir, D. Varentsov, and J. Wieser, *Survey of Theoretical Work for the Proposed HEDgeHOB Experimental Schemes: HIHEX and LAPLAS*, Contributions To Plasma Physics 47, Nr. 4-5, 223–233 (2007).

[8] D. Varentsov, V.Ya. Ternovoi, M. Kulish, D. Fernengel, A. Fertman, A. Hug, J. Menzel, P. Ni, D.N. Nikolaev, N. Shilkin, V. Turtikov, S. Udrea, V.E. Fortov, A.A. Golubev, V.K. Gryaznov, D.H.H. Hoffmann, V. Kim, I.V. Lomonosov, V. Mintsev, B.Yu. Sharkov, A. Shutov, P. Spiller, N.A. Tahir, H. Wahl, *High-energy-density physics experiments with intense heavy ion beams*, Nuclear Instruments and Methods in Physics Research A 577, 262–266 (2007).

[9] S. Udrea, E. Dewald, C. Constantin, D. Varentsov, J. Jacoby, U. Neuner, A. Tauschwitz, P. Spiller, D.H.H. Hoffmann, *Energy loss of relativistic heavy ions in matter* GSI Scientific Report 2000 (2001).

[10] S. Udrea, *Elektrische Leitfähigkeit Dichter, Schwerioneninduzierter Plasmen*, PhD thesis, Technische Universität Darmstadt (2004).

[11] S. Udrea, S. El Moussati, A.D. Fertman, V.E. Fortov, A.A. Golubev, D.H.H. Hoffmann, A. Hug, M.I. Kulish, J. Ling, J. Menzel, V.B. Mintsev, N. Müller, D.N. Nikolaev, A. Pyalling, B.Yu. Sharkov, N.S. Shilkin, V.Ya. Ternovoi, V.I. Turtikov, A. Ulrich, D. Varentsov, J. Wieser, M. Zhukova *Measurements of the Electrical Conductivity of Ion–Beam Generated WDM*, GSI Scientific Report 2008 (2009).

[12] J. Ling, *Entwicklung, Aufbau und Test eines kontaktfreien Messverfahrens zur Bestimmung der elektrischen Leitfähigkeit dichter Plasmen*, PhD thesis, Technische Universität Darmstadt (2011).

[13] A. Frank, A. Blažević, P.L. Grande, K. Harres, T. Hessling, D.H.H. Hoffmann, R. Knobloch-Maas, P.G. Kuznetsov, F. Nürnberg, A. Pelka, G. Schaumann, G. Schiwietz, A. Schökel, M. Schollmeier, D. Schumacher, J. Schütrumpf, V.V. Vatulin, O.A. Vinokurov, M. Roth, *Energy loss of argon in a laser-generated carbon plasma*, Phys. Rev. E 81, 026401 (2010).

[14] V. Bagnoud, A. Blazevic, S. Borneis, U. Eisenbarth, J. Fils, S. Goette, Th. Kuehl, E. Onkels, T. Stoehlker, A. Tauschwitz, D. Zimmer, K. Witte, *PHELIX: A petawatt-class laser recently commissioned for experiments in plasma and atomic physics*, J. Phys.: Conf. Ser. 194 152028 (2009).

[15] P.A. Ni, M.I. Kulish, V. Mintsev, D.N. Nikolaev, V.Ya. Ternovoi, D.H.H. Hoffmann, S. Udrea, A. Hug, N.A. Tahir, D. Varentsov, *Temperature measurement of warm-dense-matter generated by intense heavy-ion beams*, Laser and Particle Beams 26 (04), 583–589 (2008).

[16] R.W. Lee, H.A. Baldis, R.C. Cauble, O.L. Landen, J.S. Wark, A. Ng, S.J. Rose, C. Lewis, D. Riley, J.-C. Gauthier, P. Audebert, *Plasma-based studies with intense X-ray and particle beam sources*, Laser and Particle Beams 20 (03), 527–536 (2002).

[17] R.W. Lee et al., *Warm Dense Matter: An Overview*, https://e-reports-ext.llnl.gov/pdf/307164.pdf, summary of the LLNL Workshop on Extreme States of Materials: Warm Dense Matter to NIF (2004).

[18] A. Ng, T. Ao, F. Perrot, M.W.C. Dharma-Wardana, M.E. Foord, *Idealized slab plasma approach for the study of warm dense matter*, Laser and Particle Beams 23 (04), 527-537 (2005).

[19] R. Cauble, D.W. Phillion, T.J. Hoover, N.C. Holmes, J.D. Kilkenny, R.W. Lee, *Demonstration of 0.75 Gbar planar shocks in x-ray driven colliding foils*, Phys. Rev. Lett. 70, 2102–2105 (1993).

[20] D.H. Kalantar, B.A. Remington, J.D. Colvin, K.O. Mikaelian, S.V. Weber, L.G. Wiley, J.S. Wark, A. Loveridge, A.M. Allen, A.A. Hauer, M.A. Meyers, *Solid-state experiments at high pressure and strain rate*, Phys. Plasmas 7, 1999-2006 (2000).

[21] J. Edwards, K.T. Lorenz, B.A. Remington, S. Pollaine, J. Colvin, D. Braun, B.F. Lasinski, D. Reisman, J.M. McNaney, J.A. Greenough, R. Wallace, H. Louis, D. Kalantar, *Laser-Driven Plasma Loader for Shockless Compression and Acceleration of Samples in the Solid State*, Phys. Rev. Lett. 92, 075002 (2004).

[22] G. Dyer, B. Cho, A. Bernstein, T. Ditmire, R. Shepherd, Hui Chen, Yuan Ping, P.K. Patel, L. Elberson, *Laser Driven X-ray Radiography on Warm Dense Matter*, Quantum Electronics and Laser Science Conference QELS '07 (2007).

[23] S.W. Haan et al., *Design and modeling of ignition targets for the National Ignition Facility*, Phys. Plasmas 2, 2480 (1995).

[24] J. Clérouin, P. Noiret, P. Blottiau, V. Recoules, B. Siberchicot, P. Renaudin, C. Blancard, G. Faussurier, B. Holst, C.E. Starrett, *A database for equations of state and resistivities measurements in the warm dense matter regime*, Phys. Plasmas 19, 082702 (2012).

[25] N.A. Tahir, D.H.H. Hoffmann, J.A. Maruhn, P. Spiller, R. Bock, *Heavy-ion-beam–induced hydrodynamic effects in solid targets*, Phys. Rev. E 60, 4715–4724 (1999).

[26] D.H.H. Hoffmann, V.E. Fortov, I.V. Lomonosov, V. Mintsev, N.A. Tahir, D. Varentsov, J. Wieser, *Unique capabilities of an intense heavy ion beam as a tool for equation-of-state studies*, Phys. Plasmas 9, 3651–3654 (2002).

[27] N.A. Tahir, A. Shutov, D. Varentsov, D.H.H. Hoffmann, P. Spiller, I. Lomonosov, J. Wieser, J. Jacoby, V.E. Fortov, *High-energy-density matter research at GSI Darmstadt using intense heavy ion beams*, Laser and Particle Beams 20 (03), 393-397 (2002).

[28] N.A. Tahir, C. Deutsch, V.E. Fortov, V.Gryaznov, D.H.H. Hoffmann, M. Kulish, I.V.Lomonosov, V. Mintsev, P. Ni, D. Nikolaev, A.R.Piriz, N. Shilkin, P. Spiller, A. Shutov, M. Temporal, V. Ternovoi, S. Udream, D. Varentsov, *Proposal for the Study of Thermophysical Properties of High-Energy-Density States in Matter Using Current and Future Heavy Ion Facilities at the GSI Darmstadt*, Phys. Rev. Lett. 95, 035001 (2005).

[29] *Technical Proposal of the HEDgeHOB Collaboration*, http://hedgehob.physik.tu-darmstadt.de/Docs/HEDgeHOB-TP2005.pdf (2005).

[30] D.C. Hochhaus, B. Aurand, M. Basko, B. Ecker, T. Kühl, T. Ma, F. Rosmej, B. Zielbauer, D. Zimmer, P. Neumayer, *Laser Driven X-ray Radiography on Warm Dense Matter*, GSI Scientific Report 2011 (2012).

[31] B. Yaakobi, F.J. Marshall, D.K. Bradley, J.A. Delettrez, R.S. Craxton, R. Epstein, *Signatures of target performance and mixing in titanium-doped, laser-driven target implosions*, Phys. Plasmas 4, 3021 (1997).

[32] D.H. Kalantar, J. Belak, E. Bringa, K. Budil, J. Colvin, M. Kumar, M.A. Meyers, K. Rosolankova, R. Rudd, M. Schneider, J. Stölken, J.S. Wark, *High-pressure, high-strainrate materials effects*, https://e-reports-ext.llnl.gov/pdf/305598.pdf, LLNL report UCRL-TR-203156 (2004).

[33] O.L. Landen, S.H. Glenzer, M.J. Edwards, R.W. Lee, G.W. Collins, R.C. Cauble, W.W. Hsing, B.A. Hammel, *Dense matter characterization by X-ray Thomson scattering*, J.Q.S.R.T. 71 465 (2001).

[34] D. Kraus, A. Otten, A. Frank, V. Bagnoud, A. Blazevic, D. O. Gericke, G. Gregori, A. Ortner, G. Schaumann, D. Schumacher, J. Vorberger, F. Wagner, K. Wunsch, M. Roth, *First X-ray scattering experiments with shock-compressed matter at GSI*, GSI Scientific Report 2010 (2011).

[35] E. Wolfrum, A.M. Allen, I. Al'Miev, T. W. Barbee Jr., P.D.S. Burnett, A. Djaoui, C. Iglesias, D.H. Kalantar, R.W. Lee, R. Keenan, M.H. Key, C.L.S. Lewis, A.M. Machacek, B.A. Remington, S.J. Rose, R. O'Rourke, J.S. Wark, *Dense matter characterization by X-ray Thomson scattering*, J. Phys. B 34, 565 (2001).

[36] P.M. Celliers, G.W. Collins, L.B. Da Silva, D.M. Gold, and R. Cauble, *Accurate measurement of laser-driven shock trajectories with velocity interferometry*, Appl. Phys. Lett. 73, 1320 (1998).

[37] P. M. Celliers, D. K. Bradley, G. W. Collins, D. G. Hicks, T. R. Boehly, and W. J. Armstrong, *Line-imaging velocimeter for shock diagnostics at the OMEGA laser facility*, Rev. Sci. Instrum. 75, 4916 (2004).

[38] S. Stöwe, *Schwerioneninduzierte Hydrodynamik in Bleitargets*, PhD thesis, University of Erlangen-Nürnberg (1998).

[39] P. Ni, *Temperature measurement of high-energy-density matter generated by intense heavy ion beam*, PhD thesis, Technische Universität Darmstadt (2006).

[40] P. Ni, D.H.H. Hoffmann, M. Kulish, D. Nikolaev, N.A. Tahir, S. Udrea, D. Varentsov, H. Wahl, *Pyrometric system for temperature measurements of HED matter generated by intense heavy ion beams*, J. Phys. IV France 133, 977-980 (2006).

[41] Christiaan Huygens, *Traité de la lumiere* (1690).

[42] Thomas Young, *The Bakerian Lecture. On the Theory of Light and Colours*, Philosophical Transactions of the Royal Society of London 91 (1802).

[43] Thomas Young, *The Bakerian Lecture. On the Theory of Light and Colours*, Philosophical Transactions of the Royal Society of London 94 (1804).

[44] A.A. Michelson, *The relative motion of the earth and the luminiferous aether*, American Journal of Science 22, 120-129 (1881).

[45] G. Hansen, Z. Instrumentenk, 61:411 (1941).

[46] L.M. Barker and R.E. Hollenbach, *Laser interferometer for measuring high velocities of any reflecting surface*, J. Appl. Phys. 43, 4669 (1972).

[47] D.R. Goosman, *Analysis of the laser velocity interferometer*, J. Appl. Phys. 46, 3516 (1975).

[48] W.F. Hemsing, *Velocity sensing interferometer (VISAR) modification*, Rev. Sci. Instrum. 50, 73 (1979).

[49] W.F. Hemsing, A.R. Mathews, R.H. Warnes, G.R. Whittemore, *VISAR: line-imaging interferometer*, Proc. SPIE 1346, Ultrahigh- and High-Speed Photography, Videography, Photonics, and Velocimetry ’90, 133 (1991).

[50] M. Takeda, H. Ina, and S. Kobayashi, *Fourier transform method of fringe-pattern analysis for computer-based topography and interferometry*, J. Opt. Soc. Am. 72, 156-160 (1982).

[51] *EOPC Acousto-optic Modulator*, http://www.eopc.com/mt110.html (2012).

[52] H. Weick, H. Geissel, C. Scheidenberger, F. Attallah, T. Baumann, D. Cortina, M. Hausmann, B. Lommel, G. Münzenberg, N. Nankov, F. Nickel, T. Radon, H. Schatz, K. Schmidt, J. Stadlmann, K. Sümmerer, M. Winkler, H. Wollnik, *Slowing down of relativistic few-electron heavy ions*, Nucl. Instr. and Meth. B 164, 168-179 (2000).

[53] J.F. Ziegler, M.D. Ziegler, J.P. Biersack, *SRIM – The stopping and range of ions in matter (2010)*, Nucl. Instr. and Meth. B 268, 1818-1823 (2010).

[54] B. Ionita, S. El Moussati, D.H.H. Hoffmann, A. Hug, J. Ling, S. Udrea, A. Fedenev, D. Varentsov, K. Weyrich, E. Brambrink, A. Fertman, A. Golubev, A. Kantsyrev, A. Khudomyasov, V. Turtikov, M. Kulish, N. Markov, V. Mintsev, D. Nikolaev, A. Pyalling, N. Shilkin, V. Ternovoi, D. Yuriev, *Imaging Interferometer for Ion-Beam Driven HEDP Experiments*, GSI Scientific Report 2010 (2011).

[55] A. Hug, B. Ionita, A. Kantsyrev, L. Shestov, S. Udrea, D. Varentsov, *Data acquisition system for HHT experiments*, GSI Scientific Report 2011 (2012).

[56] *HHT DAQ and Hardware Control*, http://plasma.itep.ru/pp_hht/notes/HHT0004-DAQ_HC.html (2012).

[57] *Betriebsordnung für die Beschleuniger und Experimentiereinrichtungen der GSI*, Version V01-004 (2009).

[58] J. Jacoby, K. Mahrt, D.H.H. Hoffmann, R.W. Müller, *Heating Dense Matter with Intense Heavy Ion Beams from the RFQ-Accelerator*, GSI Scientific Report 1988 (1989).

[59] M. Dornik, V.P. Dubenkov, A. Filimonov, D.H.H. Hoffmann, M. Kulish, W. Laux, W. Seelig, B. Sharkov, P. Spiller, M. Stetter, C. Stöckl, S. Stöwe, W. Süß, H. Wetzler, *Heavy-ion-beam-induced motion in rare-gas cryo targets*, Fus. Eng. Des., Vol. 32–33, (1996).

[60] M. Stetter, J. Christiansen, U. Neuner, S. Stöwe, R. Tkotz, T. Wagner, E. Boggasch, A. Tauschwitz, D. H. H. Hoffmann, P. Spiller, *Development of a plasma lens as a fine focusing lens for heavy-ion beams*, Il Nuovo Cimento A 106, 1725-1731 (1993).

[61] S. Stöwe, R. Bock, M. Dornik, P. Spiller, M. Stetter, V.E. Fortov, V. Mintsev, M. Kulish, A. Shutov, V. Yakushev, B. Sharkov, S. Golubev, B. Bruynetkin, U. Funk, M. Geissel, D.H.H. Hoffmann, N.A. Tahir, *High density plasma physics with heavy-ion beams*, Nucl. Instr. and Meth. A 415, 61-67 (1998).

[62] W. Barth, *Commissioning of the 1.4 MeV/u High Current Heavy Ion LINAC at GSI*, 20th International Linear Accelerator Conference, Monterey, CA, USA, 21 - 25 Aug 2000, e-proc. FR201 (2000).

[63] W. Barth, L. Dahl, J. Glatz, L. Groening, S.G. Richter, S. Yaramishev, *Achievements of the High Current Beam Performance of the GSI Unilac*, Proceedings of EPAC 2004, Lucerne, Switzerland (2004).

[64] M. Kirk, H. Damerau, I. Hofmann, O. Boine-Frankenheim, P. Spiller, P. Hülsmann, *Phase space growth during RF capture in the GSI heavy ion synchrotron SIS-18*, Laser and Particle Beams 21 (01), 85-89 (2003).

[65] M. Kirk, I. Hofmann, O. Boine-Frankenheim, P. Spiller, P. Hülsmann, G. Franchetti, H. Damerau, H. Günter König, H. Klingbeil, M. Kumm, P. Moritz, P. Schütt, A. Redelbach, *Beam Loss and Longitudinal Emittance Growth in SIS*, AIP Conf. Proc. 773, 381-383 (2004).

[66] *Baseline Technical Report - Executive Summary of the HEDgeHOB Collaboration*, http://hedgehob.physik.tu-darmstadt.de/Docs/HEDgeHOB-TR-Executive_Summary.pdf (2006).

[67] P. Spiller, K. Blasche, O. Boine-Frankenheim, M. Emmerling, B. Franczak, I. Hofmann, U. Ratzinger, S. Lund, *Generation of High Power Heavy Ion Beams at GSI*, Proceedings of the 1999 Particle Accelerator Conference, 1788–1790 (1999).

[68] G. Schaumann, M.S. Schollmeier, A. Azima, A. Blazevic, E. Brambrink, M. Geißel, T. Heßling, A. Pelka, P. Pirzadeh, M. Roth, and D.H.H. Hoffmann, *Upgrade of the nhelix laser system at GSI*, GSI Plasma Annual Report 2004 (2005).

[69] T. Kuehl, *PHELIX – A Petawatt High-Energy Laser for Heavy-Ion EXperiments*, GSI Scientific Report 1998 (1999).

[70] Th. Kuehl, R. Bock, S. Borneis, E. Brambrink, et al., *PHELIX – Status and First Experiments*, Hyperfine Interactions, Springer (2005).

[71] V. Bagnoud, B. Aurand, A. Blazevic, S. Borneis, C. Bruske, B. Ecker, U. Eisenbarth, J. Fils, A. Frank and E. Gaul, *Commissioning and early experiments of the PHELIX facility*, Applied Physics B: Lasers and Optics, Springer Berlin / Heidelberg (2010).

[72] A. Pelka, A. Blazevic, A. Greiche, T. Hessling, D.H.H. Hoffmann, R. Knobloch, G. Rodriguez Prieto, M. Roth, G. Schaumann, M. Schollmeier, *Spatially resolved measurement of the electron density in laser produced plasmas*, GSI Plasma Physics Annual Report 2004 (2005).

[73] D.C. Swift and R.P. Johnson, *Quasi-isentropic compression by ablative laser loading: Response of materials to dynamic loading on nanosecond time scales*, Phys. Rev. E 71, 066401 (2005).

[74] D.C. Swift, R.G. Kraus, E.N. Loomis, D.G. Hicks, J.M. McNaney, R.P. Johnson, *Shock formation and the ideal shape of ramp compression waves*, Phys. Rev. E 78, 066115 (2008).

[75] A. Hug, *Thermodynamische Eigenschaften von schwerionengeheizten hochschmelzenden Metallen*, PhD thesis, Technische Universität Darmstadt (2011).

[76] V. Ternovoi, E. Brambrink, A. Fertman, A. Golubev, D.H.H. Hoffmann, A. Hug, B. Ionita, A. Kantsyrev, K. Khishchenko, A. Khudomyasov, M. Kulish, J. Ling, N. Markov, V. Mintsev, D. Nikolaev, A. Pyalling, N. Shilkin, V. Turtikov, S. Udrea, D. Varentsov, D. Yuriev, *Study of Near-Critical States of Refractory Materials by Intense Heavy Ion Beams*, experimental proposal (2009).

[77] A.V. Bushman, G.I. Kanel, A.L. Ni, V.E. Fortov, *Intense Dynamic Loading of Condensed Matter*, London, Taylor and Francis (1993).

[78] PCO AG: *DiCAM-PRO Operating Instructions*, http://www.pco.de (2012).

[79] D. Varentsov, A.D. Fertman, V.I. Turtikov, A. Ulrich, J. Wieser, V.E. Fortov, A.A. Golubev, D.H.H. Hoffmann, A. Hug, M. Kulish, V. Mintsev, P.A. Ni, D. Nikolaev, B.Yu. Sharkov, N. Shilkin, V.Ya. Ternovoi, S. Udrea, *Transverse Optical Diagnostics for Intense Focused Heavy Ion Beams*, Contributions To Plasma Physics 48 (08), 586–594 (2008).

[80] National Institute of Standards and Technology (NIST). *Stefan-Boltzmann constant*, http://physics.nist.gov/cgi-bin/cuu/Value?sigma (2012).

[81] *Acoustic impedance of sapphire*, http://traktoria.org/files/sonar/passive_materials/acoustic_impedace_of_some_solids.htm (2012).

[82] J. Stefan, *Über die Beziehung zwischen der Wärmestrahlung und der Temperatur*, Sitzungsberichte der mathematisch-naturwissenschaftlichen Classe der kaiserlichen Akademie der Wissenschaften 79, 391-428 (1879).

[83] L. Boltzmann, *Ableitung des Stefan'schen Gesetzes, betreffend die Abhängigkeit der Wärmestrahlung von der Temperatur aus der electromagnetischen Lichttheorie*, Annalen der Physik und Chemie 22, 291-294 (1884).

[84] W. Wien, *Ueber die Energievertheilung im Emissionsspectrum eines schwarzen Körpers*, Annalen der Physik und Chemie 294 (08), 662–669 (1896).

[85] M. Planck, *Entropie und Temperatur strahlender Wärme*, Annalen der Physik 306 (04), 719–737 (1900).

[86] K. Miyanishi, N. Ozaki, E. Brambrink, H. G. Wei, A. Benuzzi-Mounaix, A. Ravasio, A. Diziere, T. Vinci, M. Koenig, R. Kodama, *EOS measurements of pressure standard materials using laser-driven ramp-wave compression technique*, J. Phys.: Conf. Ser. 215 012199 (2010).

[87] H. Bethe, Ann. Physik 5, 325 (1930).

[88] J. Lindhard, A.H. Sørensen, *Relativistic theory of stopping for heavy ions*, Phys. Rev. A 53, 2443–2456 (1996).

[89] C. Scheidenberger, H. Geissel, *Penetration of relativistic heavy ions through matter* Nucl. Instr. and Meth. B 135, 25-34 (1998).

[90] B.A. Weaver, A.J. Westphal, *Energy loss of relativistic heavy ions in matter* Nucl. Instr. and Meth. B 187, 285-301 (2002).

[91] A. Jayaraman, *Ultrahigh pressures*, Rev. Sci. Instrum. 57, 1013 (1986).

[92] J. M. Winey, Y. M. Gupta, D. E. Hare, *r-axis sound speed and elastic properties of sapphire single crystals*, J. Appl. Phys. 90, 3109 (2001).

[93] V. Ternovoi, *private communications* (2012).

[94] D.B. Reisman, A. Toor, R.C. Cauble, C.A. Hall, J.R. Asay, M.D. Knudson, M.D. Furnish, *Magnetically driven isentropic compression experiments on the Z accelerator*, J. Appl. Phys. 89, 1625 (2001).

[95] D.G. Tasker, J.H. Goforth, H. Oona, C.M. Fowler, J.C. King, D. Herrera, D. Torres, *Advances in Isentropic Compression Experiments (ICE) Using High Explosive Pulsed Power*, AIP Conf. Proc. 706, 1239-1242 (2004).

[96] T. Guillot et al., *Interiors of Giant Planets Inside and Outside the Solar System*, Science 286 (5437), 72-77 (1999).

[97] J.D. Lindl, P. Amendt, R. L. Berger, S. Gail Glendinning, S.H. Glenzer, S.W. Haan, R.L. Kauffman, O.L. Landen, L.J. Suter, *The physics basis for ignition using indirect-drive targets on the National Ignition Facility*, Phys. Plasmas 11, 339 (2004).

[98] D.A. Pepler, S. Paradowski, *Design of Binary Phase Plates Using LabView*, Central Laser Facility Annual Report 2005-2006, 211-214 (2006).

[99] R.W. Gerchberg, W.O. Saxton, *A practical algorithm for the determination of the phase from image and diffraction plane pictures*, Optik 35, 237-246 (1972).

[100] Th. Kühl, J. Alvarez, B. Becker-de Mos, R. Bock, S. Borneis, E. Brambrink, H. Brand, D. Browning, C. Bruske, K. Brück, J. Caird, E. Dewald, H. Duddek, E. W. Gaul, C. Häfner, T. Hahn, D.H.H. Hoffmann, H.-J. Kluge, D. Marx, P. Neumayer, M. Perry, K. Poppensieker, D. Reemts, I. Reinhard, M. Roth, S. Samek, W. Seelig, A. Tauschwitz, R. Wilcox, *PHELIX, a Petawatt High Energy Laser for Heavy-Ion Experiments*, GSI Scientific Report 2001 (2002).

[101] T. Takahashi, W.A. Bassett, *High-Pressure Polymorph of Iron*, Science 145 (3631), 483-486 (1964).

[102] M. Bastea, S. Bastea, R. Becker, *High pressure phase transformation in iron under fast compression* Appl. Phys. Lett. 95, 241911 (2009).

[103] Ya.B. Zel'dovich, Yu.P. Raizer, *Physics of Shock Waves and High-Temperature Hydrodynamic Phenomena*, Academic Press New York and London (1966).

[104] Daniel H. Dolan, *Foundations of VISAR analysis*, Sandia Report SAND2006-1950 (2006).

[105] N. Amadou, E. Brambrink, A. Benuzzi-Mounaix, T. Vinci, T. de Resseguier, S. Mazevet, G. Morard, F. Guyot, N. Ozaki, K. Miyanishi, M. Koenig, *Laser-driven quasi-isentropic compression experiments and numerical studies of the iron alpha-epsilon transition in the context of planetology*, AIP Conf. Proc. 1426, 1525-1528 (2011).

Acknowledgements

Firstly, I would like to express my gratitude to Prof. Dr. Dr. h.c./RUS Dieter H.H. Hoffmann for giving me the opportunity to perform my PhD research work within the Plasma Physics group at GSI and for his continuous and kind support.

Secondly, I am indebted to Dr. Dmitry Varentsov and Dr. Serban Udrea for all their help during my activity at GSI.

I also wish to thank Dr. Erik Brambrink for many clarifying discussions regarding both the interferometric aspects of my work, as well as phenomena related to isentropic compression of materials.

Dr. Alexander Hug was of great help with optical pyrometry issues and during many hours of beam-time.

Dr. Vladimir Ternovoi, Dr. Dmitry Nikolaev and Dr. Nikolai Shilkin provided essential support for data analysis. Thank you very much!

I would also like to show my consideration for all the help received in preparation of our experiments and in sharing of the long and tiresome, but truly engaging beam-time shifts to the entire HHT experimental team: Dr. Karin Weyrich, Said El Moussati, Philipp Lang, Dr. Johannes Ling, Dr. Alexander Fertman, Alexander Kantsyrev, Nikolai Markov, Dr. Vladimir Turtikov.

A big thank you goes to the entire Z6 and PHELIX groups, especially Dr. Abel Blazevic, Dr. Vincent Bagnoud, Alexander Ortner, Florian Wagner and Witold Cayzac.

Many thanks go to Dr. Claudia-Veronika Meister who has been very supportive with several theoretical aspects of my work.

Last but not least I am grateful to Dr. Dan Apostol, Dr. Catalin Logofatu and Dr. Marian Ristici from the National Institute for Laser, Plasma and Radiation Physics and University of Bucharest Romania, for introducing me to the field of optical interferometry.

This research work was funded by the Helmholtz-Russia Joint Research Group HRJRG-112.

Curriculum Vitae

Name	Bogdan-Florin Cihodariu-Ionita (name before marriage: Ionita)
Birth date / place	27.09.1985 / Bacau, Romania
Citizenship	Romanian

Educational profile

1992-2000	Primary and secondary school in Bacau
2000-2004	Highschool "Ferdinand I", class of Mathematics and Informatics in Bacau
2004-2009	Diploma at University of Bucharest, 2009. Thesis: "Digital Holography Algorithms Implemented on Video Processors".
since August 2009	PhD student at the Technical University of Darmstadt and GSI-Darmstadt, Germany.

Erklärung zur Dissertation

Hiermit versichere ich, die vorliegende Dissertation ohne Hilfe Dritter nur mit den angegebenen Quellen und Hilfsmitteln angefertigt zu haben. Alle Stellen, die aus Quellen entnommen wurden, sind als solche kenntlich gemacht. Diese Arbeit hat in gleicher oder ähnlicher Form noch keiner Prüfungsbehörde vorgelegen.

Darmstadt, den 27. November 2012

(Bogdan-Florin Cihodariu-Ionita)